University of Salford MANCHESTER

USING MAGNETO-INERTIAL-MEASUREMENT-UNITS TO TRACK UPPER-LIMB MOVEMENT DURING REHABILITATION

ABDULLAH ABDULKAREEM ABDULRAHMAN AL-ANI

Thesis submitted to the School of Computing, Science and Engineering in partial fulfilment of the requirements for the degree of

Doctor of Philosophy

School of Computing, Science and Engineering

University of Salford,

Salford, UK, 2020

CONTENTS

LIST OF FIGURES

LIST OF TABLES

ACKNOWLEDGEMENTS

First and foremost, I would like to express my deepest gratitude to the Almighty Allah for His never-ending grace, mercy, and provision during what ended up being one of the toughest times of my life.

This work would not have been achieved without those people who supported me during my research work. First, I would like to express my sincere gratitude and deepest appreciation to my supervisor Professor David Howard and my co-supervisor Professor Laurence Kenney for their continued guidance, sincere motivation and encouragement, thoughtful support, kindness, help and advice. Their unbound patience and friendly approach have left a lasting impression.

I would also like to thank my research colleagues for their help and support, their technical discussions have been highly beneficial.

I am most grateful to my parents, my brothers and sisters for their love, support and encouragement.

Finally, I gratefully acknowledge the love, patience, encouragement and support of my wife Hanaa who has been a wonderful woman as well as my little daughter Jenna. I am forever indebted to them.

NOTATION LIST

A_k : Anatomical coordinate frame, where k is the body segment.

D Distal segment.

F Forearm segment.

H Hand segment.

k Body segment.

LAB : Laboratory coordinate frame.

P Proximal segment.

$^{A}R_{B}$: Rotation matrix, representing the orientation of frame B with respect to frame A.

$^{SI_k}R_{A_k}$: Calibration rotation matrix, representing the orientation of a body-segment's Anatomical frame with respect to its Sensor Inertial frame.

$^{SG}R_{SI_k}$: Orientation of a Sensor Inertial frame with respect to the Sensor Global frame (i.e. the sensor output).

$^{LAB}R_{A_k}$: Lab-segment rotation matrix, representing the orientation of a body-segment's Anatomical frame with respect to the LAB frame.

$^{A_P}R_{A_D}$: Joint rotation matrix, representing the orientation of a distal segment's Anatomical frame with respect to a proximal segment's Anatomical frame.

SG : Sensor Global coordinate frame.

SI_k : Sensor Inertial coordinate frame.

SM_k : Sensor Marker coordinate frame.

T Thorax segment.

U Upper-arm segment.

ABBREVIATIONS

A	Anatomical coordinate frame
AI	Artificial intelligence
ADL	Activities of daily living
CNS	Central nervous system
DoF	Degree of Freedom
EEG	Electroencephalogram
EMG	Electromyographic
ENG	Electroneurogram
ES	Electrical stimulation
EST	Electrical stimulation therapy
FES	Functional electrical stimulation
FSM	Finite-state-machine
GCF	Global coordinate frame
GUI	Graphical user interface
JCF	Joint coordinate frame
LCF	Local coordinate frame
MIMU	Magnetic and inertial measurement unit
MT	Motion tracker
NN	Neural network
SCI	Spinal cord injury
SCF	Sensor coordinate frame
TES	Therapeutic electrical stimulation

ABSTRACT

Functional Electrical Stimulation (FES) can be used to support upper-limb rehabilitation after a stroke. A key aspect of FES control and also patient monitoring is the automatic tracking of upper-limb motion during intensive and functional practise of upper-limb tasks. To achieve this in a home environment, simple on-body sensors are required. A promising approach is to use Magnetic and Inertial Measurement Units (MIMUs), but they provide body-segment orientations rather than anatomical joint angles, the latter being more meaningful. To solve this problem the sensor orientation data must be interpreted anatomically, which requires that for each body-segment the orientation of its sensor coordinate frame is known with respect to its anatomical coordinate frame. Therefore, appropriate calibration must be performed to obtain the relationship between each sensor frame and its corresponding body-segment anatomical frame.

While many papers have been published on anatomical calibration methods for MIMUs, there has been no comprehensive comparison of the alternative approaches to establish their relative merits. For FES supported upper-limb therapy, the need is for simple and fast donning and calibration, whilst achieving acceptable accuracy and repeatability with regards to the calculated joint kinematics. Therefore, the main objective of the PhD research was to undertake such a comparison and make recommendations for donning and calibration for the purposes of upper-limb FES.

To address this problem the PhD work included:

1. Undertaking a comprehensive and critical comparison of alternative anatomical calibration methods for MIMUs in terms of accuracy, speed, and simplicity.
2. Finding the most appropriate anatomical calibration methods for use in upper-limb FES applications with stroke patients.
3. Determining the best methods for processing MIMU outputs to provide anatomically meaningful upper-limb kinematic data.
4. Experimentally assessing these methods against a gold standard (a VICON optical motion capture system).

The results demonstrate that there is considerable variation between the alternative sensor defined anatomical frames and, hence, confirm the need for comprehensive comparisons. The comparisons reported in this thesis have led to tentative recommendations. Nevertheless, the methods reported are a sound foundation for future work to provide stronger recommendations, with more formal measures of confidence.

Chapter 1 – Introduction

1.1 Background

Every year 15 million people worldwide suffer a stroke, nearly six million of whom die, and another five million are left permanently disabled (WHO, 2003). Indeed, stroke is the second leading cause of disability, after dementia (WHF, 2016). Approximately 50% of stroke survivors experience significant upper-limb functional limitations (Broeks, Lankhorst, Rumping, & Prevo, 1999; Heller et al., 1987; Parker, Wade, & Langton Hewer, 1986; Timmermans et al., 2009) due to a reduction in or inappropriate muscle activations and impaired coordination (Barker, Brauer, & Carson, 2008; Burgar et al., 2011; Harris & Eng, 2010; Timmermans et al., 2009).

A wide range of rehabilitation interventions aim to help restore upper-limb function after stroke. Interventions include conventional physiotherapy, robotic assisted therapy, therapeutic electrical stimulation (TES), and functional electrical stimulation (FES). FES is the controlled use of electrical pulses to produce contraction of muscles in such a way as to support functional movement. The ideal FES control system should enable a patient to practice a variety of different upper limb functional tasks, using as much as possible of the patient's own functional ability. The system should also adapt to changes in the patient's ability to continually challenge him/her. Finally, the system should be easy to use and setup (Lynch & Popovic, 2008). However, achieving satisfactory levels of FES control is very challenging because of the nonlinear (Ferrarin, Palazzo, Riener, & Quintern, 2001; Lynch & Popovic, 2008) and time-varying (Lynch & Popovic, 2008) response of muscles to stimulation. Furthermore, perturbations from muscle spasticity and other central nervous system feedback loops introduce often unpredictable challenges to the controller (Lynch & Popovic, 2008).

A key aspect of FES control is the automatic tracking of upper-limb motion and, to achieve this in a home environment, simple on-body sensors are required. Additionally, regular clinical assessments of rehabilitation progress are important and, ideally, these should be based on objective measurement of upper-limb and body movements during functional task practise in order to assess the effects of

muscle weaknesses and coordination dysfunctions. A promising approach is to use Magnetic and Inertial Measurement Units (MIMUs). In this context, the Salford group have developed a MIMUs based FES system that incorporates a finite-state-machine (FSM) controller, which is easy to set up and flexible enough to allow for varied functional task practice across a range of patients. The therapist can use a simple graphical user interface (GUI) to set up a variety of different FSM controllers, corresponding to different upper-limb functional tasks, tailored to the individual patient. However, the system has the following limitations:

- Significant therapist input is still required to set up the FSM controller and to adapt the controller as the patient's status changes;

- It uses MIMUs to provide segment orientations, but not anatomical joint angles, which are more meaningful;
- The controller cannot automatically adapt the stimulation profiles as the patient changes (e.g. fatigues or improves their performance with practise).

In order to move towards a more automated approach to both setup and adapting to changes in the patient, further work is required. This PhD focusses on solving the second problem listed above. In other words, the focus is on the estimation of anatomical joint angles using data from MIMUs on adjoining upper-limb segments (Al-Ani, Howard, & Kenney, 2017). This is clinically important because using body segment orientations, rather than anatomical joint angles, allows users to compensate for muscle weaknesses and coordination dysfunctions by moving proximal segments to change the orientation of a more distal segment, without using their anatomical joints correctly as needed for good rehabilitation. This may also be associated with reduced patient effort to use their weaker muscles and hence reduced efficacy of the intervention.

The MIMU orientation data cannot be interpreted anatomically unless the orientations of the MIMUs (sensors) are known with respect to the anatomy. Therefore, appropriate calibration must be performed to obtain the relationships between each sensor coordinate frame and its corresponding anatomical (body segment) coordinate frame, and two approaches are possible. Firstly, by careful positioning of the sensor on the body segment, a known geometric relationship

between the sensor frame and the anatomical frame may be assumed without the need for any additional calibration procedures. In the simplest case, the segment anatomical axes are equivalent to the sensor axes. In the second approach, the sensor does not have to be positioned as carefully and calibration procedures are followed to construct the anatomical frame based on sensor readings. These procedures can include a combination of static calibrations, where the body segment is held in a defined position while readings are taken; and dynamic (functional) calibrations where the participant performs a specific functional movement while readings are taken.

Importantly, the anatomical calibration problem is still an open research question because no study has comprehensively compared alternative approaches to determine the best calibration methods. While many papers have been published on sensor-to-segment calibration, there has been no comprehensive comparison of the alternative approaches to establish their relative merits. For FES supported upper-limb therapy, the need is for simple and fast donning and calibration, whilst achieving acceptable accuracy and repeatability with regards to the calculated joint kinematics. Therefore, the primary objective of the PhD research was to undertake such a comparison and make recommendations for donning and calibration for the purposes of upper-limb FES.

1.2 Objectives

To achieve the overarching aim of estimating anatomical joint angles using data from MIMUs on adjoining upper-limb segments, the following research objectives have been set:

1. Undertake a comprehensive and critical comparison of alternative anatomical calibration methods for MIMUs in terms of accuracy, speed, and simplicity.
2. Find the most appropriate anatomical calibration methods for use in upper-limb FES applications with stroke patients.
3. Determine the best methods for processing MIMU outputs to provide anatomically meaningful upper-limb kinematic data.
4. Experimentally assess these methods against a gold standard (VICON optical motion capture system).

1.3 Overview of thesis

The organisation of the thesis is based on the sequence of work.

Chapter 2 begins with general background on healthy and damaged neural control. Next, upper-limb rehabilitation following stroke is introduced including current FES systems as well as the Salford FES system. Then a review of human motion tracking systems is presented, particularly focussed on the upper-limb. Last, a comprehensive review of the measurement of upper-limb kinematics using MIMUs, including calibration methods, is presented.

Chapter 3 describes the experimental work using two synchronised measurement systems. Firstly, descriptions of body worn MIMUs and stereophotogrammetry are presented. Secondly, the synchronised measurement of upper-limb movement using the two systems is described, including experimental set-up, marker and sensor placements, and the movement trials (calibration trials and functional task trials). Finally, the methods for pre-processing the raw MIMUs data and also for processing the stereophotogrammetry data are explained.

Chapter 4 addresses the problem of anatomical calibration and the calculation of joint kinematics using MIMUs data. Firstly, the basic principles of deriving anatomical axes and the corresponding calibration rotation matrices are introduced. Secondly, the many alternative calibration methods and their corresponding calibration rotation matrices are presented in detail for the Thorax, Upper-arm, Forearm and Hand. Finally, methods are presented for calculating the joint rotation matrices for the Lab-thorax, Shoulder, Elbow, and Wrist, using the calibration rotation matrices for their proximal and distal segments.

Chapter 5 compares the alternative calibration methods described in Chapter 4. Three different sets of results are presented. Firstly, for each body segment, the orientations of the alternative anatomical frames, relative to their common sensor inertial frame, are compared (each one corresponding to one alternative calibration rotation matrix). Secondly, for each joint, the best pair of calibration rotation matrices (i.e. for proximal and distal segments) is found using a sequential assessment process. Furthermore, for each joint, the best pair of

calibration rotation matrices is found using an independent assessment process. Finally, conclusions are discussed.

Chapter 6 summarises the work, draws conclusions, and makes recommendations for future work.

Chapter 2 – Literature Review

2.1 Background

2.1.1 Neural control in healthy subjects

The upper limb is a complex structure and, excluding scapular motion, the upper-limb with its shoulder, elbow, and wrist joints has 7 DOF, making it kinematically redundant (Prilutsky et al., 2011). Therefore, multiple joint trajectories are possible to complete any given task. Its complexity makes it difficult to model and demonstrates the sophistication of the human neural control system (Miller, Kim, & Rosen, 2011).

The intact CNS (brain and spinal cord) controls voluntary movements as follows. Firstly, visual information is required to locate the target or determine the movement. Secondly, the parts of the brain involved in planning the movement exchange information with the motor cortex (Saladin, 2001). Upper motor neurons that originate completely either in cerebral cortex or brain stem are then activated and send information to the spinal cord. Note that upper motor neurons axons decussate (cross over) before synapsing with lower motor neurons. Thus the left side of the body is controlled by the right motor cortex, and vice versa (i.e. contralateral control) (Monkhouse, 2005). Lower motor neurons are efferent nerve fibres that carry signals from spinal cord to effectors (e.g. hand) to produce effect or movement (Bear, Connors, & Paradiso, 1996; Burke, 2007). Connectivity between the upper and lower motor neurons occurs in the spinal neurons.

Sensory receptors, which are part of sensory neurons and certain spinal reflexes, transmit sensory information (e.g. position of the limb and force applied to limb) towards the central nervous system via afferent fibres. Visual feedback also provides information to the brain which makes necessary adjustments during the movement (Pierrot-Deseilligny & Burque, 2005; Rothwell, 1994).

2.1.2 Central nervous system damage

Damage to the CNS due to trauma, stroke, or disease, in conjunction with other health problems (e.g. muscle atrophy, joint contractures) can result in decreased sensory-motor performance. The regions of the body affected are determined by the extent and type of injury, stroke, or disease. For example thoracic lesions lead to paraplegia, cervical lesions result in tetraplegia, and brain lesions cause in hemiplegia or cerebral palsy (Popović, 2014). A stroke is a type of brain lesion/injury caused by an abnormality of the blood supply to a portion of the brain. When a part of the brain is damaged due to a bleed or inadequate blood supply, that part of brain becomes unable to perform its normal function.

A stroke may result in many different types of dysfunctions and disabilities. Motor dysfunction after stroke is characterised by weak, stiff, or uncoordinated movement with different severities, ranging from decrease in strength to paralysis (Caplan, 2010). The functions of individual limbs are controlled from different locations within the brain and spinal cord. Thus, any impairment in the region of the brain associated with control of that part may lead to reduced or total absence of voluntary control of the affected part (i.e. loss of motor function).

2.1.3 Artificial means of restoring function following central nervous system damage

Although traditional therapeutic rehabilitation approaches may help to restore upper limb motor function after stroke, a considerable portion of stroke patients retain motor deficits after completing therapy (Management of Stroke Rehabilitation Working Group, 2010). However, recent studies have shown that in chronic stroke patients, very intensive rehabilitation upper-limb programmes can lead to a substantial improvement in measures of impairment and activity, which are also clinically meaningful (Ward, Brander, & Kelly, 2019). In Ward's study patients received a total of 90 hours of therapy, delivered 6-hours/day, 5 days a week, for 3 weeks.

By contrast, only low intensity therapy is available to patients owing to a limited availability of therapists. For example, people with upper limb impairments following stroke receive treatment from physiotherapists and occupational

therapists three times per week (median value), with a mean duration of therapy sessions of 29 min. This shows that the current provision of upper-limb therapy is significantly lower than evidence suggests is required to drive recovery (Stockley, Peel, Jarvis, & Connell, 2019). Relatively low therapy doses are also found in other countries. For example, in a study of 7 sites in the United States and Canada, stroke patients were seen by therapists on average 4 days a week, 1-2 times a day. Average session duration was 36±14 minutes (Lang et al., 2009).

Therefore, another approach, the use of electrical stimulation (ES), has been investigated (Baker, Wederich, Newsam, & Waters, 2000). ES is a technique that uses electric impulses (or electrical current) to stimulate nerve(s) and hence cause contractions in muscle(s). Functional electrical stimulation (FES) is the use of electrical stimulation to assist with performance of a functional activity, such as walking, or reaching to grasp an object. FES can be used a means of practicing functional movements for therapeutic benefit (Sheffler & Chae, 2007) and an FES control system, coupled with residual voluntary movement, may restore elements of voluntary functional upper-limb movement (Howlett, Lannin, Ada, & McKinstry, 2015). Use of FES is clinically supported (J. De Kroon, Van der Lee, IJzerman, & Lankhorst, 2002), and the potential of FES to restore voluntary function is enhanced when the person's intention to move is associated with stimulation (J. R. de Kroon, Ijzerman, Chae, Lankhorst, & Zilvold, 2005) and the opportunity for repetitive task oriented movement practice is provided (Hughes et al., 2009). These studies, as well as the basic science studies reported above, support the potential for motor relearning to be facilitated by FES-mediated functional movement (Sheffler & Chae, 2007).

FES (Baker et al., 2000) is now widely used in helping restore motor function for stroke patients (Lynch & Popovic, 2008). The core of any FES system is the controller that calculates the stimulation patterns needed to be applied to specific muscles at particular times in order to perform the desired function. This task is complicated, due to the highly non-linear, redundant and time-varying properties of the musculoskeletal system (Chizek et al., 1988). Furthermore, upper limb movements are goal-directed, (Crago, Lan, Veltink, Abbas, & Kantor, 1996) and hence the amplitude, velocity and direction of the motions vary greatly depending on the task to be performed.

Researchers have developed a number of different systems which use a variety of different types of control to address these problems. The following section describes the characteristics of an ideal upper-limb FES system.

2.1.4 What are the ideal characteristics of an upper-limb FES system?

To enable patients to practice at the levels of intensity suggested by (Ward et al., 2019) , an FES system for the upper limb should ideally be able to be used at home. Design of a home-based FES system is challenging as the setup would need to be individualised to each patient's needs and the software and hardware be sufficiently easy to use by patients and/or carers. Further, an FES system should also ideally synchronise stimulation with the patients voluntarily effort, as this may have a positive impact on CNS reorganisation (Rushton, 2003). Finally, the patient should always be challenged in the task they are practicing (Nudo, Plautz, & Milliken, 1997). To address this, adaptive control techniques may be required.

As shown in Figure 2.1, the general concept of assistive systems which have been used to augment movement may include a powered exoskeleton or an FES system. With either type of system, the user traditionally controls the assistive device with a physiological command signal (e.g. EMG, EEG, residual limb movement). The system then assists by either moving the arm with robotic support or by stimulating relevant muscles. This type of system can be used in conjunction with residual voluntary effort to complete the desired task.
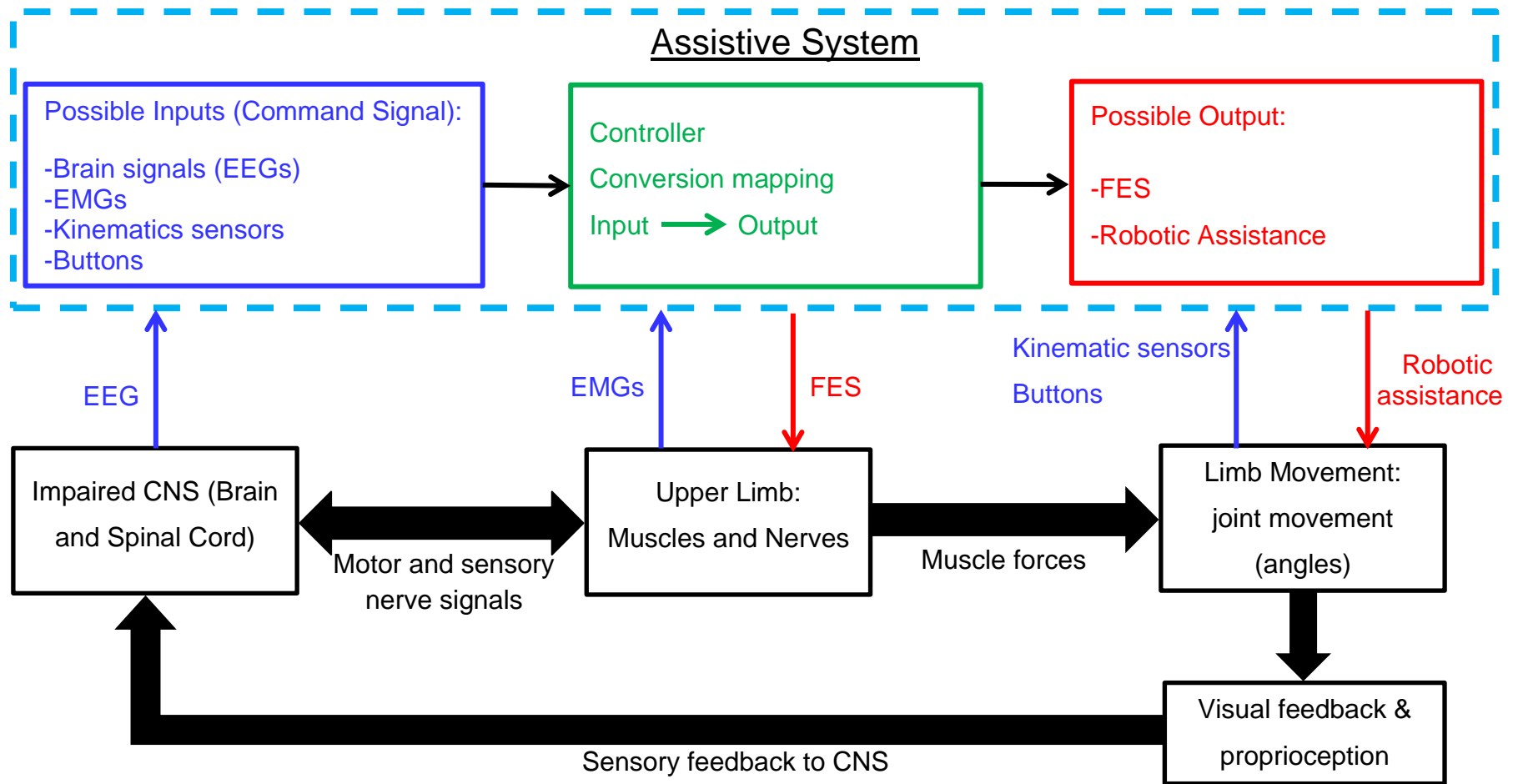
Figure 2.1 : General concept for a stroke assistive system (FES system) showing possible system inputs, feedback signals and outputs

2.1.5 Current FES systems

Upper-limb motion is non-periodic, unrestricted, and redundant. Movement control of the upper-limb in stroke patients via FES is, therefore, a complex problem (Tresadern, Thies, Kenney, Howard, & Goulermas, 2008). Furthermore, the nonlinearity of target muscles, rapid changes in muscle properties due to fatigue, muscle spasticity, perturbations, and noise from unwanted signals from the nervous system are considered major problems that limit the success of FES control (Ferrarin et al., 2001; Lynch & Popovic, 2008)

To address these issues, researchers have developed different types of control strategies. These can be classified under one or more of the following headings: open-loop control, closed-loop control, finite-state-machine control, hybrid control, iterative learning control, and adaptive control. Closed-loop control is particularly difficult because of the aforementioned major problems. Conversely, simple open-loop control (e.g. timed exercise stimulation) does not sufficiently involve the patient. Finite-state-machine (FSM) control provides a compromise that avoids the need for continuous closed-loop control, but nevertheless involves the patient through the voluntary triggering of the transitions between states.

In Table 2.1 below, the published studies on FSM control of FES for the upper-limb are reviewed. The first column contains the name of the system; a letter indicating whether the electrodes are Percutaneous (P), Surface (S); and the number of channels; the year invented.

Table 2.1: FSM control systems for upper-limb FES

System	Control signal	Stimulation profile	Sensors used	Restricted to specific part of body	Voluntary triggered by body worn sensor	Functional task provided	Can be programmed to particular functional task	References
MES-controlled FES (P, 2, 2004)	Voluntary movement (MES) (threshold) (indirect)	Manually adjusted	EMG sensor	Yes	Yes	Grasping	No	(Knutson, Hoyen, Kilgore, & Peckham, 2004)
Clinical-setup tool (CST) by (Tresadern et al., 2008) (S, 2, 2008)	x-acceleration, y-acceleration, and time (T). In other word, Voluntary movement (when the accelerometer exceeds the threshold), or time	Manually adjusted	Two 2-axes accelero-meters	No	Yes	Open and close the hand in drinking task	Yes	(Tresadern et al., 2008)

System	Control signal	Stimulation profile	Sensors used	Restricted to specific part of body	Voluntary triggered by body worn sensor	Functional task provided	Can be programmed to particular functional task	References
Salford FES (HASOMED GmbH) (RehaStim) (S, 8, 2010s)	Switch (push-button), time, or satisfy conditions based on accelerometers data	Manually adjusted	Xsens (Accelero-meters)	No	Yes	Different tasks	Yes	(Sun, 2014)
Portable system (Crook & Chappell, 1998) (S,8, 1998)	Wrist movement detected by wrist position sensor, and force sensors	Adjusted based on information from sensors and pulse width when exceed threshold	5 Force sensors on fingertips and 1 sensor on the wrist	Yes	Yes	Grasp-release	No	(Crook & Chappell, 1998)

2.1.6 The Salford FES system

The Salford team, funded by the UK Department of Health have produced a flexible upper-limb FES system, based FSM control, which enables therapists to setup patient and task-specific state machine controllers (Smith et al., 2017, 2019; Sun et al., 2016, 2018). The FSM controller represents a given functional activity as a sequence of movement phases or states, each of which is associated with stimulation to one or more muscles at user-defined levels. Additionally, transitions conditions for moving from one state to another (between phases) are governed by user-defined rules, which use inputs from body-worn Magnetic and Inertial Measurement Unit sensors (MIMUs) (Sun, 2014).

However, the system limitations are as follows:

- Significant therapist input is still required to set up the state-machine controller and to adapt the controller as the patient's status changes;
- It uses individual MIMUs to provide segment orientations, but does not combine information from pairs of MIMUs on adjoining segments to give anatomical joint angles, which are more meaningful;
- The controller cannot automatically adapt the stimulation profiles as the patient changes (e.g. fatigues or improves their performance with practise).

In order to move towards a more automated approach to both setup and adapting to changes in the patient, further work is required. This PhD focusses on solving the second problem listed above. In other words, the focus is on the estimation of anatomical joint angles using data from MIMUs on adjoining upper-limb segments. Therefore, the following section reviews literature on methods that have been use for measuring upper-limb motion, particularly using MIMUs.

2.2 Human motion tracking

Rehabilitation is a dynamic process that uses assisted practice to help patients to regain more normal functional movement (Sveistrup, 2004) and, hence, to enable patients to regain the highest possible level of independence (Zhou & Hu,

2007b, 2007a). To achieve assisted practice using automated technology such as FES, the movement of patients' limbs needs to be continuously monitored. This is particularly the case in a home based rehabilitation scheme (Zhou & Hu, 2004). More specifically, the patients should be able use the rehabilitation system at home without the need for a therapist to be present at each session. Therefore, since the 1980s, human motion tracking for rehabilitation has been an active research topic.

Many sensor technologies and estimation algorithms have been used in human motion tracking (Bodor, Jackson, Masoud, & Papanikolopoulos, 2003). Sensor data can be used to describe the movement of individual body segments such as the head, torso, upper-arm, forearm etc. However, the sensor signals include errors and noise in part because of relative movement between on-body sensors or markers and the underlying bones (known as the skin artefact).

According to (Sidenbladh, Black, & Fleet, 2000), motion tracking systems can be classified generally under three headings: visual, non-visual, and robot-aided (Figure 2.2) and these headings will be used in the following brief review.
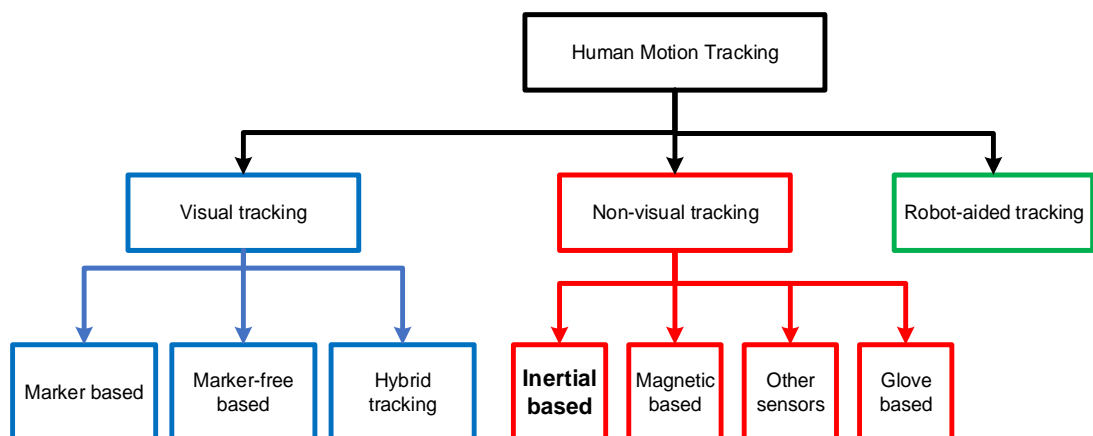
Figure 2.2: Classification of human motion tracking using sensor technologies

2.2.1 Visual tracking systems

Visual tracking systems use optical sensors such as cameras and can provide high accuracy in marker position estimation. Visual tracking systems can be classified as follows:

A. **Marker-based visual tracking systems:** This is a technique where cameras track markers placed upon the human body (typically on bony landmarks). Suppliers include Qualisys, VICON, CODA, ReActor2, ELITE Biomech, APAS, Polaris, and Optotrack. Camera-based motion capture systems have been widely used for quantifying upper- and lower-limb kinematics during different activities in laboratory settings (Zhang, Novak, Brouwer, & Li, 2013) and are often used as a "gold standard" because of the accuracy of the marker position data (around 1 mm). A major disadvantage of using cameras with on-body markers is the possibility of occlusion of markers by the moving body segments, which means that camera and marker placement is a non-trivial problem. Additionally, they are complex, very expensive, and require careful setup, generally in a dedicated room. This makes these systems unsuitable for home use (Yi Zhang, Huosheng Hu, & Huiyu Zhou, 2005; Zhou & Hu, 2008).

B. **Marker-free visual tracking systems:** Marker-free visual tracking systems use cameras to capture the point clouds representing the individual body segments without requiring markers. Complex image processing techniques are then used to fit an anatomical model to the point clouds (stick figures and volumetric representations). The advantage of such systems is that they do not need careful placement of markers on the body and, therefore, may be more usable in a home setting. However, they are less accurate than marker-based systems and rely on good lighting conditions, clothing that is tight and stands out against the background. Furthermore, cameras with high resolution and speed, and intensive computation are required (Zhou & Hu, 2008).

C. **Hybrid tracking systems:** These combine the advantages of marker and mark-free systems and, therefore, they can achieve higher accuracy. For instance, the boundaries of body segments can still be captured when not all of the markers on the segments are in the field of view of the cameras.

Nevertheless, intensive calibration and computation is required (Tao, Hu, Park, & Kingdom, 2003).

In summary, despite their advantages and reasonably good accuracy, camera-based systems are not well suited to home use because of the need to carefully place multiple cameras, which is not possible in most living accommodation, and also the complexity of the setup procedures.

2.2.2 Robot-aided tracking systems

Robot-aided tracking refers to the use of sensors that are embedded in a rehabilitation robot or exoskeleton that is being used to guide and support the patient's limb. These track the motion of the robot and, hence, indirectly the motion of the patient's limb. Therefore, the measurement variables are usually the robot joint angles, which are used to derive limb kinematics. Typical sensor technologies include rotary potentiometers and encoders (see (Hillman, 2004; Speich & Rosen, 2004) for more information).

2.2.3 Non-visual tracking systems

These systems normally use sensors attached to the human body to collect movement information. These sensors are commonly classified as mechanical, inertial, acoustic, radio or microwave, or magnetic. Each type of sensor has its own advantages and disadvantages. The advantages of on-body sensors include small size, low cost, and they do not suffer from the line-of-sight (occlusion) problems that visual systems do; so they are more likely to be suitable for rehabilitation technologies designed for home environments. However, they are usually less accurate, can suffer from drift problems (or errors in the absolute reference system) and difficulties in making the outputs anatomically relevant.

There are different kinds of sensors of non-visual based tracking such as inertial sensors, magnetic-inertial sensors, magnetic sensors which use an artificially generated magnetic field, goniometers which are typically based on bend sensors, and other non-commercial systems. One of the more promising on-body sensor technologies is the Magnetic and Inertial Measurement Unit (MIMU),

which is discussed below and its use for tracking upper-limb motion is the focus of this PhD.

2.3 Measuring upper-limb motion using MIMUs

2.3.1 Overview

A MIMU sensor consists of a 3D accelerometer, a 3D gyroscope, and a 3D magnetometer. The accelerometer signal is the sum of the absolute acceleration vector and the gravity vector (negated). Under static conditions, an accelerometer can be used for measuring inclination (Henk J Luinge & Veltink, 2004; O'Donovan, Kamnik, O'Keeffe, & Lyons, 2007). The gyroscope measures angular velocity, however, it suffers from drift effects when angular velocity is integrated in order to obtain orientation (H. J. Luinge & Veltink, 2005). The magnetometer measures a magnetic field and can therefore measure the sensor's heading relative to North (Roetenberg, Luinge, Baten, & Veltink, 2005; Schiefer et al., 2014). A drift-free 3D orientation output can be provided by using a sensor fusion algorithm that combines the three outputs (i.e. the acceleration, angular velocity, and magnetic field vectors) to provide the 3D orientation of the sensor-fixed coordinate system (SCS) with respect to the earth (global)-fixed coordinate system (GCS). This output can be presented in many different forms, for example: The Unit Quaternion (Euler parameters); Euler angles (roll, pitch, yaw); and the rotation matrix (direction cosine matrix).

MIMUs have been used as an alternative to camera-based motion capture systems for tracking upper-limb kinematics, especially in real life environments where the use of multiple cameras is not practical (B Morrow et al., 2017; Cutti et al., 2010; Favre, Aissaoui, Jolles, de Guise, & Aminian, 2009; Ferrari et al., 2010; Lin & Kulić, 2012; T. Liu, Inoue, & Shibata, 2009; Newman et al., 2017; Picerno, Cereatti, & Cappozzo, 2008; Walmsley et al., 2018). Furthermore, MIMUs are not subject to a restricted measurement volume or occlusion problems.

Hence, the application of MIMUs in upper-limb rehabilitation has been the subject of significant research over the last 10 years (Cutti, Giovanardi, Rocchi, Davalli,

& Sacchetti, 2008; de Vries, Veeger, Cutti, Baten, & van der Helm, 2010; Galinski & Dehez, 2012; H. J. Luinge, Veltink, & Baten, 2007; Pérez et al., 2010; Picerno et al., 2008; Plamondon et al., 2007; Luca Ricci et al., 2014).

2.3.2 Defining upper-limb kinematics

Many studies have worked to propose a set of standards to define segment and joint coordinate systems for both the upper- and lower-limb. However, most the studies have focused on the lower-limb (Grood & Suntay, 1983; Wu & Cavanagh, 1995; Wu et al., 2002). The ISB (International Society of Biomechanics) standard for the representation of upper limb kinematics is based on Grood and Suntay's joint coordinate system of the knee joint (Grood & Suntay, 1983). The ISB standard for the thorax, shoulder, elbow joint, and wrist joint (Wu et al., 2005) are presented in detail in chapter 3 section 3.3.3, but in this section the general issues addressed by the standard are described.

2.3.2 The anatomical calibration problem

The relative orientation of adjacent body segments, and hence the kinematics of shoulder, elbow and wrist joints, can be calculated from orientation data measured by MIMU sensors attached to each body segment of interest. However, the MIMU orientation data cannot be interpreted anatomically unless the orientations of the MIMUs are known with respect to their corresponding segment anatomical coordinate systems. Therefore, an appropriate calibration must be performed to obtain the relationships between each MIMU sensor coordinate system (SCS) and its corresponding segment local (anatomical) coordinate system (LCS) (Bouvier, Duprey, Claudon, Dumas, & Savescu, 2015; de Vries et al., 2010). The sensor-to-segment calibration procedure consists of the following steps: (1) positioning MIMU sensors on the thorax, upper-arm, forearm, and hand; (2) defining an LCS for each body segment; and (3) expressing the orientation of the LCS with respect to the sensor coordinate system (SCS).

To define a segment local (anatomical) coordinate system (LCS), two anatomical reference vectors are used, one primary (v_{ref1}) and one secondary (v_{ref2}).

These reference vectors are unit vectors and they are non-aligned and non-orthogonal. To construct the LCS, v_{ref1} is used as one of the coordinate system axes. A second axis is obtained from the vector cross product of v_{ref1} and v_{ref2}. Finally, the third axis is obtained from the vector cross product of the first two axes. In this way the chosen axes assure the orthogonality of the LCS. The general mathematical approach of this method may proceed as follows (Equations 2.1 to 2.3):

$${}^{S}X_{LCS} = v_{ref1} \tag{2.1}$$

$${}^{S}Y_{LCS} = \frac{v_{ref2} \times {}^{S}X_{LCS}}{\left| v_{ref2} \times {}^{S}X_{LCS} \right|} \tag{2.2}$$

$${}^{S}Z_{LCS} = {}^{S}X_{LCS} \times {}^{S}Y_{LCS} \tag{2.3}$$

In this notation the subscript signifies the coordinate system to which the axis belongs, and the preceding superscript signifies that the axis is expressed in the sensor coordinate system. Note that the sequence of the cross products can vary depending on: a) which coordinate system axis is defined by v_{ref1} (the **X**-axis in the example above); and b) which plane is defined by v_{ref1} and v_{ref2} (the **Z-X** plane in the example above, the **Y**-axis being perpendicular to that). This sensor to body segment calibration process is described in more detail in section 4.2 (chapter 4).

Only a small number of studies have investigated the use of MIMU sensors for tracking the kinematics of the upper-limb in an anatomically relevant way. These studies have mainly focused on tracking the kinematics of the upper-arm (humerus) (e.g. (Coley et al., 2007)), the thorax and upper-arm (humerothoracic) (e.g. (Bachmann, McGhee, Yun, & Zyda, 2001)), and elbow (e.g. (Bachmann et al., 2001; H. J. Luinge et al., 2007; Zhou, Stone, Hu, & Harris, 2008)). Using the upper-arm as an example (Figure 2.3), v_{ref1} and v_{ref2} may be obtained from static calibrations (based on the gravity vector in a defined arm position) and dynamic calibrations (based on a functional movement). (de Vries et al., 2010; H. J. Luinge et al., 2007), both used dynamic movement of the upper-arm (internal-external rotation) to define v_{ref1}. (de Vries et al., 2010), used elbow flexion-

extension to define v_{ref2} (using data from the forearm's sensor), whereas (H. J. Luinge et al., 2007) used a static calibration to define v_{ref2}. Alternatively, (Cutti et al., 2008) used careful positioning of the sensor on the upper-arm to align the sensor axes with the anatomical axes, thus avoiding the need for any further calibration procedures.
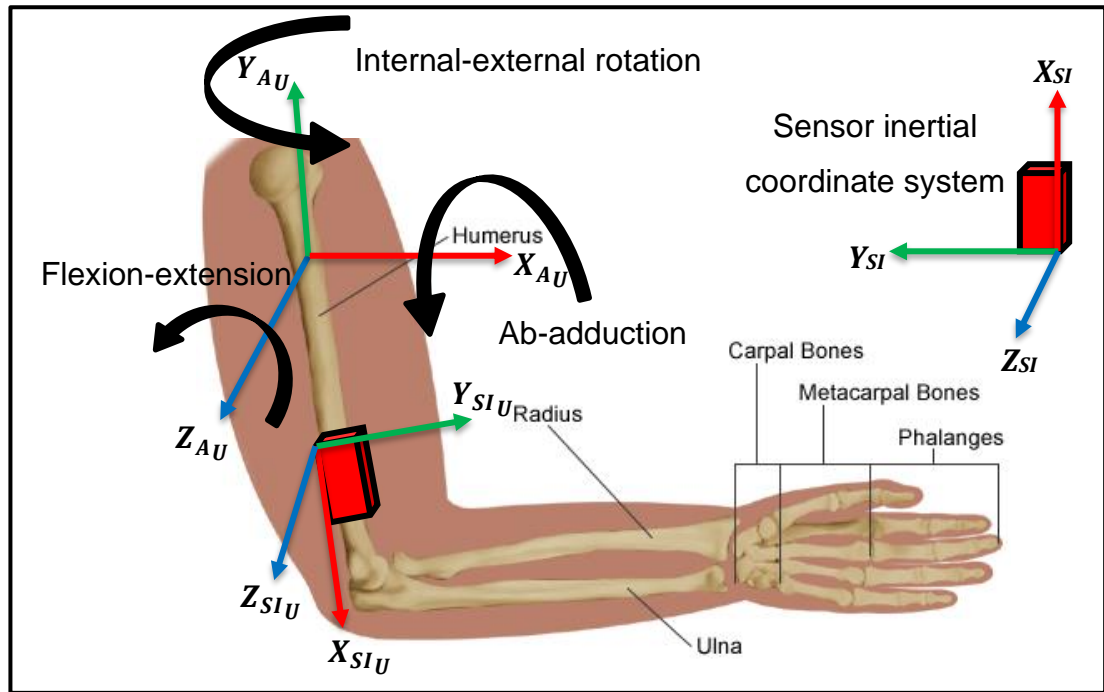
Figure 2.3: Upper-arm coordinate system and definition of motions

2.3.3 A review of calibration methods

Importantly, the anatomical calibration problem is still an open research question because no study has comprehensively compared alternative approaches to determine the best calibration method. In particular, no study has compared the many alternative methods of defining the two reference vectors (v_{ref1} and v_{ref2}). For this reason, a literature review was undertaken to establish the calibration methods used by other researchers in upper-limb applications and, hence, inform the author's work. The databases that were searched include: Web of Science, Google Scholar, and PubMed. A critical comparison was then made of the alternative methods.

The anatomical calibration methods found were classified as involving one or more of the following: (1) anatomical alignment of sensors; (2) static

measurements; or (3) dynamic measurements. Anatomical alignment involves aligning the sensor axes with anatomical axes defined by bony landmarks such as the styloid processes, humeral epicondyles, and humeral tubercle. Static measurements involve positioning the arm in a known posture and using the gravity vector (measured by the 3-axis accelerometer) to achieve anatomical calibration. Dynamic measurements involve moving a joint in a defined way and using the angular velocity vector (measured by the 3-axis rate-gyro) to achieve anatomical calibration. Table 2.2 below shows the alternative methods found and, in particular, how the two reference vectors have been defined by other researchers.

Table 2.2: Calibration methods

Ref	Segment	Reference vector	Note	Axis	Anatomical direction	Calibration method
(H. J. Luinge et al., 2007)	Upper-arm	$v_{ref1} = -\dfrac{\omega_{Ext}}{|\omega_{Ext}|} = \dfrac{\omega_{Int}}{|\omega_{Int}|}$	Internal-external rotation	Y	Superiorly	Dynamic
		$v_{ref2} = \dfrac{g_{Start} \times g_{End}}{|g_{Start} \times g_{End}|}$	Abduct the upper arm while keeping the elbow fixed. The direction of the z-axis can be found using the gravity at the start and end of the abduction movement	$\tilde{Z}$	Posteriorly	Dynamic
	Forearm	$v_{ref1} = -\dfrac{\omega_{Sup}}{|\omega_{Sup}|} = \dfrac{\omega_{pron}}{|\omega_{pron}|}$	Pronation-supination	Y	Superiorly	Static
		$v_{ref2} = -\dfrac{g}{|g|}$	Holding the palm of the hand downwards, it is assumed that the z-axis of the forearm coordinate system points in the vertical direction at the beginning and end of each trial	$\tilde{Z}$	Posteriorly	Static

Table 2.2: Calibration methods (Continued…)

Ref	Segment	Reference vector	Note	Axis	Anatomical direction	Calibration method
(Cutti et al., 2008)	Thorax	$v_{ref1} = -\dfrac{g}{|g|}$	Standing straight	Y	Superiorly	Static
		$v_{ref2} = \dfrac{Y \times [0\ 0\ 1]}{|Y \times [0\ 0\ 1]|}$	Rigorous positioning of MIMU	X	Laterally to the right	Alignment
	Upper-arm	$v_{ref1} = -\dfrac{\omega_{Ext}}{|\omega_{Ext}|} = \dfrac{\omega_{Flex}}{|\omega_{Flex}|}$	Elbow flexion-extension, keeping a constant pro-sup and the upper-arm alongside the body	X	Laterally to the right	Dynamic
		$v_{ref2} = Y$		Y	Superiorly	Alignment
	Forearm	$v_{ref1} = -\dfrac{\omega_{Sup}}{|\omega_{Sup}|} = \dfrac{\omega_{pron}}{|\omega_{pron}|}$	Upper-arm alongside the body, elbow flexed at 90º, forearm pronation-supination	Y	Superiorly	Dynamic
		$v_{ref2} = \dfrac{Y \times [0\ 0\ 1]}{|Y \times [0\ 0\ 1]|}$	Rigorous positioning of MIMU	X	Laterally to the right	Alignment

Table 2.2: Calibration methods (Continued...)

Ref	Segment	Reference vector	Note	Axis	Anatomical direction	Calibration method
(Bonnet, Bassom pierre, Godin, Lesecq, & Barraud, 2009)	Forearm	$v_{ref1} = \dfrac{\omega_{Sup}}{\left|\omega_{Sup}\right|} = -\dfrac{\omega_{pron}}{\left|\omega_{pron}\right|}$	Forearm pronation-supination	X	Inferiorly	Dynamic
		$v_{ref2} = -\dfrac{\omega_{Ext}}{\left|\omega_{Ext}\right|} = \dfrac{\omega_{Flex}}{\left|\omega_{Flex}\right|}$	Elbow flexion-extension	Y	Laterally to the right	Dynamic
(de Vries et al., 2010)	Thorax	$v_{ref1} = -\dfrac{g}{\left|g\right|}$	Standing straight	$\widetilde{Y}$	Superiorly	Static
		$v_{ref2} = \dfrac{\omega_{Ext}}{\left|\omega_{Ext}\right|} = -\dfrac{\omega_{Flex}}{\left|\omega_{Flex}\right|}$	Forward flexion – backward extension	Z	Laterally to the right	Dynamic
	Upper-arm	$v_{ref1} = -\dfrac{\omega_{Ext}}{\left|\omega_{Ext}\right|} = \dfrac{\omega_{Int}}{\left|\omega_{Int}\right|}$	Elbow flexed at 90°, internal-external rotation	Y	Superiorly	Dynamic

Table 2.2: Calibration methods (Continued…)

Ref	Segment	Reference vector	Note	Axis	Anatomical direction	Calibration method
(de Vries et al., 2010)	Upper-arm	$v_{ref2} = \dfrac{\omega_{Ext}}{\lvert\omega_{Ext}\rvert} = -\dfrac{\omega_{Flex}}{\lvert\omega_{Flex}\rvert}$	Upper-arm alongside the body, elbow flexion – extension. The data from MIMU on forearm is expressed in the coordinate system of the MIMU on the upper-arm	$\widetilde{Z}$	Laterally to the right	Dynamic
	Forearm	$v_{ref1} = -\dfrac{\omega_{Sup}}{\lvert\omega_{Sup}\rvert} = \dfrac{\omega_{pron}}{\lvert\omega_{pron}\rvert}$	Forearm pronation-supination	Y	Superiorly	Dynamic
		$v_{ref2} = \dfrac{\omega_{Ext}}{\lvert\omega_{Ext}\rvert} = -\dfrac{\omega_{Flex}}{\lvert\omega_{Flex}\rvert}$	Elbow flexion-extension	$\widetilde{Z}$	Laterally to the right	Dynamic
	Hand	$v_{ref1} = -\dfrac{g}{\lvert g\rvert}$	Keep hand flat on a table	X	Anteriorly	Static
		$v_{ref2} = -\dfrac{\omega_{Ext}}{\lvert\omega_{Ext}\rvert} = \dfrac{\omega_{Flex}}{\lvert\omega_{Flex}\rvert}$	The forearm and hand flat on a table, and perform dorsal flexion of the hand or hand extension	$\widetilde{Z}$	Laterally to the right	Dynamic

Table 2.2: Calibration methods (Continued…)

Ref	Segment	Reference vector	Note	Axis	Anatomical direction	Calibration method
(Yang & Ye, 2011)	Upper-arm	$v_{ref1} = -\dfrac{\omega_{Ext}}{|\omega_{Ext}|} = \dfrac{\omega_{Flex}}{|\omega_{Flex}|}$	Shoulder flexion-extension	Y	Laterally to the right	Dynamic
		$v_{ref2} = -\dfrac{g_{Start} \times g_{End}}{|g_{Start} \times g_{End}|}$	Shoulder abduction-adduction	$\widetilde{Z}$	Anteriorly	Static
	Forearm	$v_{ref1} = \dfrac{g}{|g|}$	Upper-limb is stretched away from the body (abducted to 90°) and the palm faces downward	$\widetilde{Y}$	Anteriorly	Static
		$v_{ref2} = -\dfrac{\omega_{Sup}}{|\omega_{Sup}|} = \dfrac{\omega_{pron}}{|\omega_{pron}|}$	Upper-limb is stretched away from the body (abducted to 90°) and the palm faces downward, then pronation-supination of the forearm about 180°	X	Inferiorly	Dynamic
	Hand	$v_{ref1} = \dfrac{g}{|g|}$	Upper-limb is stretched away from the body (abducted to 90°) and the palm faces downward	$\widetilde{Y}$	Anteriorly	Static

Table 2.2: Calibration methods (Continued…)

Ref	Segment	Reference vector	Note	Axis	Anatomical direction	Calibration method
(Yang & Ye, 2011)	Hand	$v_{ref2} = -\dfrac{\omega_{Sup}}{\lvert\omega_{Sup}\rvert} = \dfrac{\omega_{pron}}{\lvert\omega_{pron}\rvert}$	Upper-limb is stretched away from the body (abducted to 90º) and the palm faces downward, then pronation-supination of the forearm about 180º	X	Inferiorly	Dynamic
(Prayudi & Kim, 2012)	Upper-arm, forearm, and hand	${}^{S}q_J = \left({}^{G}q_S\right)^{-1} \otimes {}^{G}q_J$	T-pose (arms are placed horizontally with thumbs point forward). During pre-defined pose (T-pose as predefined pose), it has been assumed that all joints have the same orientation with respect to GCF. This study used quaternion method to find the relationship between SCF and JCS, and eventually to find JCS with respect to GCS.			Static

Table 2.2: Calibration methods (Continued…)

Ref	Segment	Reference vector	Note	Axis	Anatomical direction	Calibration method
(Parel et al., 2012)	Thorax	$v_{ref1} = \dfrac{g}{\|g\|}$	Standing straight	Y	Superiorly	Static
	Upper-arm	$v_{ref1} = -\dfrac{g}{\|g\|}$	Standing straight, upper-arm perpendicular to the ground and in neutral rotation	Y	Superiorly	Static
	Forearm	$v_{ref1} = -\dfrac{g}{\|g\|}$	Standing straight, elbow flexed at 90º in neutral forearm rotation	Z	Laterally to the right	Static
(Vignais et al., 2013)	Thorax	$v_{ref1} = \dfrac{g}{\|g\|}$	Standing straight	Z	Inferiorly	Static
		$v_{ref2} = \dfrac{g_{Start} \times g_{End}}{\|g_{Start} \times g_{End}\|}$	Forward flexion	X	Laterally to the right	Static
	Upper-arm	$v_{ref1} = \dfrac{g}{\|g\|}$	Neutral pose (standard anatomical position)	Z	Inferiorly	Static

Table 2.2: Calibration methods (Continued…)

Ref	Segment	Reference vector	Note	Axis	Anatomical direction	Calibration method
(Vignais et al., 2013)	Upper-arm	Using magnetometer	All local body frames are aligned with the global body frame	X & Y	Laterally to the right & posteriorly	Static
	Forearm	$v_{ref1} = \dfrac{g}{|g|}$	Neutral pose (standard anatomical position)	Z	Inferiorly	Static
		Using magnetometer	All local body frames are aligned with the global body frame	X & Y	Laterally to the right & posteriorly	Static
(L. Ricci et al., 2013, 2014)	Thorax	$v_{ref1} = -\dfrac{g}{|g|}$	Supine position	Z	Anteriorly	Static
		$v_{ref2} = \dfrac{\omega_{Rr}}{|\omega_{Rr}|} = -\dfrac{\omega_{Rl}}{|\omega_{Rl}|}$	Axial rotation	X	Inferiorly	Dynamic
		$v_{ref3} = -\dfrac{\omega_{Ext}}{|\omega_{Ext}|} = \dfrac{\omega_{Flex}}{|\omega_{Flex}|}$	Flexion-extension	Y	Laterally to the left	Dynamic

Table 2.2: Calibration methods (Continued…)

Ref	Segment	Reference vector	Note	Axis	Anatomical direction	Calibration method
(L. Ricci et al., 2013; Luca Ricci et al., 2014)	Upper-arm	$v_{ref1} = -\dfrac{g}{|g|}$	Supine position with arms alongside the body and palms facing down	Y	Anteriorly	Static
		$v_{ref1} = -\dfrac{\omega_{Abd}}{|\omega_{Abd}|} = \dfrac{\omega_{Add}}{|\omega_{Add}|}$	Abduction-adduction	Y	Anteriorly	Dynamic
		$v_{ref2} = -\dfrac{\omega_{Ext}}{|\omega_{Ext}|} = \dfrac{\omega_{Flex}}{|\omega_{Flex}|}$	Flexion-extension	Z	Laterally to the right	Dynamic
		$v_{ref2} = -\dfrac{\omega_{Ext}}{|\omega_{Ext}|} = \dfrac{\omega_{Flex}}{|\omega_{Flex}|}$	Flexion-extension while holding a bar with hands at shoulder breadth with an adducted thumb grasp	Z	Laterally to the right	Dynamic
	Forearm	$v_{ref1} = -\dfrac{g}{|g|}$	Supine position with arms alongside the body and palms facing down	Z	Laterally to the right	Dynamic
		$v_{ref1} = -\dfrac{\omega_{Ext}}{|\omega_{Ext}|} = \dfrac{\omega_{Flex}}{|\omega_{Flex}|}$	Flexion-extension	Z	Laterally to the right	Dynamic

Table 2.2: Calibration methods (Continued…)

Ref	Segment	Reference vector	Note	Axis	Anatomical direction	Calibration method
(L. Ricci et al., 2013, 2014)	Forearm	$v_{ref2} = -\dfrac{\omega_{Sup}}{\|\omega_{Sup}\|} = \dfrac{\omega_{pron}}{\|\omega_{pron}\|}$	Pronation-supination with arms fully extended and hands closed	X	Inferiorly	Dynamic
		$v_{ref3} = -\dfrac{\omega_{Ext}}{\|\omega_{Ext}\|} = \dfrac{\omega_{Flex}}{\|\omega_{Flex}\|}$	Flexion-extension while holding a bar	Y	Anteriorly	Dynamic
(Bouvier et al., 2015)	Thorax	$v_{ref1} = -\dfrac{g}{\|g\|}$	Standing and sitting straight	Y	Superiorly	Static
	Upper-arm	$v_{ref1} = -\dfrac{g}{\|g\|}$	Upper-arm along the body in standing and sitting position	Y	Superiorly	Static
		$v_{ref2} = -\dfrac{\omega_{Ext}}{\|\omega_{Ext}\|} = \dfrac{\omega_{Int}}{\|\omega_{Int}\|}$	Internal-external rotation	Y	Superiorly	Dynamic
	Forearm	$v_{ref1} = -\dfrac{g}{\|g\|}$	Upper limbs along the body, in neutral forearm pronation-supination, fingers pointing downwards, in standing position	Y	Superiorly	Static
		$v_{ref2} = -\dfrac{g}{\|g\|}$	Elbow flexed at 90°, neutral forearm PS, fingers pointing forward, in sitting position	Z	Laterally to the right	Static

Table 2.2: Calibration methods (Continued…)

Ref	Segment	Reference vector	Note	Axis	Anatomical direction	Calibration method
(Bouvier et al., 2015)	Forearm	$v_{ref3} = -\dfrac{\omega_{Ext}}{\|\omega_{Ext}\|} = \dfrac{\omega_{Flex}}{\|\omega_{Flex}\|}$	Flexion-extension	X	Anteriorly	Dynamic
		$v_{ref1} = -\dfrac{\omega_{Sup}}{\|\omega_{Sup}\|} = \dfrac{\omega_{pron}}{\|\omega_{pron}\|}$	Pronation-supination	Y	Superiorly	Dynamic
	Hand	$v_{ref1} = -\dfrac{g}{\|g\|}$	Upper limbs along the body, in neutral forearm pronation-supination, fingers pointing downwards, in standing position	Y	Superiorly	Static
		$v_{ref2} = -\dfrac{g}{\|g\|}$	upper arm along the body, elbow flexed at 90°, in neutral forearm PS, fingers pointing forward, in sitting position	Z	Laterally to the right	Static
		$v_{ref3} = -\dfrac{g}{\|g\|}$	Hand flat on a table	X	Anteriorly	Static
		$v_{ref2} = -\dfrac{\omega_{Ext}}{\|\omega_{Ext}\|} = \dfrac{\omega_{Flex}}{\|\omega_{Flex}\|}$	Hand flat on a table, wrist extension	Z	Laterally to the right	Dynamic

It can be seen in Table 2.2 that studies varied in their approach to deriving the primary reference vector. Some studies used the angular velocity vector, generated by pre-defined rotation of a limb segment, while others used the orientation of the gravity vector to define the primary reference vector. The most common way to define the secondary axis relied on the user placing their upper limb in specific static postures and deriving the secondary vector from the measured gravity vector. However, in some cases, the primary and secondary reference vectors were both defined using angular velocity data. Also, all the studies relied on careful positioning of the MIMU with respect to the anatomical frame. It is clear from the studies summarised above that there is no commonly accepted approach to defining either reference vector.

No comparison of the alternatives shown in Table 2.2 has been found in the literature apart from that of (Bouvier et al., 2015), which did not cover all of the alternatives and only assessed accuracy and precision. (Bouvier et al., 2015), did not compare calibration methods in term of speed or simplicity to, for example, sensor misalignment. Furthermore, they did not include thorax orientation with respect to the GCS or LAB. In summary, no study has:

1) Included all segments of the upper-limb;

2) Compared all of the alternatives in Table 2.2 for defining the two reference vectors;

3) Made a comprehensive comparison covering accuracy, speed, and simplicity.

Therefore, this PhD undertakes a comprehensive and critical comparison of alternative calibration methods and finds the most appropriate anatomical calibration method for use in rehabilitation and other applications.

Chapter 3 – Experimental Methods

3.1 Introduction

If scapular motion and motion of the finger joints are excluded, the upper limb has seven degrees of freedom (DoF) (Miller et al., 2011), 3 at the shoulder (flexion-extension, adduction-abduction, internal-external rotations); 2 at the elbow (flexion-extension, pronation-supination); and 2 at the wrist (flexion-extension, ulnar-radial deviation). Capturing and describing the kinematics of the upper-limb is needed for a variety of applications in the field of rehabilitation. For example, upper limb segment motion measured using body-worn IMUs has been applied in the control of FES systems (Sun, 2014) and upper limb prosthetic systems (Merad, Roby-Brami, & Jarrasse, 2016). In addition, motion tracking devices for the upper limb have been used as part of a home-based rehabilitation system for stroke patients (Zhou, Hu, & Tao, 2006). Assessment of upper-limb joint coordination during activities has been used to quantify motor impairment following neurological injury (Murgia, Kerkhofs, Savelberg, & Meijer, 2010). Indeed, various upper limb kinematic measures are now used as metrics to quantify motor impairments following stroke (Kwakkel et al., 2019; Santisteban et al., 2016). It is worth noting that many of these approaches use camera-based systems to track joint angle trajectories.

Motion tracking systems based on stereo-photogrammetry provide high accuracy in tracking the position of markers on the body, which can be used to reconstruct other parameters, such as joint angle trajectories (A Cappozzo, 1983; Chiari, Della Croce, Leardini, & Cappozzo, 2005; Y Ehara, Fujimoto, Miyazaki, Tanaka, & Yamamoto, 1995; Yoshihiro Ehara et al., 1997). However, stereo-photogrammetry measurements require specialised personnel to run the expensive camera systems, and hence this largely restricts its use to the laboratory. Further, setup and analysis are time-consuming, and they rely upon good camera placements to ensure marker visibility.

The advent of Micro-Electro-Mechanical Systems (MEMS) technology allowed systems based on inertial and magnetic sensors to be used in biomedical

applications. These systems are potentially useful for measurements outside of a specialised laboratory, overcoming some of the limitations of camera based systems (Mancini, Zampieri, Carlson-Kuhta, Chiari, & Horak, 2009). However, to measure the relative motion between two adjacent body segments and hence derive clinically meaningful joint angle trajectories, using MIMUs, anatomical calibrations are needed. To compare the different calibration techniques published in the literature and to support future analysis methods, an experimental data set spanning all of the previously published methods for calibration, is required. To assess the different calibration methods, a set of functional tasks were also required. This chapter describes the experiment to capture the required data sets. The chapter begins with an overview of the two measurement systems, the stereophotogrammetry system and the MIMU measurement system. This is followed by a description of the experimental methods used to capture synchronous data on upper limb movement using both measurement systems. Section 3.5 describes the analysis of the data sets in preparation for the work presented in the following chapter. The chapter ends with a discussion section.

3.2 Measurement Systems

The two measurement systems (MIMUs and camera-based system – stereophotogrammetry system) are described below.

3.2.1 Magneto-Inertial Measurement Unit System (MIMUs)

Four MIMUs (MTx Motion Tracker, Xsens technologies B.V., Netherlands) were used. Each unit is a three Degree of Freedom (3-DoF) orientation tracker, providing drift-free three dimensional (3D) orientations (as quaternions, rotation matrices, or Euler angles) as well as the following raw sensor data: 3D acceleration, 3D rate of turn (rate gyro) and 3D earth-magnetic field (Roetenberg, Luinge, & Slycke, 2013). The MIMUs are connected to an Xbus Master, which in turn transmits data via a USB serial cable to a PC/laptop (see Figure 3.1). The

Xbus Master delivers power to the connected MIMUs and retrieves their data while they are sampled synchronously.
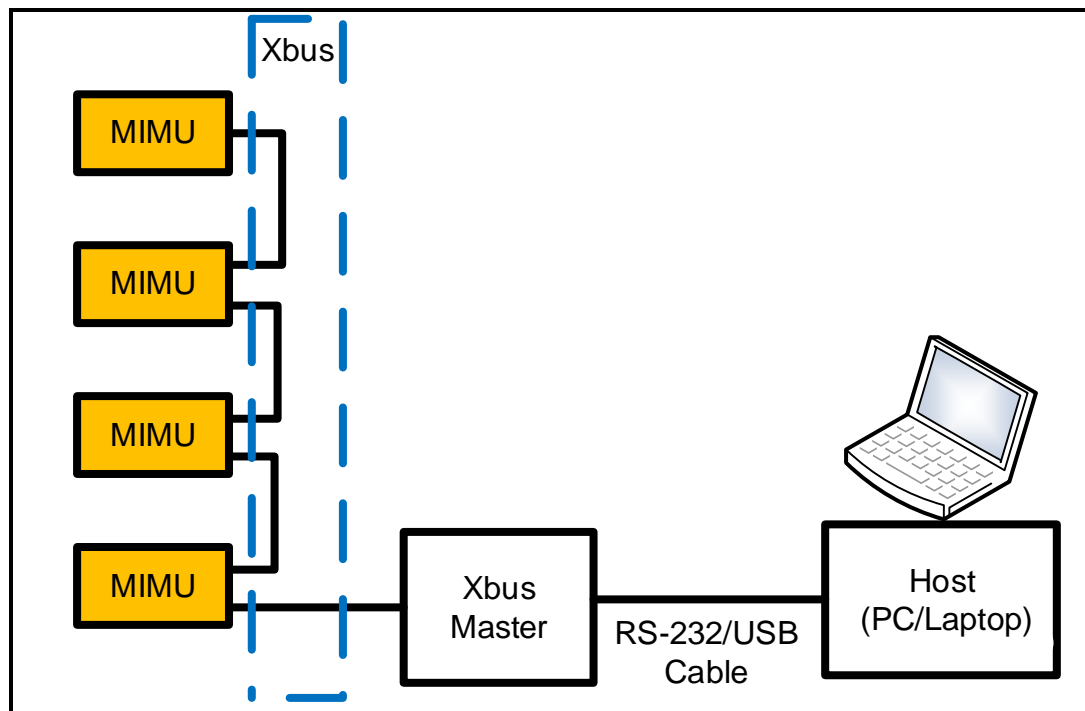
Figure 3.1: MIMU measurement system

A sensor fusion algorithm, developed by Xsens, calculates absolute orientation in 3D space in real-time from the raw 3-axis accelerometer, rate-gyroscope, and magnetometer data (see Figure 3.2). The algorithm utilizes measurement of gravity (3-axis accelerometer) and magnetic north (3-axis magnetometer) to compensate for ever increasing errors (drift) from the integration of errors in rate of turn (angular velocity). This type of drift compensation is called an Attitude and Heading Reference System (AHRS).
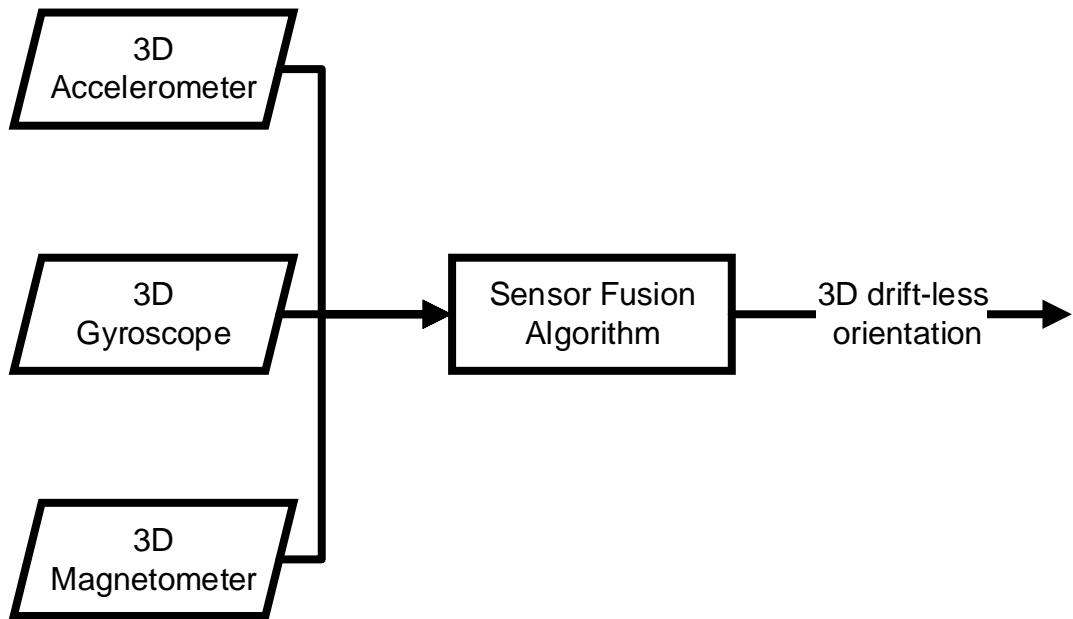
Figure 3.2: Sensor fusion

All MIMU sensor outputs (orientation, acceleration, rate of turn, and earth magnetic field) are expressed in the body-fixed right-handed sensor coordinate system (SCS) shown in Figure 3.3. The orientation of the sensor is measured with respect to a global (an earth) coordinate system (GCS) defined by the directions of gravity and magnetic north. It should be noted that the 3-axis accelerometer measures the sum of the free acceleration and gravity.
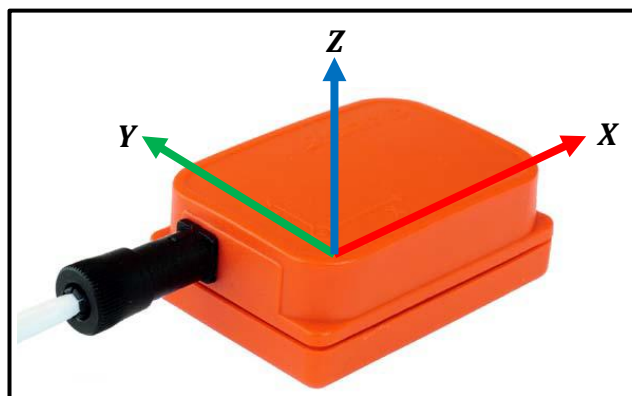
Figure 3.3: MIMU with sensor-fixed coordinate system (SCS) overlaid

The four MIMUs are connected together with Xbus cables, with the last in the chain connected to the Xbus Master (see Figure 3.4), allowing each MIMU to communicate its data to the laptop.
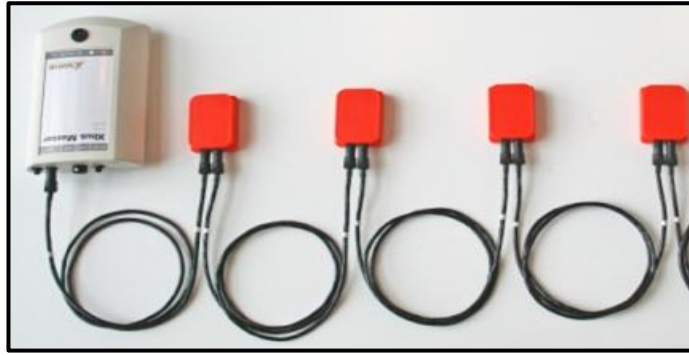
Figure 3.4: Xbus Master and MIMU sensors chain connection

3.2.2 Stereophotogrammetry System

Stereophotogrammetry is a technique that uses cameras to track the movements of reflective markers placed on the human body. When combined with a biomechanical model, the marker data can be used to reconstruct anatomically relevant parameters such as body postures and joint angle trajectories.

The stereophotogrammetry system used in this experimental work was VICON produced by Oxford Metrics company. The system includes 10 cameras positioned around the room on wall-mounted frame (see Figure 3.5)

Figure 3.5: Stereophotogrammetry measurement system

In addition, the stereophotogrammetry laboratory reference frame was identified using the static wand of precisely known geometry, placed over the corners of one of the force plates. Calibration of the capture volume used an active wand, which incorporates Light Emitting Diodes, the position of which are tracked

automatically in stereophotogrammetry software which is Nexus software. The same software was used for data collection.

Synchronisation between the two measurement systems was achieved as follows. The MIMUs system outputs an analogue rectangular pulse signal for synchronisation purposes, which indicates when MIMU recording starts and ends. This is fed to an analogue input channel in the stereophotogrammetry system, which then samples the signal in synchrony with capturing the camera frames. Figure 3.6 shows an example of this and the camera frames corresponding to the start and end of MIMU recording can be identified. Camera frames before and after MIMU recording are discarded.
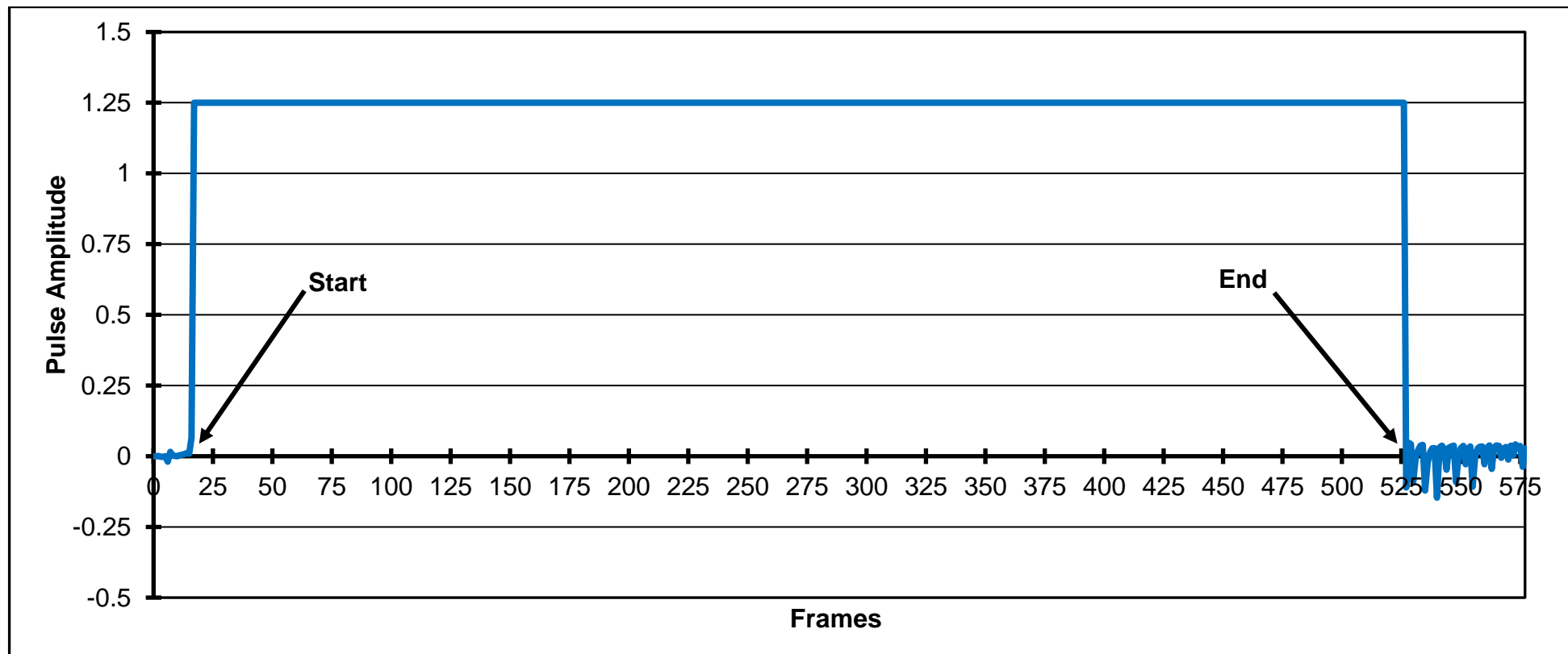
Figure 3.6: Synchronisation signal represents the start and the end of synchronisation frames for thorax axial movement – participant 1.

3.3 Measurement of upper limb motion using synchronised MIMUs and stereophotogrammetry

3.3.1 Introduction

The next sections explain the methods used to collect and process synchronous data from the MIMU and stereophotogrammetry systems. The section begins with an explanation of the placement of reflective markers and MIMUs on the participants. The following section describes the set of calibration movements, derived from Table 2.2 (Chapter 2), which were used to replicate previous studies' approaches to establish anatomical coordinate frames for MIMUs and use these data to estimate joint angles. It also describes the functional task trials used to evaluate the performance of the various calibration procedures. Section 3.5 describes the data analysis procedures, including building an upper-limb kinematic model.

The data processing reported in this section used the following software: Data from stereophotogrammetry system were processed using the Nexus 1.8.5 2013, Visual 3D v6.01.36 (2019) and MATLAB 9.6 2019a (The Math Work, USA). Data from the MIMU system were processed using MATLAB.

3.3.2 Marker and sensor placement and upper limb model - overview

In order to allow for subsequent comparison of data from the two measurement systems, markers were placed on both the anatomy and on the MIMUs. Clusters of markers on the MIMUs were used both to allow tracking of the MIMUs as well as to allow for the relative alignment of the MIMUs to the anatomical coordinate systems. The markers also served as technical clusters in the CAST analysis, described below.

The definition of the Anatomical Coordinate Systems (A) is based on an approach called CAST (Calibrated Anatomical Systems Technique) (A Cappozzo, Catani, Della Croce, & Leardini, 1995). The CAST technique uses a series of markers to track the motion of the body. The markers can be classified as either Anatomical Landmark markers, which can be used to identify joint axes, or technical markers, which are located in clusters of 3 or more on the limb segment itself. A static calibration is used to define a cluster marker technical frame (coordinate) (CTF) for each tracked segment, the relationship between this frame and the relevant anatomical coordinate frame, and the relationship between the anatomical coordinate frame and the lab frame.

Later in this chapter, the set of dynamic (functional) calibrations are described. In each dynamic calibration, the participant performs a well-defined uni-axial rotation while angular velocity readings are taken, which are used to determine a functional axis of rotation.

3.3.3 Upper-limb model

The model of the upper-limb to be used in subsequent data processing is defined according International Standard of Biomechanics (ISB) recommendation (Wu et al., 2005). The upper limb kinematic model is based on the assumptions that the thorax, upper-arm (humerus), forearm, and hand are rigid segments (Cutti et al., 2008; Wu et al., 2005) . Each segment has its associated anatomical coordinate system. The orientation of the thorax is computed with respect to the laboratory coordinate system, while the orientation of the humerus is computed with respect to the thorax; the forearm with respect to the humerus, and lastly the hand with respect to the forearm.

The model for the upper-limb, together with the locations of the markers, is described in Tables 3.1 to 3.4 and Figures 3.7 to 3.14.

Thorax

The thorax segment is defined using the markers listed in Table 3.1 and shown in Figure 3.7.

Table 3.1: Anatomical markers – Thorax

Thorax	
C7	Processus Spinosus (spinous process) of the 7th cervical vertebra.
T8**	Processus Spinosus (spinal process) of the 8th thoracic vertebra.
IJ**	Deepest point of Incisura Jugularis (suprasternal notch).
PX	Processus Xiphoideus (xiphoid process), most caudal point on the sternum.

** means that marker was used is bigger to increase the visibility.
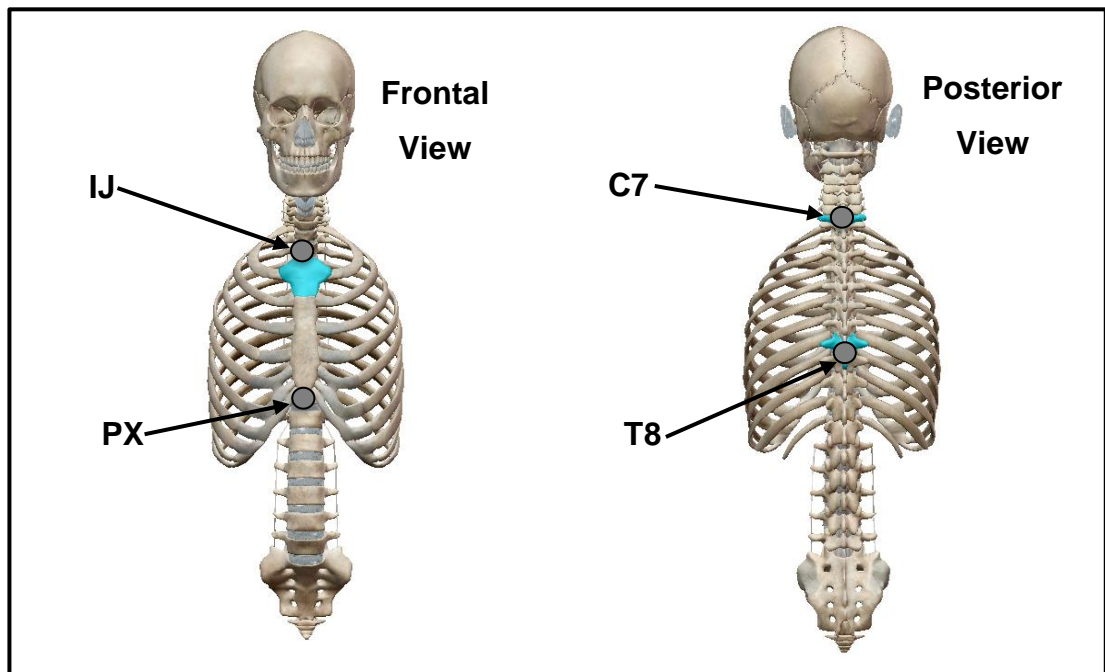
Figure 3.7: Anatomical bony landmarks for thorax

It is worth noting that C7 has an enlarged spinous process called a vertebra prominence. It is the most prominent structure that can be palpated when finger is passed downwards from the skull and easiest to identify with the head bent

forward. T8 was difficult to find, therefore, a physiotherapist was asked to check the placement. IJ is the deepest point of Incisura Jugularis which is the visible dip in between the neck and the two collarbones, and PX is at the end of the sternum.

Thorax kinematics are described by three independent angles: flexion-extension, lateral flexion, and axial rotation, relative to the laboratory frame, as shown in Figure 3.8.
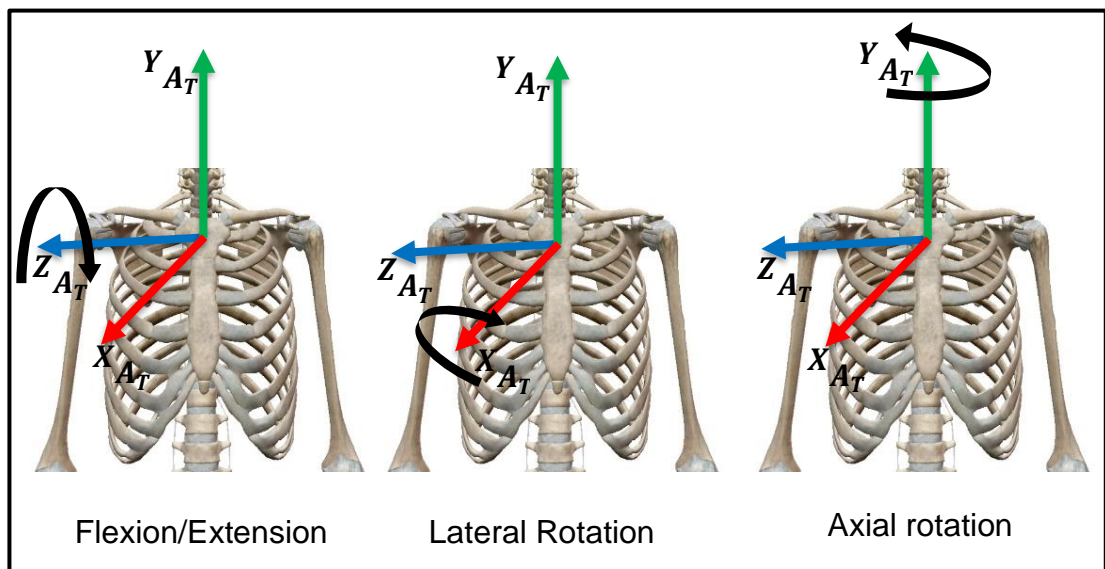
Figure 3.8: Anatomical local coordinate system with three independent orientations for thorax

The anatomical reference frame shown in Figure 3.8 has been defined following ISB recommendations, as follows:

Y_{A_T}: The line connecting the midpoint between PX and T8 and the midpoint between IJ and C7, pointing upward;

Z_{A_T}: The line perpendicular to the plane formed by IJ, C7, and the midpoint between PX and T8, pointing to the right;

X_{A_T}: The common line perpendicular to the Z_{A_T}- and Y_{A_T}-axis, pointing forward.

Upper arm

The upper arm segment is defined using the markers listed in Table 3.2 and shown in Figure 3.9.

Table 3.2: Anatomical markers – Upper-arm

Upper-arm	
RHA	Right Humerus anterior.
RHP	Right Humerus posterior.
RHAC (GH)	Right Humerus Acromion- Glenohumeral rotation centre.
LEH	Lateral Epicondyle of right humerus (elbow)- Most caudal point on lateral epicondyle.
MEH**	Medial Epicondyle of right humerus (elbow)- Most caudal point on medial epicondyle.

** means that marker used was larger to increase visibility.
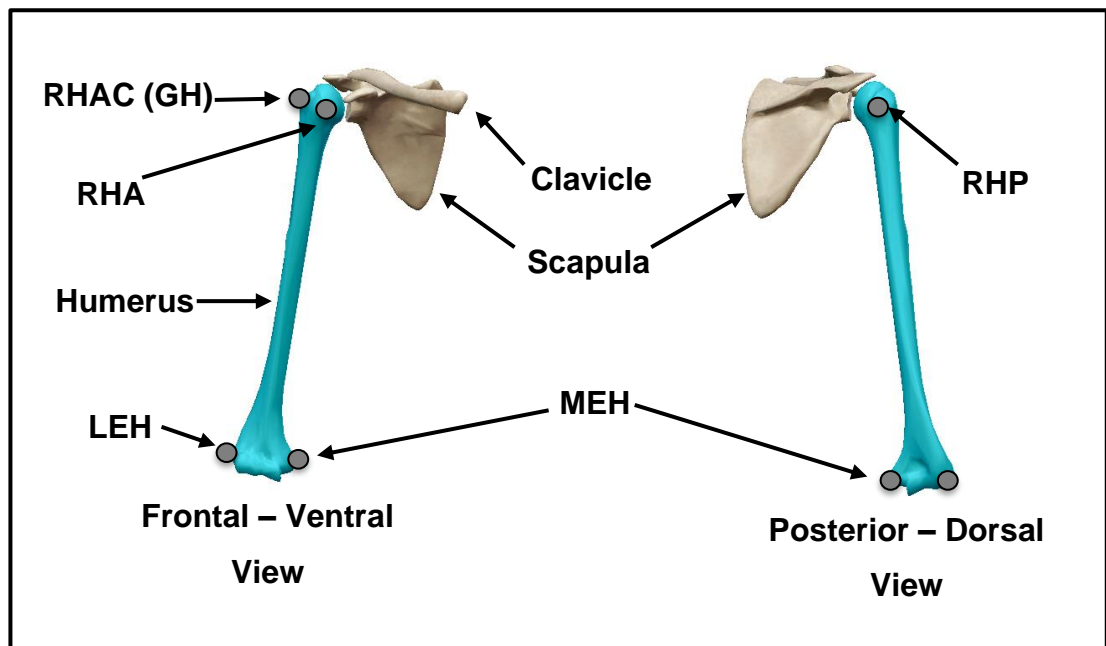
Figure 3.9: Anatomical Bony Landmarks for Right-Upper-arm

RHAC is the acromion which is palpable by following the clavicle laterally, it is the most dorsal point on the acromioclavicular joint. Next, RHA and RHP are anterior and posterior markers on the shoulder joint centre respectively. By flexing and extending the elbow joint, LEH and MEH can be found.

Humerothoracic (shoulder) kinematics are based on a ball and socket joint model (see Figure 3.10) and are described by three independent angles: flexion-extension, internal-external rotation, and abduction-adduction.
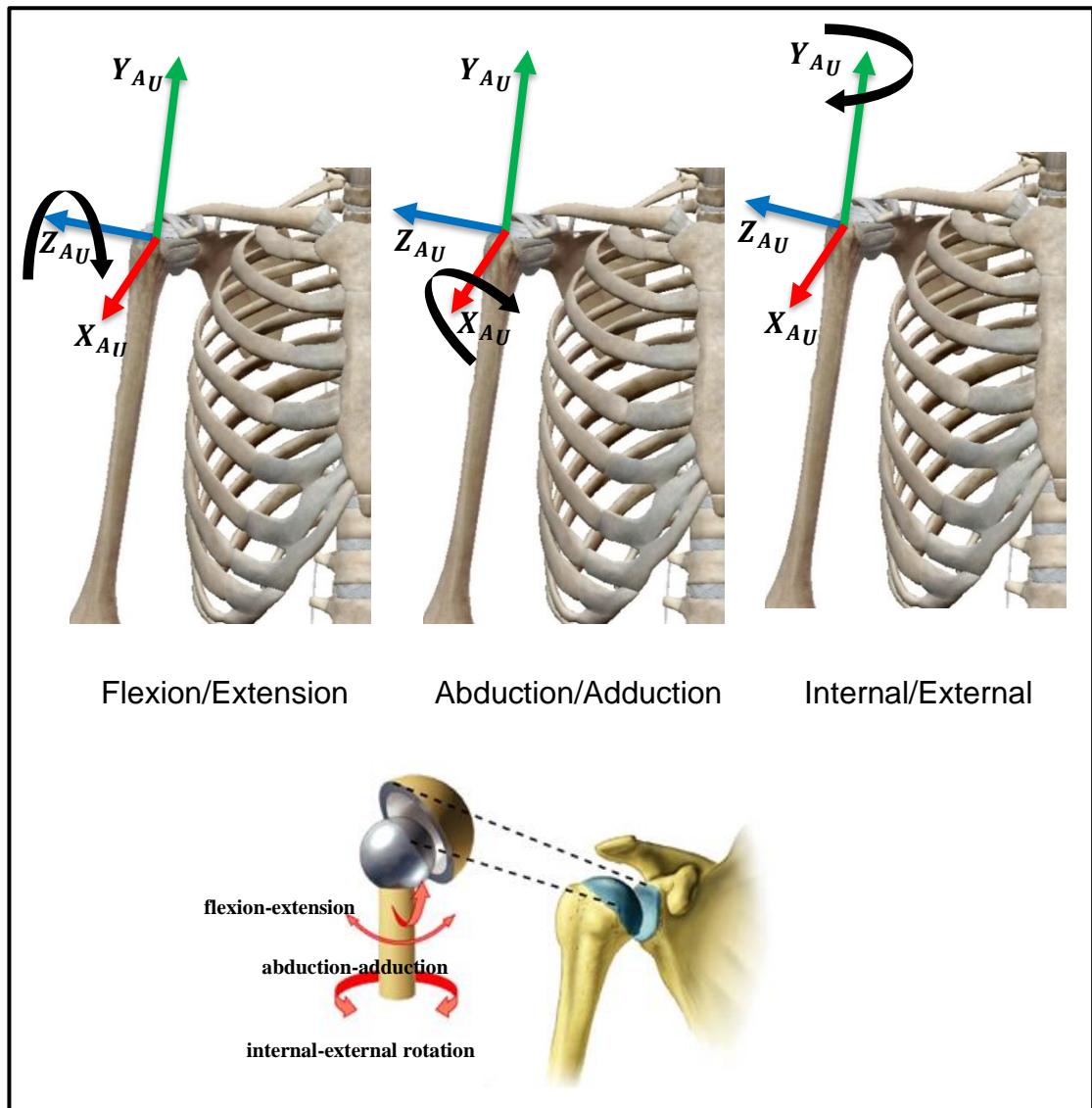
Figure 3.10: Anatomical local coordinate system with three independent orientations for upper-Arm and shoulder joint

The anatomical coordinate for upper-arm in Figure 3.10 can be defined as follow:

Y_{A_U}: The line connecting GH and the midpoint of LEH and MEH, pointing to GH;

X_{A_U}: The line perpendicular to the plane formed by LEH, MEH, and GH, pointing forward;

Z_{A_U}: The common line perpendicular to the Y_{A_U}- and Z_{A_U}-axis, pointing to the right.

Forearm

The forearm segment is defined using the markers in Table 3.3 and shown in Figure 3.11.

Table 3.3: Anatomical markers - Forearm

Forearm	
USP	Most caudal–medial point on the ulnar styloid.
RSP	Most caudal–lateral point on the radial styloid.
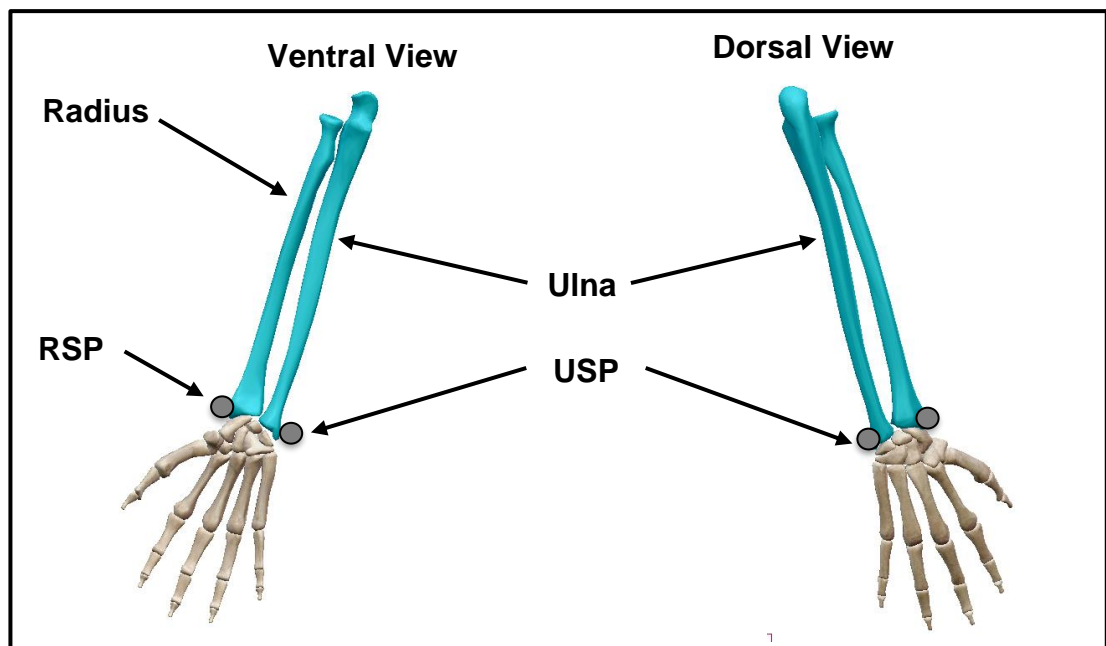
Figure 3.11: Anatomical bony landmarks for right-forearm

RSP and USP are the wrist markers, placed on the bony prominences most easily identified when the forearm flexed at 90° with respect to the upper-arm.

Elbow kinematics is described by two independent angles: flexion-extension and pronation-supination as shown in Figure 3.12.
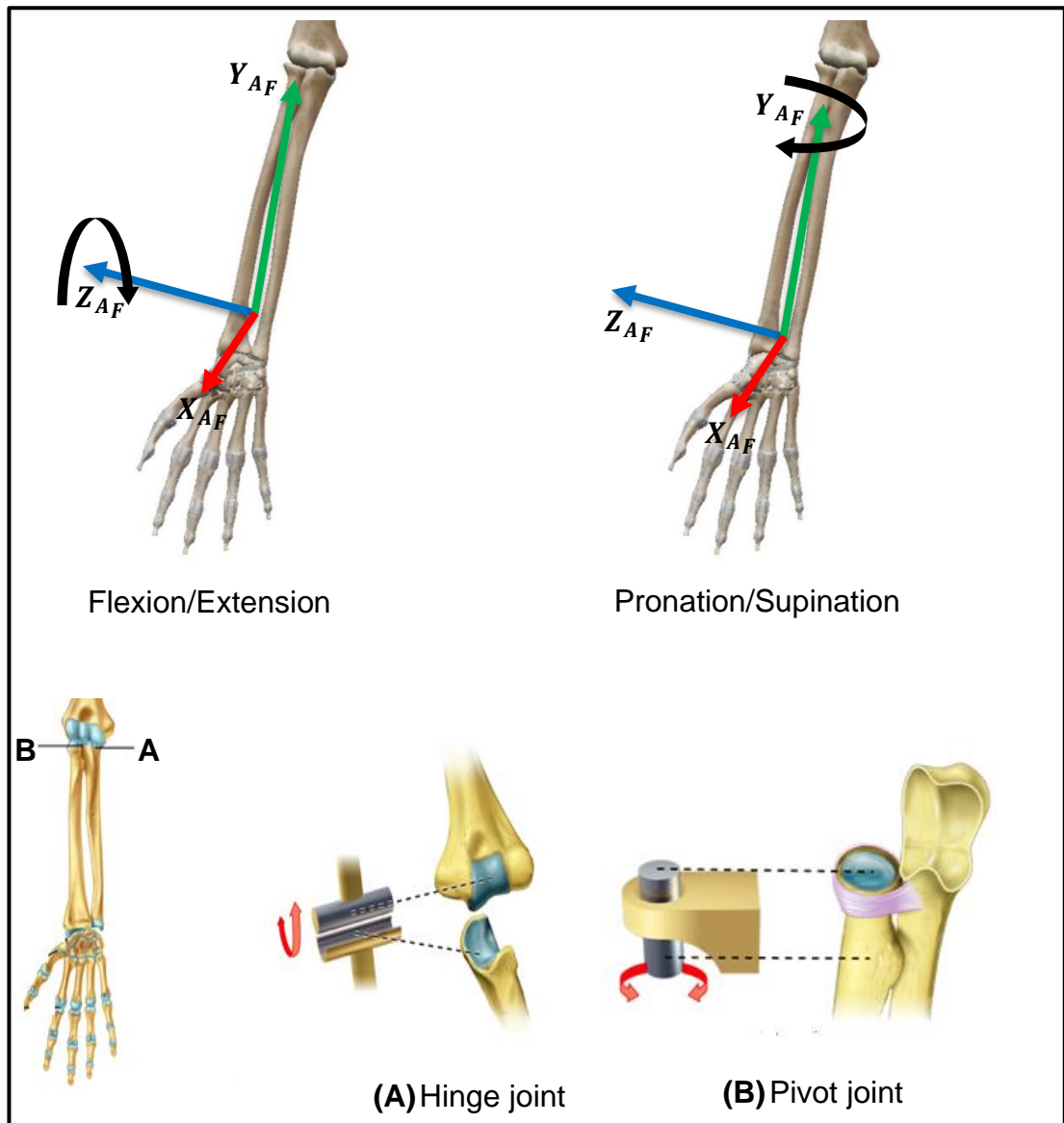
Figure 3.12: Anatomical Local Coordinate System with two Independent Orientations for Forearm and Elbow Joint

For forearm, the anatomical coordinate can be found as follow:

Y_{A_F}: The line connecting USP and the midpoint between LEH and MEH, pointing proximally;

X_{A_F}: The line perpendicular to the plane through USP, RSP, and the midpoint between LEH and MEH, pointing forward;

Z_{A_F}: The common line perpendicular to the X_{A_F}- and Y_{A_F}-axis, pointing to the right.

Hand and Wrist

The hand segment is defined by the set of markers in Table 3.4 and shown in Figure 3.13.

Table 3.4: Anatomical markers – Hand

Hand	
MCII	Most distal point of second metacarpal bone.
MCV	Most distal point of fifth metacarpal bone.
RCJ	Radial side of radiocarpal joint.
UCJ	Ulnar side of radiocarpal joint.
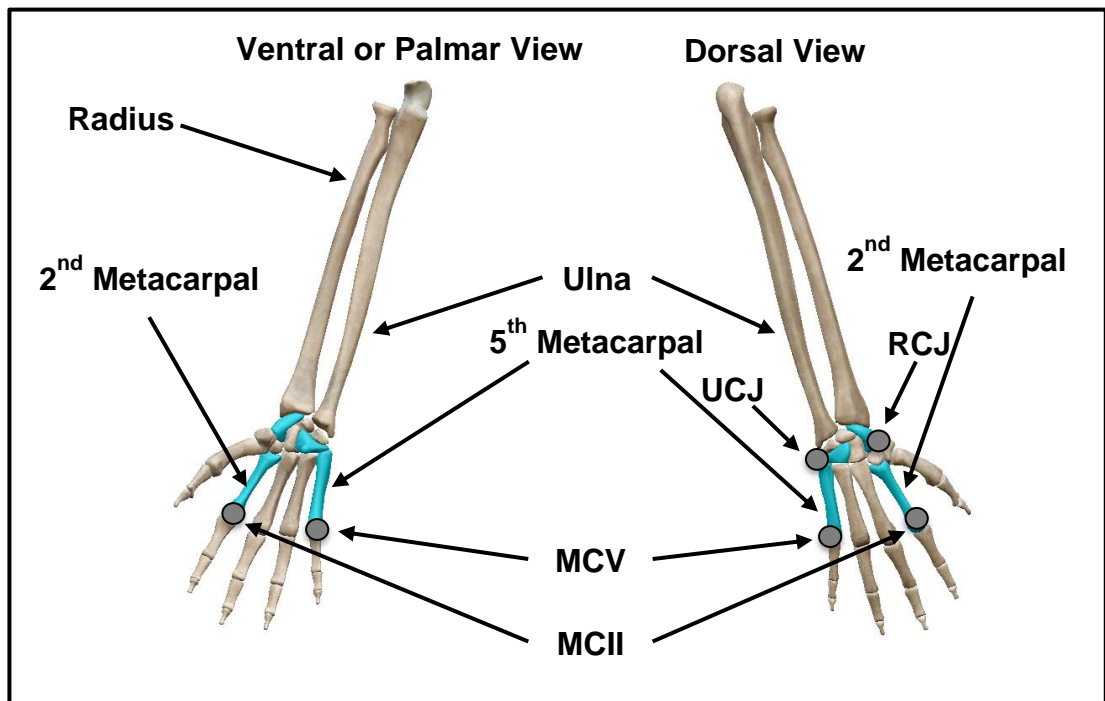
Figure 3.13: Anatomical bony landmarks for right-hand

UCJ and RCJ markers were placed on the radiocarpal joint on the projected extension of Ulna and Radius. Finally, MCII and MCV were easy to find when the hand was laid flat on the table.

Wrist kinematics are described by two angles: flexion-extension and ulnar deviation (ulnar flexion) or radial deviation (radial flexion) as shown in Figure 3.14.
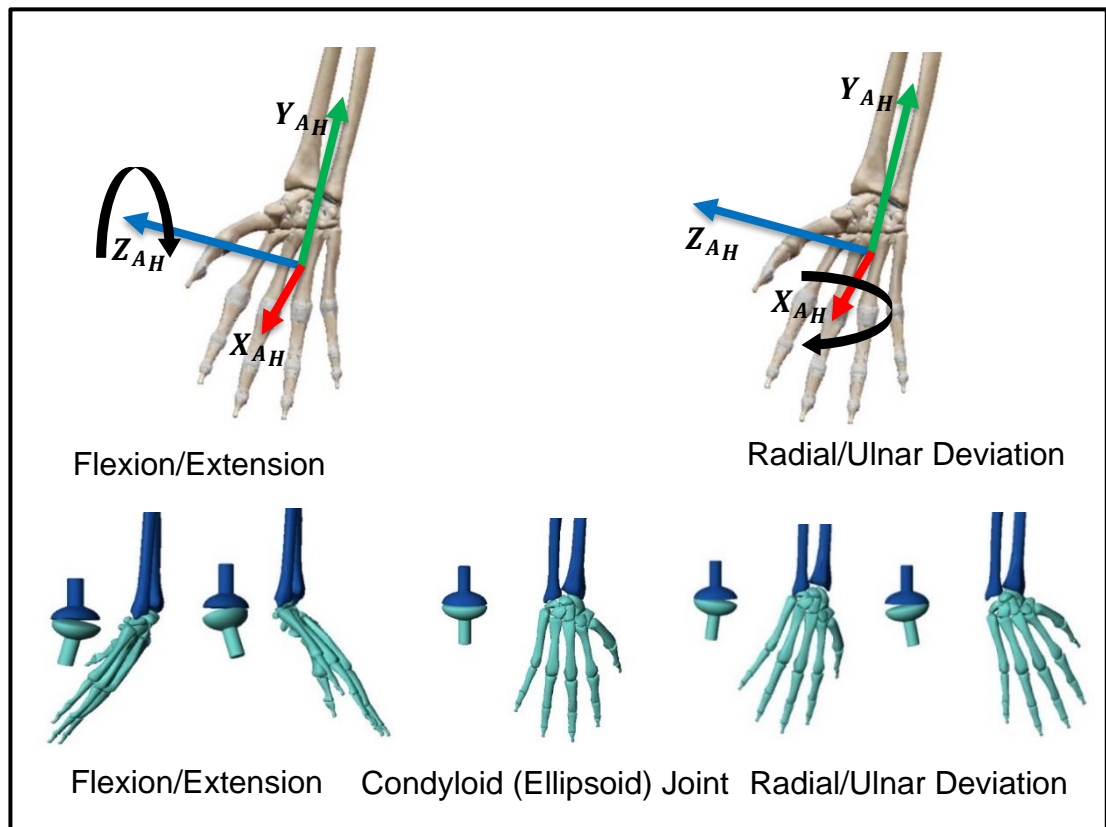
Figure 3.14: Anatomical local coordinate system with two independent orientations for hand and wrist joint

The anatomical coordinate for hand can be defined as follow:

Y_{A_H}:   The line parallel to Radius pointing proximally to LEH;

X_{A_H}:   The line perpendicular to the plane formed by USP, RSP, and LEH pointing forward;

Z_{A_H}:   The common line perpendicular to the X_{A_H}- and Y_{A_H}-axis, pointing to the right.

3.3.4 MIMU placements

Four MIMUs were placed on the thorax, upper-arm, forearm, and hand of each participant with double-sided sticky tape. Each MIMU also served as a convenient rigid body on which to mount markers used to define the cluster marker technical frame (coordinate) (CTF), see section 3.3.2. The cluster also allowed for a marker-based coordinate frame (referred to in Chapter 4 as Sensor Marker coordinate frame), approximately coincident with the MIMU inertial framework. The individual MIMUs were carefully located and orientated according to the descriptions in Tables 3.5 to 3.8, thereby manually aligning the MIMU and marker-based coordinate frames.

The MIMUs were placed as described in Tables 3.5 to 3.8.

Table 3.5: MIMUs placement – Thorax

	Thorax	
Position	On the flat portion of thorax-sternum. The precise location of the MIMU sensor on the sternum is participant dependent, because of soft tissue, sensor movement, and marker occlusion due to the chin.	
Alignment	The x-axis of the MIMU sensor is placed parallel with respect to the virtual line between the IJ and PX marker.	
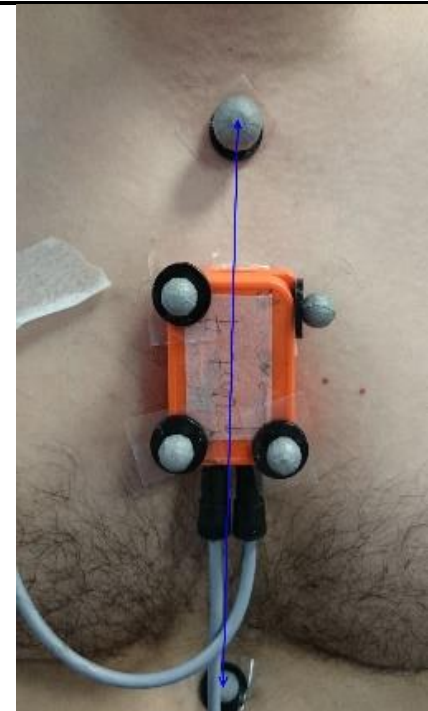
Table 3.6: MIMUs placement – Upper-arm

	Upper-arm	
Position	Latero-distally of the right upper-arm, just distal of the end of the deltoid muscle and proximal of the end of the brachialis muscle.	
Alignment	The x-axis of the MIMU sensor is placed parallel with respect to the virtual line between the acromion shoulder marker and the lateral elbow marker.	
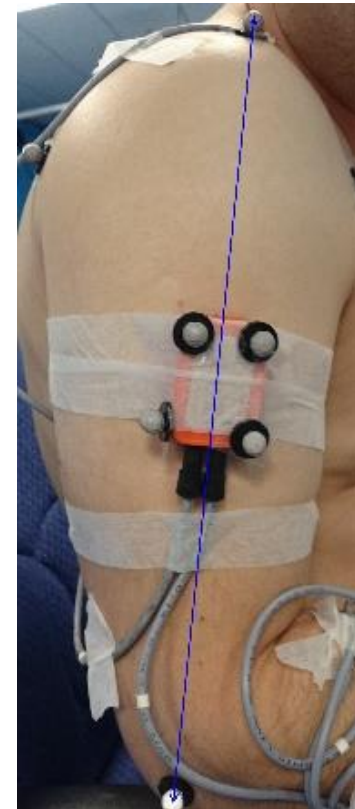
Table 3.7: MIMUs placement – Forearm

	Upper-arm	
Position	Dorso-distally on the right forearm, close to the wrist. This location is a trade-off between the best place to measure forearm movement and interference of with the hand markers.	
Alignment	The x-axis of the MIMU sensor is placed parallel with respect to the virtual line between the middle point of the elbow and the middle point of the wrist.	

Table 3.8: MIMUs placement – Hand

Hand	
Position	Dorsally on the right hand on Metacarpal II and III (MCII & MCIII).
Alignment	The x-axis of the MIMU sensor parallel along the hand.
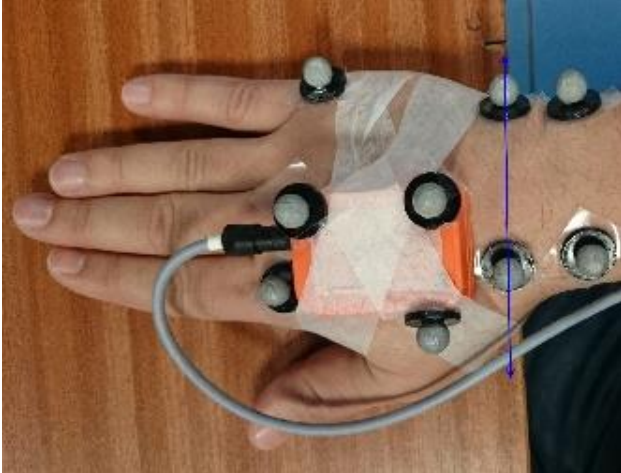
3.4 Human experimental procedures

3.4.1 Participants

Five healthy participants (3 females and 2 male) from the research team took part in this study. The participants had no history of right upper-limb complaints.

To avoid unwanted reflections, participants asked to avoid wearing clothing or jewellery which might introduce reflections. In addition, participants were asked to tie up hair which could occlude markers.

3.4.2 Movements

Two types of trials were recorded: calibration trials and functional task trials, as explained below.

Calibration trials:

These can be divided into two types, static calibration trials and dynamic calibration trials.

The static calibration trials involved the participant holding the body segment in a defined posture while synchronous data from the MIMUs and stereophotogrammetry system were collected. This posture was sitting straight, upper-arm vertical, elbow flexed at 90°, and the hand palm flat on the table. This static position is similar to static trial used by (Bouvier et al., 2015). For each repeat, the participant was requested to hold this posture for five seconds.

The dynamic calibration trials involved the participant performing a specific functional movement while synchronous data from the MIMUs and stereophotogrammetry system were collected. These dynamic calibration movements trials cover the set of calibration movements in Table 2.2 (section 2.3.3, chapter 2) as well as some additional movements. The specific movements for each of the dynamic calibration trials are shown in Table 3.9. It is worth noting that the dynamic movements trials include systematic pauses in the motion,

which are used to derive reference vectors from gravity data (accelerometer data).

Table 3.9: Dynamic calibration movements trials

Thorax (3 DOF)		
1	Sit straight with upper arm vertical, elbow flexed 90º, palm inward – lean forward – back to start pose – lean backward – back to start pose. (de Vries et al., 2010; Luca Ricci et al., 2014).	Thorax flexion-extension
2	Sit straight – laterally lean to right – back to start pose – lean to left – back to start pose.	Thorax lateral-flexion
3	Sit straight, twist to right – back to start pose – twist to left – back to start pose. (Luca Ricci et al., 2014).	Thorax axial rotation
Hand (2 DOF)		
4	Sit straight with upper arm vertical, elbow flexed 90º, palm down on the table – extend hand – back to start pose. (Bouvier et al., 2015; de Vries et al., 2010).	Hand extension
5	Sit straight with upper arm vertical, elbow flexed 90º, palm down on the table – deviate hand radially (to the left) – back to start pose – ulnar deviation (to the right) – back to start pose.	Hand radial-ulnar deviation
Forearm (2 DOF)		
6	Sit straight with upper arm vertical, elbow flexed 90º, palm inward – rotate hand to palm down – back to start pose. (Bonnet et al., 2009; Bouvier et al., 2015; Cutti et al., 2008; de Vries et al., 2010; H. J. Luinge et al., 2007; Luca Ricci et al., 2014; Yang & Ye, 2011).	Neutral-pronation-neutral (0º-90º-0º)

Table 3.9: Dynamic calibration movements trials (Continued…)

	Forearm (2 DOF)	
7	Sit straight with upper arm vertical, elbow flexed 90°, palm inward – flex elbow – back to start pose. (Bonnet et al., 2009; Bouvier et al., 2015; de Vries et al., 2010; Luca Ricci et al., 2014).	Elbow flexion-extension
	Shoulder (3 DOF)	
8	Sit straight with upper arm vertical, elbow flexed 90°, palm inward – rotate shoulder internally – back to start pose – rotate shoulder externally – back to start pose. (Bouvier et al., 2015; de Vries et al., 2010; H. J. Luinge et al., 2007).	Shoulder internal-external rotation
9	Sit straight with upper arm vertical, elbow flexed 90°, palm inward – flex shoulder forward to 90° – back to start pose. (Cutti et al., 2008; de Vries et al., 2010; Luca Ricci et al., 2014; Yang & Ye, 2011).	Shoulder flexion-extension
10	Sit straight with upper arm vertical, elbow flexed 90°, palm inward – abduct shoulder to 90° – back to start pose. (Luca Ricci et al., 2014).	Shoulder abduction-adduction

Functional task trials:

Each dynamic calibration movement trial was followed by the participant performing 4 functional tasks listed in Table 3.10.

Table 3.10: The movements involved in each of the functional task trials

No.	The tasks
1	Reach and sweep to side
2	Reach and sweep back
3	Reach and drink
4	Reach and pour water

All functional tasks were performed with the right limb only. The participants were asked to perform these movements in a natural manner at moderate speed.

To describe each of the functional tasks a top view of the table used is shown in Figures 3.15 to 3.18.

These functional tasks have been chosen because they are both popular and common in clinical physiotherapy rehabilitation and assessments. They involve the larger muscles which move the joints of the upper-limb to produce compound motion. These functional tasks are better suited to FES applications, rather than very complex fine movements (e.g. buttoning a blouse), and they can be tailored to suit the impairment levels of particular stroke patients (Smith et al., 2019).

There were five numbered marks (circles) on the table to guide the participants. All tasks began at Mark-1, which corresponded to the following starting posture: trunk close to the table (about 10 cm between abdomen and table); upper-arm vertical; forearm flexed at 90° with the forearm on the table; and the fingertips on Mark-1. The distance from Mark-1 to Mark-2 was defined as the maximum comfortable reaching movement of each participant. Then the locations of the other marks were as shown in Figures 3.15 to 3.18. Briefly, the functional tasks were as follows:

1. **Reach and sweep to side:** This task consists of two movement phases. Firstly, starting from Mark-1 (the starting position), the participant reaches forward to Mark-2 (shoulder flexion and elbow extension). Secondly, from Mark-2, the hand is swept towards Mark-3 (external rotation of the shoulder is part of the movement).
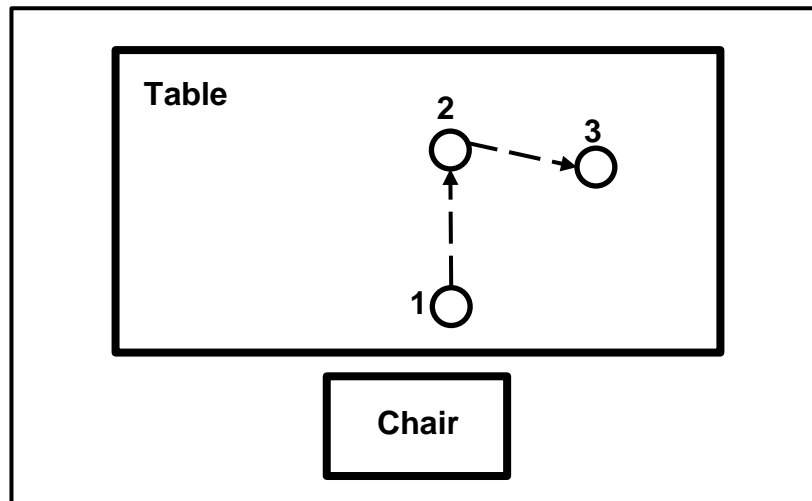
Figure 3.15: Top view of the table – Task 1

2. Reach and sweep back: This task consists of two movement phases. Firstly, starting from Mark-1 (the starting position), the participant reaches forward to Mark-2. Secondly, from Mark-2, the hand is swept towards Mark-4 (internal rotation of the shoulder and elbow flexion are parts of the movement).
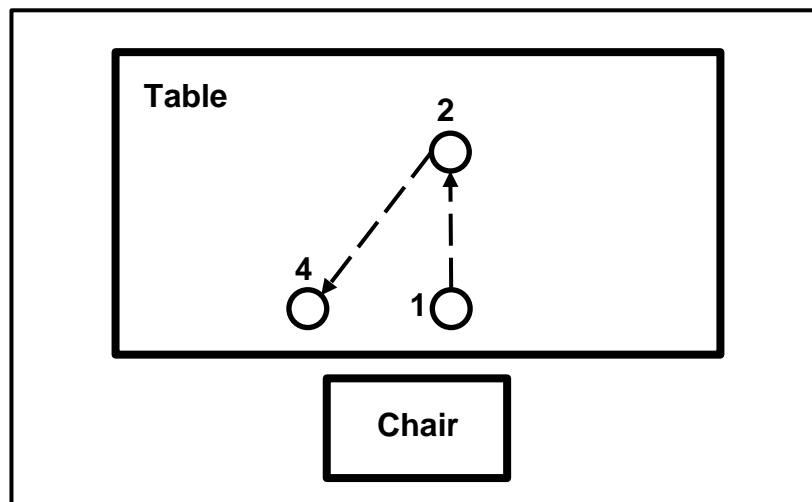
Figure 3.16: Top view of the table – Task 2

3. Reach and drink: Starting from Mark-1, the participant reaches for a bottle placed at Mark-2. Next, the participant lifts the bottle to their mouth for drinking (elbow flexion). Then they put the bottle back in the same place and return to the starting position (elbow extension).
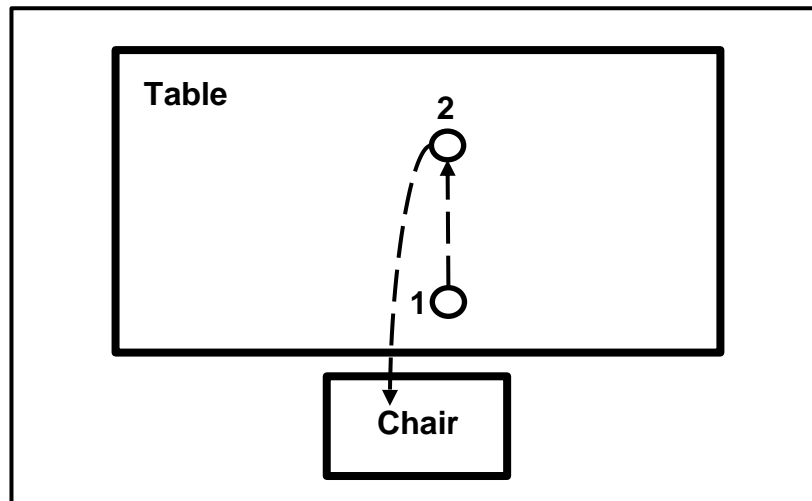
Figure 3.17: Top view of the table – Task 3

4. Reach and pour water: Starting from Mark-1, the participant reaches for a bottle placed at Mark-2. Next, the participant lifts the bottle and pours water into a glass next to the bottle at Mark-5 (forearm pronation) and then the participant puts the bottle back in the same place (forearm supination) and return to the starting position (Mark-1).
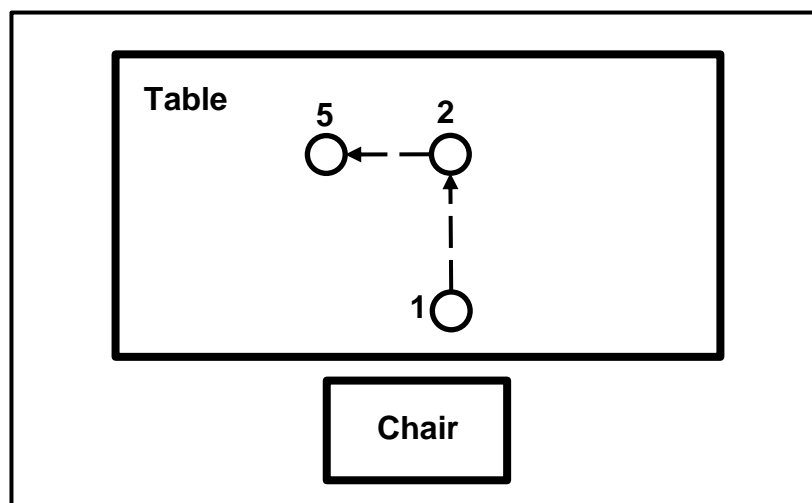
Figure 3.18: Top view of the table – Task 4

Each calibration movement and functional task was repeated four times (four trials (see Figure 3.19)).
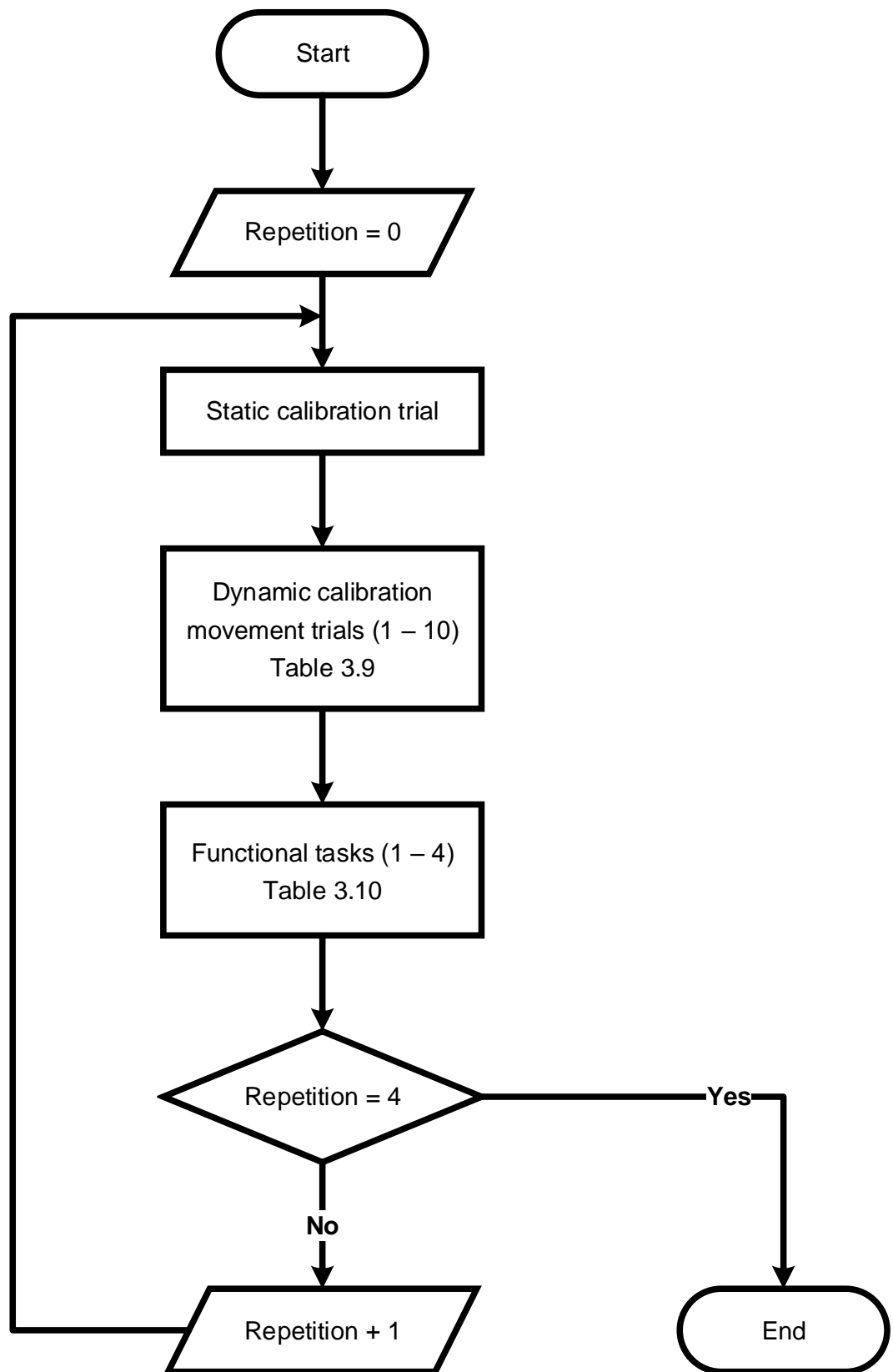
Figure 3.19: Flowchart of experimental protocol for one participant

3.5 Analysis of both stereophotogrammetry and MIMUs data

After data were collected synchronously at 50 Hz with MIMUs and stereophotogrammetry systems, post-processing analysing of data was implemented for both types of data (stereophotogrammetry data and MIMUs data).

3.5.1 Analysis of stereophotogrammetry data

The flow diagram in Figure 3.20 illustrates the data analysis steps:

Step 1. During the data collection, potential marker occlusions or missing markers were checked by examining the marker recordings using Nexus software following each static trial and dynamic movement trial. If any trial had missing or/and occluded marker then the participant was asked to repeat the trial.

Step 2: The raw data was reconstructed to create 3D position data for each of the markers throughout each of the trials.

Step 3: Where there were gaps in the trajectories of any of the trials, first the length of the gaps was identified. In cases where the gaps were less than 10 frames, the missing data were reconstructed using the gap filling function in Nexus.

Step 4: Anatomical markers from the static trial were labelled manually according to the ISB model (Wu et al., 2005) . The technical markers were labelled according to their associated segment. The auto-labelling function was then used to label the markers for each of the dynamic trials. More detail on the labelling convention is given in Chapter 4 (section 4.3.2).
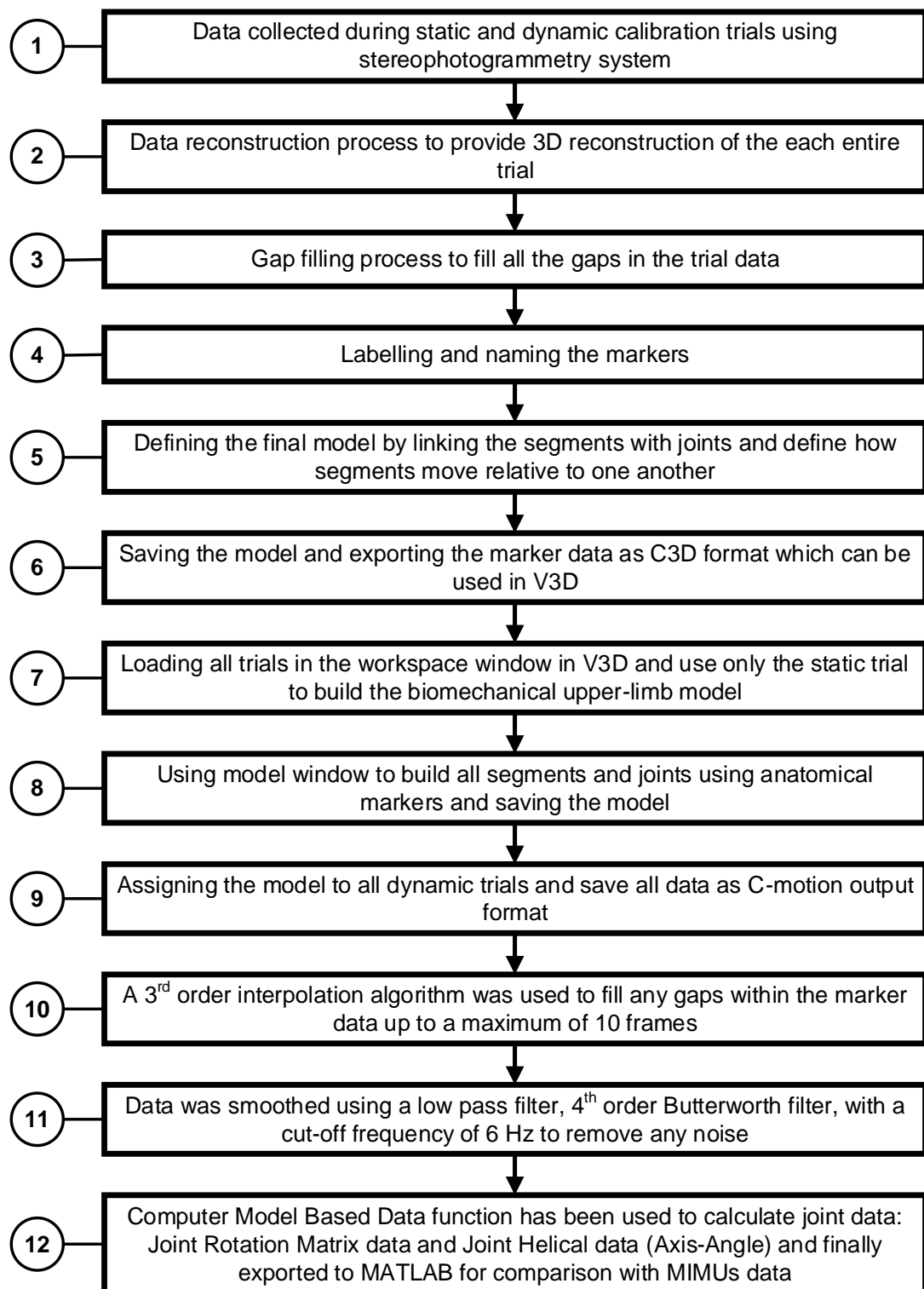
Figure 3.20: Processing of marker data

Step 5: This process involved firstly defining each segment by its associated markers for the static trial. As an example, the forearm segment was defined by

markers RSP, USP, LEH, and MEH (section 3.3.3). Then the joints between each pair of adjoining segments were defined as having 1,2 or 3 degrees of freedom.

Step 6: The defined model, including the set of segments, the markers associated with each segment and the degrees of freedom for each joint was now complete. The set of data from each of the trials was exported from Nexus in C3D format to be ready for use in the data processing stages which used Visual 3D.

Step 7 & 8: Using Visual 3D, the C3D file for the static trial was used build the biomechanical upper-limb kinematic model including the anatomical coordinate frames (see section 3.3.3) for each segment (see Figures 3.21 to 3.24). This involved assigning the sequence of segments in proximal to distal order. The cluster markers were assigned as calibrated tracking markers. The anatomical coordinate frames, based on the ISB model (Wu et al., 2005), (section 3.3.3) were defined as follows

a- Thorax: proximal joint: Mid_T8PX (joint centre); distal: RHAC (lateral) and Mid_C7IJ (joint centre); and the MIMU sensor's markers (T1, T2, T3, and T4) (see Figure 3.21);
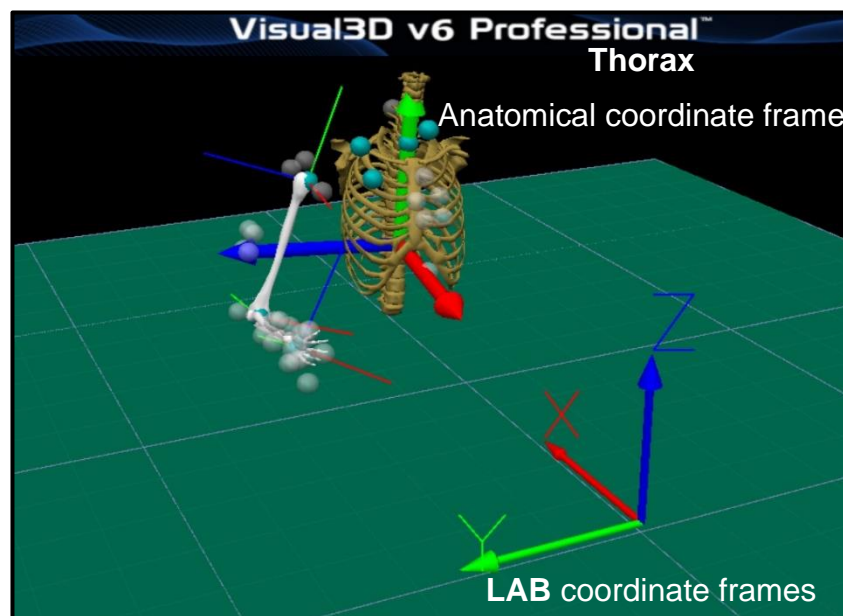
Figure 3.21: Thorax model with anatomical coordinate frames

b- Upper-arm: proximal joint: GHJC (joint centre); distal: LEH (lateral) and MEH (medial); and the MIMU sensor's markers (UA1, UA2, UA3, and UA4) (see Figure 3.22);
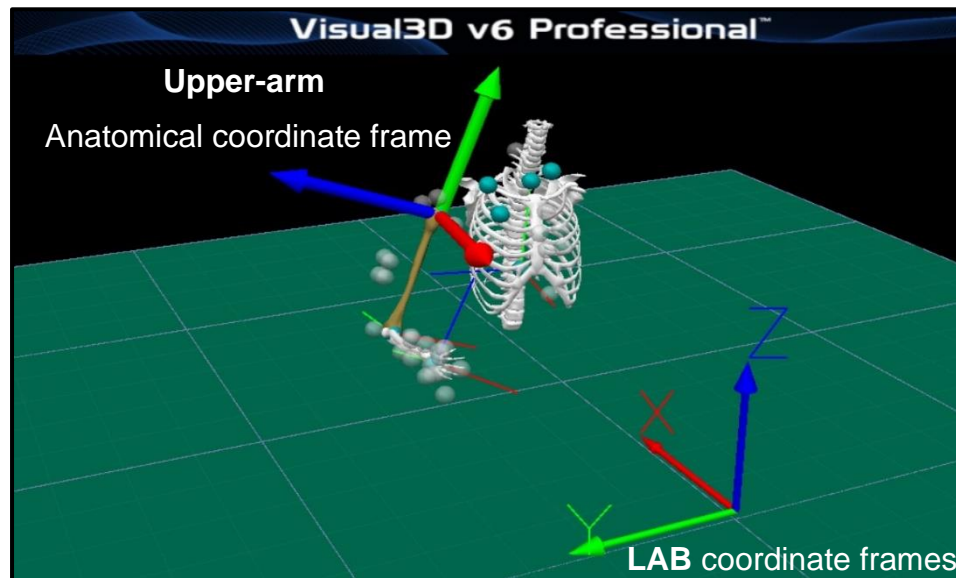
Figure 3.22: Upper-arm model with anatomical coordinate frames

c- Forearm: proximal joint: LEH (lateral) and MEH (medial); distal: Mid_Wrist (joint centre); and the MIMU sensor's markers (FA1, FA2, FA3, and FA4) (see Figure 3.23);
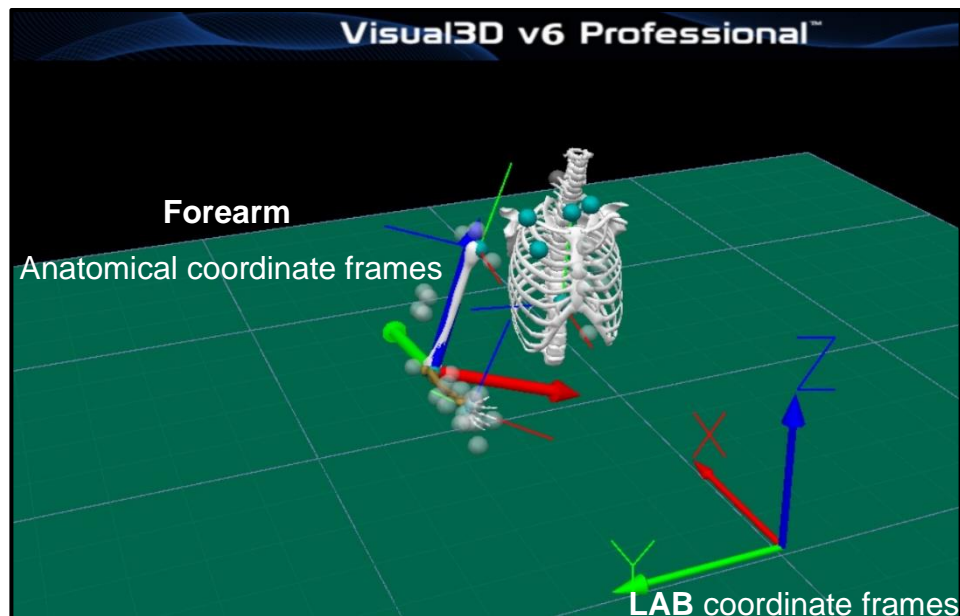
Figure 3.23: Forearm model with anatomical coordinate frames

d- Hand: proximal joint RCP (lateral) and USP (medial); distal: MCII (joint centre); and the MIMU sensor's markers (H1, H2, H3, and H4) (see Figure 3.24);
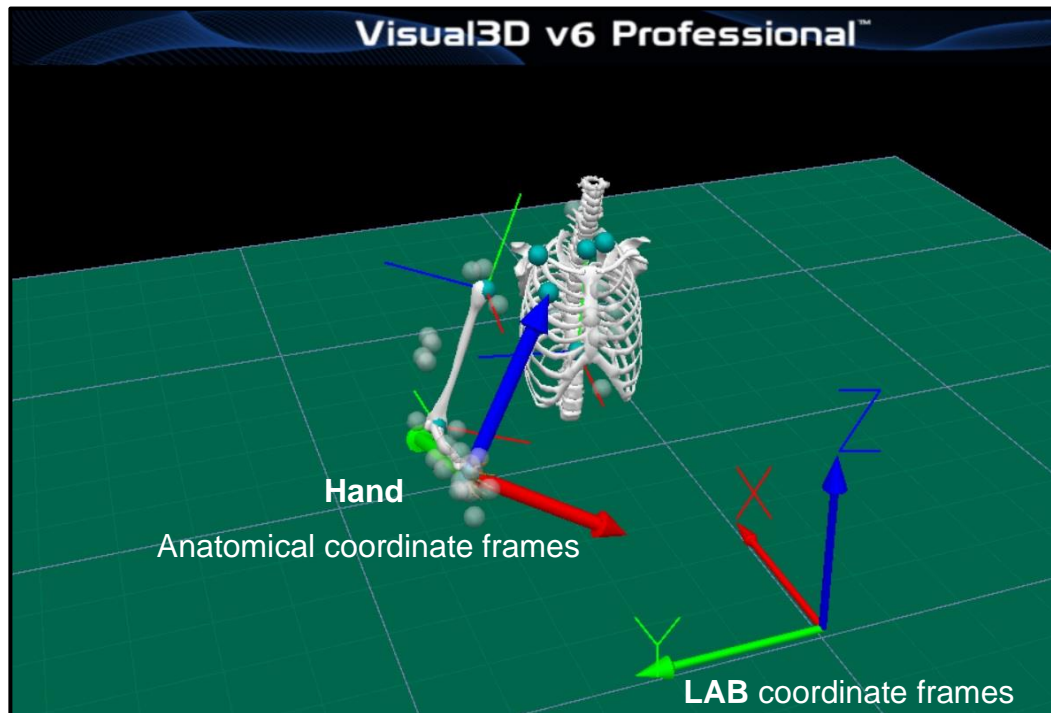
Figure 3.24: Hand model with anatomical coordinate frames

Next the segment coordinate axes were created following ISB recommendation.

Step 9: The upper-limb model was assigned to the all dynamic trials.

Steps 10 and 11: Gap filling was re-done using a 3rd order polynomial interpolation algorithm to fill any remaining gaps up to a maximum of 10 frames. The data were then filtered using a 4th order Butterworth low pass filter with a 6Hz cut-off frequency.

Step 12: The joint angle trajectories for each of the dynamic trials for the 4 joints (thorax, shoulder, elbow, and wrist) in the format of joint rotation matrices were created.

3.5.2 Analysis of MIMUs data

The Figure 3.25 illustrates the steps of recording and analysing MIMUs data.

```
┌─────────────────────────────────────────────────────────────┐
│      MIMU sensor hardware have been checked – wired connection. │
│ (1) │  Additionally, the analogue synchronous channel output to      │
│      stereophotogrammetry system has been checked.             │
└─────────────────────────────────────────────────────────────┘
```

┌─────────┐
│ **1** │ MIMU sensor hardware have been checked – wired connection. Additionally, the analogue synchronous channel output to stereophotogrammetry system has been checked.
└─────────┘

┌─────────┐
│ **2** │ MIMUs sensor setting has been checked. Input options on real-time. Orientation data and calibrated sensor data have been selected on output options as follows: Euler angles: roll, pitch, yaw (XYZ Earth fixed type, also known as Cardan); and Calibrated Sensor Data (3D acceleration, rate of turn, magnetic field).
└─────────┘

┌─────────┐
│ **3** │ MIMUs data has been recorded during static and dynamic calibration trials synchronously at 50 Hz with stereophotogrammetry system and saved as a log files.
└─────────┘

┌─────────┐
│ **4** │ The inertial data (acceleration, angular velocity, and magnetic field data) and orientation data have been moved all to MATLAB directory to be processed.
└─────────┘

Figure 3.25: Processing of MIMUs data

Step 1: The MIMUs were checked before placing them on the participant's body segments. The checking involved making sure the sensors were connected correctly and MT manager software was working properly. Also, the output analogue channel signal from the MIMU system to the stereophotogrammetry system was setup and visually checked. This process was repeated prior to each trial.

Step 2: The MIMU sensor settings in the MT Manager software were set as follows:

- Input options: The COM port used to read real time data was assigned
- Output options: The following outputs were requested
    - Orientation data in format of Euler angles: roll, pitch, yaw (*XYZ* Earth fixed type, also known as Cardan) and
    - Calibrated sensor data (3D acceleration, rate of turn, magnetic field).

Step 3: Data were recorded for each trial (static and dynamic calibration trials, and functional tasks as described in section 3.4.2) synchronously with stereophotogrammetry system at 50 Hz.

Step 4: Finally, MIMUs data was read into MATLAB to be processed and eventually to calculate joint angle trajectories for 4 joints (thorax, shoulder, elbow, and wrist) in the format of joint rotation matrices in order to be ready for comparison with gold standard (stereophotogrammetry). This work is described in the following chapters.

3.6 Discussion and conclusions

This chapter has reported on a protocol used to collect synchronous upper- limb kinematic data from two motion capture systems on five participants. The chapter also reported on the methods to process the data ready for the subsequent work presented in Chapters 4 and 5.

The set of calibration movements used in the study spanned all the previously published methods (Bonnet et al., 2009; Bouvier et al., 2015; Cutti et al., 2008; de Vries et al., 2010; H. J. Luinge et al., 2007; Parel et al., 2012; L. Ricci et al., 2013; Luca Ricci et al., 2014; Vignais et al., 2013; Yang & Ye, 2011). Two new calibration movements were included, to allow for thorax lateral flexion and wrist radial/ulnar deviation to be estimated.

Only two studies have previously tested their methods for estimating joint angle trajectories from MIMU data using functional activities. One task used by (Bouvier

et al., 2015) involved a rotating a circular wheel placed horizontally on a table in front of the participant (Figure 3.26).
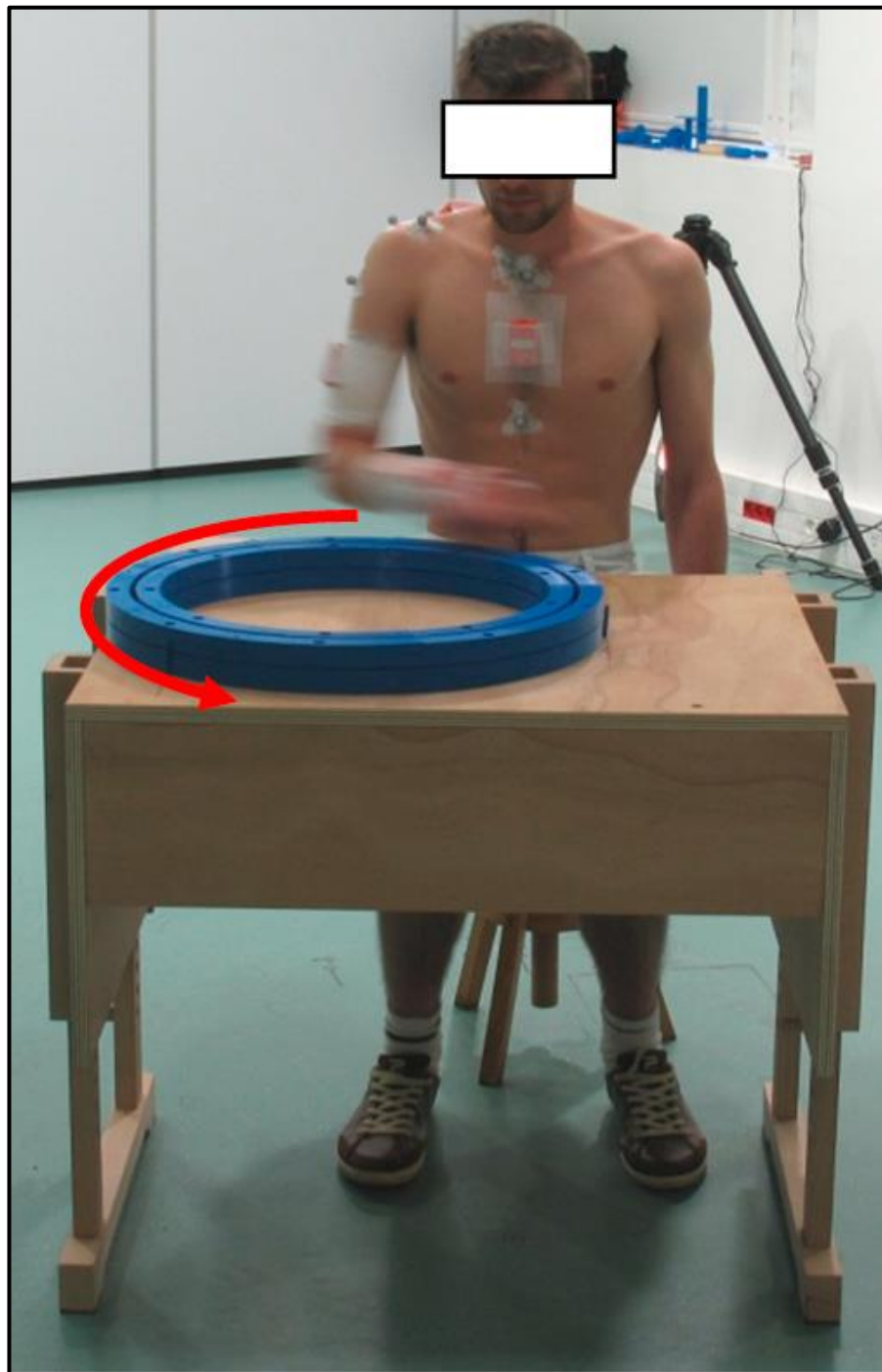
Figure 3.26: Wheel movement task (Bouvier et al., 2015)

Luinge et al. evaluated their approach by asking a single subject to carry out the following tasks: mimicking eating routines: pouring a glass, eating soup, eating spaghetti, eating meat, drinking. The morning routines task consisted of:

splashing water on face and drying it using a towel, applying deodorant, buttoning a blouse, combing hair, brushing teeth.

This study, in common with Luinge's study (H. J. Luinge et al., 2007), used a set of more real-world relevant activities than those used by Bouvier (Bouvier et al., 2015). However, as mentioned earlier, the functional tasks that have been used in this PhD are more suitable for testing FES systems designed for upper-limb rehabilitation. Conversely, the functional tasks used in Luinge's study (H. J. Luinge et al., 2007) are too complex because they were chosen for healthy participants.

Chapter 4 – Theory: Deriving Joint Kinematics from MIMUs Data

4.1 Introduction

In this chapter, the mathematical methods used to process MIMUs data are presented. Firstly, anatomical calibration is discussed, including the basic principles and the alternative approaches to be compared for defining each anatomical coordinate frame. For each alternative, the mathematics for calculating the calibration rotation matrix are presented. Secondly, the derivation of joint rotation matrices and, hence, joint kinematics is described. This combines the sensor outputs (their orientations) and the calibration rotation matrices to obtain the orientations of the anatomical frames. Then the anatomical orientations of segments that are proximal and distal to a joint are used to calculate that joint's rotation matrix, from which other descriptions of the joint kinematics can be derived. Finally, this chapter describes the difficulties encountered with the MIMU orientation estimators.

4.2 Anatomical Calibration

4.2.1 Basic Principles

Anatomical calibration is the establishment of an anatomical coordinate frame for a body segment, expressed in that body segment's MIMU (sensor) coordinate frame, where the latter is defined in Figure 3.3 (section 3.2.1, chapter 3). In other words, for a given body segment, it establishes the relationship between the Anatomical frame (A_k) and the Sensor Inertial frame (SI_k), where the subscript k refers to the body segment, which can be the thorax T, upper-arm U, forearm F or hand H.

The relative orientation of adjacent body segments, and hence the kinematics of shoulder, elbow and wrist joints, can be calculated from orientation data measured by MIMUs (sensors) attached to each body segment of interest.

However, the sensor orientation data cannot be interpreted anatomically unless the orientations of the sensor frames are known with respect to their corresponding segment anatomical frames. Therefore, appropriate calibration must be performed to obtain the relationship between each sensor frame and its corresponding segment anatomical frame (Bouvier et al., 2015; de Vries et al., 2010). The sensor-to-segment calibration procedure consists of the following steps: (1) positioning sensors on the thorax, upper-arm, forearm, and hand; (2) defining an anatomical frame for each body segment; and (3) expressing the orientation of the Anatomical frame (A) with respect to the Sensor Inertial frame (SI) by deriving the corresponding rotation matrix ($^{SI_k}R_{A_k}$).

Two approaches to defining an anatomical frame are possible. Firstly, by careful positioning of the sensor on the body segment, a known geometric relationship between the sensor frame and the anatomical frame may be assumed without the need for any additional calibration procedures. In the simplest case, the segment anatomical axes are equivalent to the sensor axes. In the second approach, the sensor does not have to be positioned as carefully and calibration procedures are followed to construct the segment anatomical frame based on sensor readings. These procedures can include a combination of static calibrations, where the body segment is held in a defined position while readings are taken; and dynamic (functional) calibrations where the participant performs a specific functional movement while readings are taken. In the first case, the participant holds a defined static position for five seconds and the measured gravity vector is used to establish an anatomical reference vector (v_{ref}). In the second case, the participant performs a well-defined uni-axial rotation to determine a functional axis of rotation, which is used as an anatomical reference vector (v_{ref}).

To define a segment anatomical frame, two anatomical reference vectors are used, one primary (v_{ref1}) and one secondary (v_{ref2}). These reference vectors are unit vectors, they are not collinear, and are non-orthogonal. To construct the anatomical frame, v_{ref1} is used as one of the coordinate frame axes. A second axis is obtained from the vector cross product of v_{ref1} and v_{ref2}. Finally, the third

axis is obtained from the vector cross product of the first two axes. This guarantees the orthogonality of the axes of the Anatomical frame (A). For example, the mathematical method may proceed as follows:

$$^{SI_k}X_{A_k} = v_{ref1} \tag{4.1}$$

$$^{SI_k}Y_{A_k} = \frac{v_{ref2} \times {}^{SI_k}X_{A_k}}{\left| v_{ref2} \times {}^{SI_k}X_{A_k} \right|} \tag{4.2}$$

$$^{SI_k}Z_{A_k} = {}^{SI_k}X_{A_k} \times {}^{SI_k}Y_{A_k} \tag{4.3}$$

In this notation the subscript A_k signifies the anatomical coordinate frame to which the axis belongs, and the preceding superscript SI_k signifies that the axis is expressed in the Sensor Inertial coordinate frame. In this case, the secondary reference vector v_{ref2} lies only approximately in the Z-direction, is a temporary Z-axis, and the true Z-axis is obtained by using the cross product to guarantee that the anatomical frame axes are orthogonal (equation 4.3). For this reason, the following notation is also used for the secondary reference vector: $v_{ref2} \equiv {}^{SI}\widetilde{Z}_A$, where the tilde ~ symbol over the axis name indicates that it is a secondary reference vector that is used as a temporary Z-axis. Note that the sequence of the cross products can vary depending on: a) which anatomical axis is defined by v_{ref1} (the **X**-axis in the example above, equation 4.1); and b) which plane is defined by v_{ref1} and v_{ref2} (the **Z-X** plane in the example above, the **Y**-axis being perpendicular to that, equation 4.2).

Then the calibration rotation matrix, equation 4.4, describing the orientation of the Anatomical frame (A_k) with respect to the Sensor Inertial frame (SI_k) is given by (Craig, 2005):

$$^{SI_k}R_{A_k} = \begin{bmatrix} {}^{SI_k}X_{A_k} & {}^{SI_k}Y_{A_k} & {}^{SI_k}Z_{A_k} \end{bmatrix} \tag{4.4}$$

The columns of the calibration rotation matrix are the unit vectors describing the axes of the Anatomical frame (A_k) expressed in the Sensor Inertial frame (SI_k).

While many papers have been published on sensor-to-segment calibration, there has been no comprehensive comparison of the alternative approaches to establish their relative merits (section 2.3.3, chapter 2). For FES supported upper-limb therapy, the need is for simple and fast donning and calibration, whilst achieving acceptable accuracy and repeatability with regards to the calculated joint kinematics. Therefore, the primary objective of the PhD research was to undertake such a comparison and make recommendations for donning and calibration for the purposes of upper-limb FES. To achieve this, MATLAB software has been written to generate all of the alternative combinations of reference vectors (v_{ref1} and v_{ref2}) and the associated calibration rotation matrices.

4.2.2 Alternative Reference Vectors

As mentioned above, there is no study that presents a comprehensive comparison of the alternatives to determine the best approach to calibration. More specifically, no study has compared the many alternative methods for defining the two anatomical reference vectors (v_{ref1} and v_{ref2}). Therefore, in this section, alternative reference vectors are presented for each segment, along with all of the alternative derivations of the corresponding anatomical axes and calibration rotation matrices. The thorax has 8 alternative derivations; the upper-arm has 8 alternatives; the forearm has 10 alternatives; and finally, the hand has 8 alternatives.

For each alternative derivation, the mathematics for calculating the calibration rotation matrix are presented in the series of tables in the following sub-sections. For each segment, the anatomical reference vectors are explained under two headings: static calibrations and dynamic calibrations. In the first case, the participant holds a defined static position for five seconds and the measured gravity vector is used to establish an anatomical reference vector. In the second case, the participant performs a well-defined uni-axial rotation to determine a functional axis of rotation, which is used as an anatomical reference vector.

4.2.2.1 Thorax

Figure 4.1 shows two coordinate frames. The sensor frame is referred to by subscript SI_T (Sensor Inertial Thorax). The anatomical frame is referred to by subscript A_T (Anatomical Thorax).
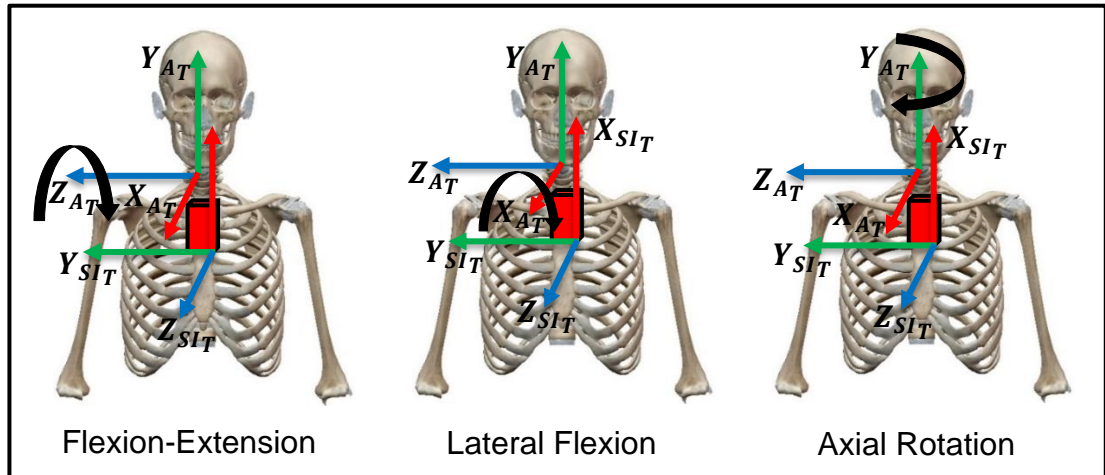
Figure 4.1: Anatomical and Sensor Inertial Frames for the Thorax

To determine the anatomical frame's axes, the sensor data was used as follows:

Static Calibrations:

The static calibration position is sitting with the thorax vertical and straight. The acceleration (gravity) data was used to calculate one anatomical reference vector as follows:

$$^{SI_T}\widetilde{Y}_{AT1} \cong \frac{g}{|g|} \tag{4.5}$$

The subscript A_T and the preceding superscript SI_T signifies that this is an Anatomical Thorax axis and that it is expressed in the thorax's Sensor Inertial frame. The subscript 1 is used because there is more than one alternative Y-axis.

This is not recommended for use as a primary reference vector (v_{ref1}) because this static calibration position is not considered to be particularly repeatable. Rather it should be used only as a secondary reference vector (v_{ref2}), which is indicated by the tilde ~ symbol over the axis name. It lies only approximately in the Y-direction, is a temporary thorax Y-axis, and the true Y-axis is obtained by

using the cross product to guarantee that the anatomical frame axes are orthogonal (see Table 4.1).

Dynamic (Functional) Calibrations:

Three calibration movements were used (see Figure 4.1) to calculate the following anatomical reference vectors:

1) Angular velocity ω (gyro) data captured during lateral flexion of the thorax was used to calculate:

$$^{SI_T}X_{A_T} = \frac{\omega_{LF_r}}{|\omega_{LF_r}|} = -\frac{\omega_{LF_l}}{|\omega_{LF_l}|} \tag{4.6}$$

ω_{LF_r} refers to lateral flexion to the right, while ω_{LF_l} refers to lateral flexion to the left. According to the right-hand rule and to ensure that the anatomical **X**-axis points forwards, if data for lateral flexion to the right is used, then the sign should remain unchanged. Conversely, if data for lateral flexion to the left is used, the vector should be multiplied by -1.

2) Angular velocity data captured during axial rotation of the thorax was used to calculate:

$$^{SI_T}Y_{A_{T2}} = -\frac{\omega_{AR_r}}{|\omega_{AR_r}|} = \frac{\omega_{AR_l}}{|\omega_{AR_l}|} \tag{4.7}$$

ω_{AR_r} refers to axial rotation to the right, while ω_{AR_l} refers to axial rotation to left, while ω_{AR_l} refers to axial rotation to the left. The subscript 2 is used because there is more than one alternative **Y**-axis (see equation 4.5 above).

3) Angular velocity data captured during forward flexion/backward extension of the thorax was used to calculate:

$$^{SI_T}Z_{A_T} = -\frac{\omega_{Flex}}{|\omega_{Flex}|} = \frac{\omega_{Ext}}{|\omega_{Ext}|} \tag{4.8}$$

ω_{Flex} refers to flexion, while ω_{Ext} refers to extension.

Given the four anatomical reference vectors above (equations 4.5 to 4.8) and noting that $^{SI_T}\widetilde{Y}_{A_{T1}}$ is only to be used as v_{ref2}, there are 8 ways these can be combined as shown in Table 4.1 together with the corresponding derivations of the anatomical axes and the calibration rotation matrix. The derivations are based on the general approach described by equations 4.1 to 4.4.

Table 4.1: Eight alternative derivations of the calibration rotation matrix for the thorax

	v_{ref1}	v_{ref2}	Second and third axes	Calibration rotation matrix
1	$^{SI_T}X_{A_T}$	$^{SI_T}\widetilde{Y}_{A_{T1}}$	$^{SI_T}Z_{A_T} = \dfrac{^{SI_T}X_{A_T} \times v_{ref2}}{\left|^{SI_T}X_{A_T} \times v_{ref2}\right|}$, $^{SI_T}Y_{A_T} = {}^{SI_T}Z_{A_T} \times {}^{SI_T}X_{A_T}$	$^{SI_T}R_{A_{T1}} = \begin{bmatrix} ^{SI_T}X_{A_T} & ^{SI_T}Y_{A_T} & ^{SI_T}Z_{A_T} \end{bmatrix}$
2	$^{SI_T}X_{A_T}$	$^{SI_T}\widetilde{Y}_{A_{T2}}$	$^{SI_T}Z_{A_T} = \dfrac{^{SI_T}X_{A_T} \times v_{ref2}}{\left|^{SI_T}X_{A_T} \times v_{ref2}\right|}$, $^{SI_T}Y_{A_T} = {}^{SI_T}Z_{A_T} \times {}^{SI_T}X_{A_T}$	$^{SI_T}R_{A_{T2}} = \begin{bmatrix} ^{SI_T}X_{A_T} & ^{SI_T}Y_{A_T} & ^{SI_T}Z_{A_T} \end{bmatrix}$
3	$^{SI_T}X_{A_T}$	$^{SI_T}\widetilde{Z}_{A_T}$	$^{SI_T}Y_{A_T} = \dfrac{v_{ref2} \times {}^{SI_T}X_{A_T}}{\left|v_{ref2} \times {}^{SI_T}X_{A_T}\right|}$, $^{SI_T}Z_{A_T} = {}^{SI_T}X_{A_T} \times {}^{SI_T}Y_{A_T}$	$^{SI_T}R_{A_{T3}} = \begin{bmatrix} ^{SI_T}X_{A_T} & ^{SI_T}Y_{A_T} & ^{SI_T}Z_{A_T} \end{bmatrix}$
4	$^{SI_T}Y_{A_{T2}}$	$^{SI_T}\widetilde{X}_{A_T}$	$^{SI_T}Z_{A_T} = \dfrac{v_{ref2} \times {}^{SI_T}Y_{A_{T2}}}{\left|v_{ref2} \times {}^{SI_T}Y_{A_{T2}}\right|}$, $^{SI_T}X_{A_T} = {}^{SI_T}Y_{A_{T2}} \times {}^{SI_T}Z_{A_T}$	$^{SI_T}R_{A_{T4}} = \begin{bmatrix} ^{SI_T}X_{A_T} & ^{SI_T}Y_{A_{T2}} & ^{SI_T}Z_{A_T} \end{bmatrix}$
5	$^{SI_T}Y_{A_{T2}}$	$^{SI_T}\widetilde{Z}_{A_T}$	$^{SI_T}X_{A_T} = \dfrac{^{SI_T}Y_{A_{T2}} \times v_{ref2}}{\left|^{SI_T}Y_{A_{T2}} \times v_{ref2}\right|}$, $^{SI_T}Z_{A_T} = {}^{SI_T}X_{A_T} \times {}^{SI_T}Y_{A_{T2}}$	$^{SI_T}R_{A_{T5}} = \begin{bmatrix} ^{SI_T}X_{A_T} & ^{SI_T}Y_{A_{T2}} & ^{SI_T}Z_{A_T} \end{bmatrix}$
6	$^{SI_T}Z_{A_T}$	$^{SI_T}\widetilde{X}_{A_T}$	$^{SI_T}Y_{A_T} = \dfrac{^{SI_T}Z_{A_T} \times v_{ref2}}{\left|^{SI_T}Z_{A_T} \times v_{ref2}\right|}$, $^{SI_T}X_{A_T} = {}^{SI_T}Y_{A_T} \times {}^{SI_T}Z_{A_T}$	$^{SI_T}R_{A_{T6}} = \begin{bmatrix} ^{SI_T}X_{A_T} & ^{SI_T}Y_{A_T} & ^{SI_T}Z_{A_T} \end{bmatrix}$
7	$^{SI_T}Z_{A_T}$	$^{SI_T}\widetilde{Y}_{A_{T1}}$	$^{SI_T}X_{A_T} = \dfrac{v_{ref2} \times {}^{SI_T}Z_{A_T}}{\left|v_{ref2} \times {}^{SI_T}Z_{A_T}\right|}$, $^{SI_T}Y_{A_T} = {}^{SI_T}Z_{A_T} \times {}^{SI_T}X_{A_T}$	$^{SI_T}R_{A_{T7}} = \begin{bmatrix} ^{SI_T}X_{A_T} & ^{SI_T}Y_{A_T} & ^{SI_T}Z_{A_T} \end{bmatrix}$
8	$^{SI_T}Z_{A_T}$	$^{SI_T}\widetilde{Y}_{A_{T2}}$	$^{SI_T}X_{A_T} = \dfrac{v_{ref2} \times {}^{SI_T}Z_{A_T}}{\left|v_{ref2} \times {}^{SI_T}Z_{A_T}\right|}$, $^{SI_T}Y_{A_T} = {}^{SI_T}Z_{A_T} \times {}^{SI_T}X_{A_T}$	$^{SI_T}R_{A_{T8}} = \begin{bmatrix} ^{SI_T}X_{A_T} & ^{SI_T}Y_{A_T} & ^{SI_T}Z_{A_T} \end{bmatrix}$

4.2.2.2 Upper-arm

Figure 4.2 shows two coordinate frames. The sensor frame is referred to by subscript SI_U (Sensor Inertial Upper-arm). The anatomical frame is referred to by subscript A_U (Anatomical Upper-arm).

Figure 4.2: Anatomical and Sensor Inertial Frames for the Upper-arm

To determine the anatomical frame's axes, the sensor data was used as follows:

Static Calibrations:

The static calibration position is sitting with the thorax vertical and straight, and the upper-arm vertical and aligned with the body. The acceleration (gravity) data was used to calculate one anatomical reference vector as follows:

$$^{SI_U}\widetilde{Y}_{AU1} \cong \frac{g}{|g|} \tag{4.9}$$

The subscript A_U and the preceding superscript SI_U signifies that this is an Anatomical Upper-arm axis and that it is expressed in the upper-arm's Sensor

Inertial frame. The subscript 1 is used because there is more than one alternative Y-axis.

This is not recommended for use as a primary reference vector (v_{ref1}) because this static calibration position is not considered to be particularly repeatable. Rather it should be used only as a secondary reference vector (v_{ref2}), which is indicated by the tilde ~ symbol over the axis name. It lies only approximately in the Y-direction, is a temporary upper-arm Y-axis, and the true Y-axis is obtained by using the cross product to guarantee that the anatomical frame axes are orthogonal (see Table 4.2).

Dynamic (Functional) Calibrations:

Three calibration movements were used (see Figure 4.2) to calculate the following anatomical reference vectors:

1) Angular velocity ω (gyro) data captured during shoulder abduction-adduction was used to calculate:

$$^{SI_U}X_{A_U} = \frac{\omega_{Add}}{|\omega_{Add}|} = -\frac{\omega_{Abd}}{|\omega_{Abd}|} \tag{4.10}$$

ω_{Add} refers to adduction, while ω_{Abd} refers to abduction. According to the right-hand rule and to ensure that the anatomical X-axis points forwards, if data for adduction is used, then the sign should remain unchanged. Conversely, if data for abduction is used, the vector should be multiplied by -1.

2) Angular velocity data captured during shoulder internal-external rotation was used to calculate:

$$^{SI_U}Y_{A_{U2}} = \frac{\omega_{Int_r}}{|\omega_{Int_r}|} = -\frac{\omega_{Ext_r}}{|\omega_{Ext_r}|} \tag{4.11}$$

ω_{Int_r} refers to internal rotation, while ω_{Ext_r} refers to external rotation. The subscript 2 is used because there is more than one alternative Y-axis (see equation 4.9 above).

3) Angular velocity data captured during shoulder flexion-extension was used to calculate:

$$^{SI_U}Z_{A_U} = \frac{\omega_{Flex}}{|\omega_{Flex}|} = -\frac{\omega_{Ext}}{|\omega_{Ext}|} \tag{4.12}$$

$\boldsymbol{\omega_{Flex}}$ refers to flexion, while $\boldsymbol{\omega_{Ext}}$ refers to extension.

Given the four anatomical reference vectors above (equations 4.9 to 4.12) and noting that ${}^{SI_U}\widetilde{Y}_{AU1}$ is only to be used as v_{ref2}, there are 8 ways these can be combined as shown in Table 4.2 together with the corresponding derivations of the anatomical axes and the calibration rotation matrix. The derivations are based on the general approach described by equations 4.1 to 4.4.

Table 4.2: Eight alternative derivations of the calibration rotation matrix for the upper-arm

	v_{ref1}	v_{ref2}	Second and third axes	Calibration rotation matrix
1	$^{SI_U}X_{A_U}$	$^{SI_U}\widetilde{Y}_{A_{U1}}$	$^{SI_U}Z_{A_U} = \dfrac{^{SI_U}X_{A_U} \times v_{ref2}}{\left|^{SI_U}X_{A_U} \times v_{ref2}\right|}, \ ^{SI_U}Y_{A_U} = {^{SI_U}Z_{A_U}} \times {^{SI_U}X_{A_U}}$	$^{SI_U}R_{A_{U1}} = \begin{bmatrix} ^{SI_U}X_{A_U} & ^{SI_U}Y_{A_U} & ^{SI_U}Z_{A_U} \end{bmatrix}$
2	$^{SI_U}X_{A_U}$	$^{SI_U}\widetilde{Y}_{A_{U2}}$	$^{SI_U}Z_{A_U} = \dfrac{^{SI_U}X_{A_U} \times v_{ref2}}{\left|^{SI_U}X_{A_U} \times v_{ref2}\right|}, \ ^{SI_U}Y_{A_U} = {^{SI_U}Z_{A_U}} \times {^{SI_U}X_{A_U}}$	$^{SI_U}R_{A_{U2}} = \begin{bmatrix} ^{SI_U}X_{A_U} & ^{SI_U}Y_{A_U} & ^{SI_U}Z_{A_U} \end{bmatrix}$
3	$^{SI_U}X_{A_U}$	$^{SI_U}\widetilde{Z}_{A_U}$	$^{SI_U}Y_{A_U} = \dfrac{v_{ref2} \times {^{SI_U}X_{A_U}}}{\left|v_{ref2} \times {^{SI_U}X_{A_U}}\right|}, \ ^{SI_U}Z_{A_U} = {^{SI_U}X_{A_U}} \times {^{SI_U}Y_{A_U}}$	$^{SI_U}R_{A_{U3}} = \begin{bmatrix} ^{SI_U}X_{A_U} & ^{SI_U}Y_{A_U} & ^{SI_U}Z_{A_U} \end{bmatrix}$
4	$^{SI_U}Y_{A_{U2}}$	$^{SI_U}\widetilde{X}_{A_U}$	$^{SI_U}Z_{A_U} = \dfrac{v_{ref2} \times {^{SI_U}Y_{A_{U2}}}}{\left|v_{ref2} \times {^{SI_U}Y_{A_{U2}}}\right|}, \ ^{SI_U}X_{A_U} = {^{SI_U}Y_{A_{U2}}} \times {^{SI_U}Z_{A_U}}$	$^{SI_U}R_{A_{U4}} = \begin{bmatrix} ^{SI_U}X_{A_U} & ^{SI_U}Y_{A_{U2}} & ^{SI_U}Z_{A_U} \end{bmatrix}$
5	$^{SI_U}Y_{A_{U2}}$	$^{SI_U}\widetilde{Z}_{A_U}$	$^{SI_U}X_{A_U} = \dfrac{^{SI_U}Y_{U2} \times v_{ref2}}{\left|^{SI_U}Y_{U2} \times v_{ref2}\right|}, \ ^{SI_U}Z_{A_U} = {^{SI_U}X_{A_U}} \times {^{SI_U}Y_{A_{U2}}}$	$^{SI_U}R_{A_{U5}} = \begin{bmatrix} ^{SI_U}X_{A_U} & ^{SI_U}Y_{A_{U2}} & ^{SI_U}Z_{A_U} \end{bmatrix}$
6	$^{SI_U}Z_{A_U}$	$^{SI_U}\widetilde{X}_{A_U}$	$^{SI_U}Y_{A_U} = \dfrac{^{SI_U}Z_{A_U} \times v_{ref2}}{\left|^{SI_U}Z_{A_U} \times v_{ref2}\right|}, \ ^{SI_U}X_{A_U} = {^{SI_U}Y_{A_U}} \times {^{SI_U}Z_{A_U}}$	$^{SI_U}R_{A_{U6}} = \begin{bmatrix} ^{SI_U}X_{A_U} & ^{SI_U}Y_{A_U} & ^{SI_U}Z_{A_U} \end{bmatrix}$
7	$^{SI_U}Z_{A_U}$	$^{SI_U}\widetilde{Y}_{A_{U1}}$	$^{SI_U}X_{A_U} = \dfrac{v_{ref2} \times {^{SI_U}Z_{A_U}}}{\left|v_{ref2} \times {^{SI_U}Z_{A_U}}\right|}, \ ^{SI_U}Y_{A_U} = {^{SI_U}Z_{A_U}} \times {^{SI_U}X_{A_U}}$	$^{SI_U}R_{A_{U7}} = \begin{bmatrix} ^{SI_U}X_{A_U} & ^{SI_U}Y_{A_U} & ^{SI_U}Z_{A_U} \end{bmatrix}$
8	$^{SI_U}Z_{A_U}$	$^{SI_U}\widetilde{Y}_{A_{U2}}$	$^{SI_U}X_{A_U} = \dfrac{v_{ref2} \times {^{SI_U}Z_{A_U}}}{\left|v_{ref2} \times {^{SI_U}Z_{A_U}}\right|}, \ ^{SI_U}Y_{A_U} = {^{SI_U}Z_{A_U}} \times {^{SI_U}X_{A_U}}$	$^{SI_U}R_{A_{U8}} = \begin{bmatrix} ^{SI_U}X_{A_U} & ^{SI_U}Y_{A_U} & ^{SI_U}Z_{A_U} \end{bmatrix}$

4.2.2.3 Forearm

Figure 4.3 shows two coordinate frames. The sensor frame is referred to by subscript SI_F (Sensor Inertial Forearm). The anatomical frame is referred to by subscript A_F (Anatomical Forearm).
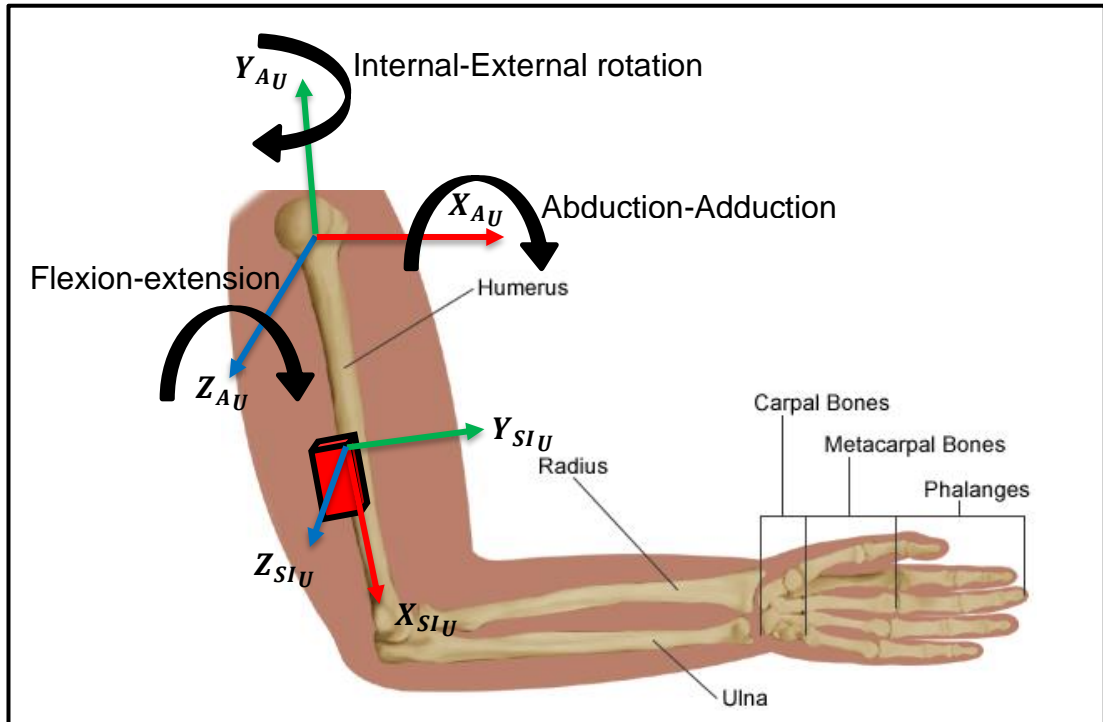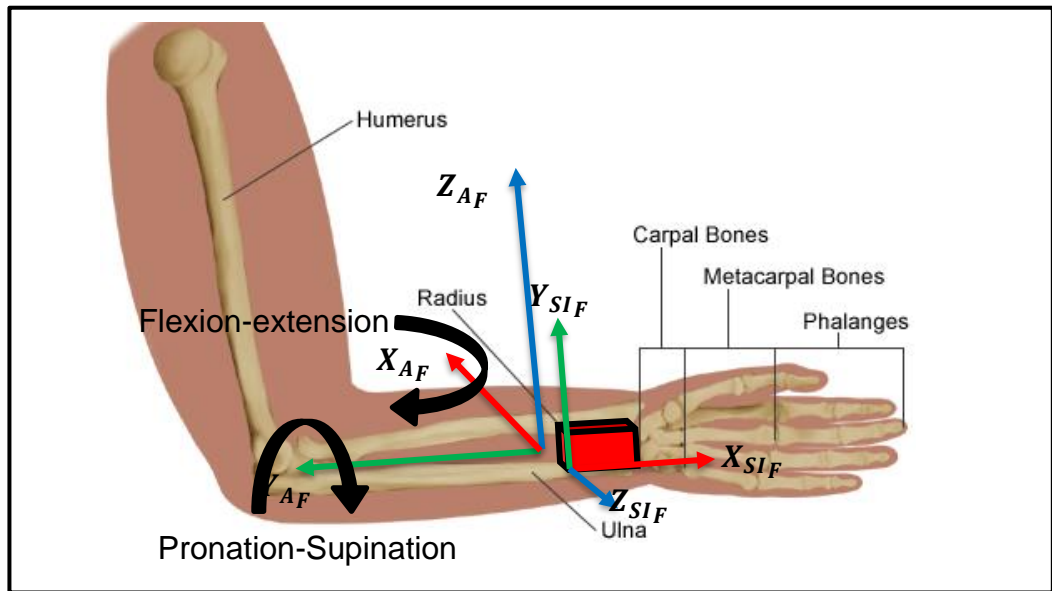

Figure 4.3: Anatomical and Sensor Inertial Frames for the Forearm

To determine the anatomical frame's axes, the sensor data was used as follows:

Static Calibrations:

1) The first static calibration position is sitting with the thorax vertical and straight, the upper-arm vertical and aligned with the body, and the forearm fully pronated with the hand palm down on the table. The acceleration (gravity) data was used to calculate one anatomical reference vector as follows:

$$^{SI_F}\widetilde{X}_{A_{F1}} \cong -\frac{g}{|g|} \tag{4.13}$$

The subscript A_F and the preceding superscript SI_F signifies that this is an Anatomical Forearm axis and that it is expressed in the forearm's Sensor Inertial frame. The subscript 1 is used because there is more than one alternative X-axis.

This is not recommended for use as a primary reference vector (v_{ref1}) because this static calibration position is not considered to be particularly repeatable. Rather it should be used only as a secondary reference vector (v_{ref2}), which is indicated by the tilde ~ symbol over the axis name. It lies only approximately in the X-direction, is a temporary forearm X-axis, and the true X-axis is obtained by using the cross product to guarantee that the anatomical frame axes are orthogonal (see Table 4.3).

2) A second gravity-based anatomical reference vector has been calculated, from the sensor data captured at the beginning of the pronation-supination movement, when the forearm is in the neutral position with the palm vertical as shown in Figure 4.3:

$$^{SI_F}\widetilde{Z}_{A_{F1}} \cong \frac{g}{|g|} \tag{4.14}$$

Again, the subscript 1 is used because there is more than one alternative Z-axis and the tilde ~ symbol is used because this should be used only as a secondary reference vector (v_{ref2}).

Dynamic (Functional) Calibrations:

Two calibration movements were used (see Figure 4.3) to calculate the following anatomical reference vectors:

1) Angular velocity $\boldsymbol{\omega}$ (gyro) data captured during elbow flexion-extension was used to calculate:

$$^{SI_F}X_{A_{F2}} = \frac{\omega_{Ext}}{|\omega_{Ext}|} = -\frac{\omega_{Flex}}{|\omega_{Flex}|} \tag{4.15}$$

ω_{Ext} refers to extension, while ω_{Flex} refers to flexion. The subscript 2 is used because there is more than one alternative X-axis (see equation 4.13 above). According to the right-hand rule and to ensure that the anatomical X-axis points forwards, if data for elbow extension is used, then the sign should remain unchanged. Conversely, if data for elbow flexion is used, the vector should be multiplied by -1.

2) Angular velocity data captured during elbow pronation-supination was used to calculate:

$$^{SI_F}Y_{A_F} = -\frac{\omega_{Sup}}{|\omega_{Sup}|} = \frac{\omega_{Pron}}{|\omega_{Pron}|} \tag{4.16}$$

ω_{Sup} refers to supination, while ω_{Pron} refers to pronation.

3) Angular velocity data captured during shoulder internal-external rotation was used to calculate:

$$^{SI_U}Z_{A_{F2}} = \frac{\omega_{Int_r}}{|\omega_{Int_r}|} = -\frac{\omega_{Ext_r}}{|\omega_{Ext_r}|} \tag{4.17}$$

ω_{Int_r} refers to internal rotation, while ω_{Ext_r} refers to external rotation. The subscript 2 is used because there is more than one alternative **Z**-axis (see equation 4.14 above).

Given the five anatomical reference vectors above (equations 4.13 to 4.17) and noting that $^{SI_F}\widetilde{X}_{A_{F1}}$ and $^{SI_F}\widetilde{Z}_{A_{F1}}$ are only to be used as v_{ref2}, there are 10 ways these can be combined as shown in Table 4.3 together with the corresponding derivations of the anatomical axes and the calibration rotation matrix. The derivations are based on the general approach described by equations 4.1 to 4.4

Table 4.3: Ten alternative derivations of the calibration rotation matrix for the forearm

	v_{ref1}	v_{ref2}	Second and third axes	Calibration rotation matrix
1	$^{SI_F}X_{A_{F2}}$	$^{SI_F}\widetilde{Y}_{A_F}$	$^{SI_F}Z_{A_F} = \dfrac{^{SI_F}X_{A_{F2}} \times v_{ref2}}{\left|^{SI_F}X_{A_{F2}} \times v_{ref2}\right|}$, $^{SI_F}Y_{A_F} = {}^{SI_F}Z_{A_F} \times {}^{SI_F}X_{A_{F2}}$	$^{SI_F}R_{A_{F1}} = \begin{bmatrix} ^{SI_F}X_{A_{F2}} & ^{SI_F}Y_{A_F} & ^{SI_F}Z_{A_F} \end{bmatrix}$
2	$^{SI_F}X_{A_{F2}}$	$^{SI_F}\widetilde{Z}_{A_{F1}}$	$^{SI_F}Y_{A_F} = \dfrac{v_{ref2} \times {}^{SI_F}X_{A_{F2}}}{\left|v_{ref2} \times {}^{SI_F}X_{A_{F2}}\right|}$, $^{SI_F}Z_{A_F} = {}^{SI_F}X_{A_{F2}} \times {}^{SI_F}Y_{A_F}$	$^{SI_F}R_{A_{F2}} = \begin{bmatrix} ^{SI_F}X_{A_{F2}} & ^{SI_F}Y_{A_F} & ^{SI_F}Z_{A_F} \end{bmatrix}$
3	$^{SI_F}X_{A_{F2}}$	$^{SI_U}\widetilde{Z}_{A_{F2}}$	$^{SI_F}Y_{A_F} = \dfrac{v_{ref2} \times {}^{SI_F}X_{A_{F2}}}{\left|v_{ref2} \times {}^{SI_F}X_{A_{F2}}\right|}$, $^{SI_F}Z_{A_F} = {}^{SI_F}X_{A_{F2}} \times {}^{SI_F}Y_{A_F}$	$^{SI_F}R_{A_{F3}} = \begin{bmatrix} ^{SI_F}X_{A_{F2}} & ^{SI_F}Y_{A_F} & ^{SI_F}Z_{A_F} \end{bmatrix}$
4	$^{SI_F}Y_{A_F}$	$^{SI_F}\widetilde{X}_{A_{F1}}$	$^{SI_F}Z_{A_F} = \dfrac{v_{ref2} \times {}^{SI_F}Y_{A_F}}{\left|v_{ref2} \times {}^{SI_F}Y_{A_F}\right|}$, $^{SI_F}X_{A_F} = {}^{SI_F}Y_{A_F} \times {}^{SI_F}Z_{A_F}$	$^{SI_F}R_{A_{F4}} = \begin{bmatrix} ^{SI_F}X_{A_F} & ^{SI_F}Y_{A_F} & ^{SI_F}Z_{A_F} \end{bmatrix}$
5	$^{SI_F}Y_{A_F}$	$^{SI_F}\widetilde{X}_{A_{F2}}$	$^{SI_F}Z_{A_F} = \dfrac{v_{ref2} \times {}^{SI_F}Y_{A_F}}{\left|v_{ref2} \times {}^{SI_F}Y_{A_F}\right|}$, $^{SI_F}X_F = {}^{SI_F}Y_{A_F} \times {}^{SI_F}Z_{A_F}$	$^{SI_F}R_{A_{F5}} = \begin{bmatrix} ^{SI_F}X_{A_F} & ^{SI_F}Y_{A_F} & ^{SI_F}Z_{A_F} \end{bmatrix}$
6	$^{SI_F}Y_{A_F}$	$^{SI_F}\widetilde{Z}_{A_{F1}}$	$^{SI_F}X_{A_F} = \dfrac{^{SI_F}Y_{A_F} \times v_{ref2}}{\left|^{SI_F}Y_{A_F} \times v_{ref2}\right|}$, $^{SI_F}Z_{A_F} = {}^{SI_F}X_{A_F} \times {}^{SI_F}Y_{A_F}$	$^{SI_F}R_{A_{F6}} = \begin{bmatrix} ^{SI_F}X_{A_F} & ^{SI_F}Y_{A_F} & ^{SI_F}Z_{A_F} \end{bmatrix}$
7	$^{SI_F}Y_{A_F}$	$^{SI_U}\widetilde{Z}_{A_{F2}}$	$^{SI_F}X_{A_F} = \dfrac{^{SI_F}Y_{A_F} \times v_{ref2}}{\left|^{SI_F}Y_{A_F} \times v_{ref2}\right|}$, $^{SI_F}Z_{A_F} = {}^{SI_F}X_{A_F} \times {}^{SI_F}Y_{A_F}$	$^{SI_F}R_{A_{F7}} = \begin{bmatrix} ^{SI_F}X_{A_F} & ^{SI_F}Y_{A_F} & ^{SI_F}Z_{A_F} \end{bmatrix}$
8	$^{SI_U}Z_{A_{F2}}$	$^{SI_F}\widetilde{X}_{A_{F1}}$	$^{SI_F}Y_{A_F} = \dfrac{^{SI_U}Z_{A_{F2}} \times v_{ref2}}{\left|^{SI_U}Z_{A_{F2}} \times v_{ref2}\right|}$, $^{SI_F}X_{A_F} = {}^{SI_F}Y_{A_F} \times {}^{SI_U}Z_{A_{F2}}$	$^{SI_F}R_{A_{F8}} = \begin{bmatrix} ^{SI_F}X_{A_F} & ^{SI_F}Y_{A_F} & ^{SI_U}Z_{A_{F2}} \end{bmatrix}$

Table 4.3: Ten alternative derivations of the calibration rotation matrix for the forearm (Continued…)

	v_{ref1}	v_{ref2}	Second and third axes	Calibration rotation matrix
9	${}^{SI_U}Z_{A_{F2}}$	${}^{SI_F}\widetilde{X}_{A_{F2}}$	${}^{SI_F}Y_{A_F} = \dfrac{{}^{SI_U}Z_{A_{F2}} \times v_{ref2}}{\left\|{}^{SI_U}Z_{A_{F2}} \times v_{ref2}\right\|},\ {}^{SI_F}X_{A_F} = {}^{SI_F}Y_{A_F} \times {}^{SI_U}Z_{A_{F2}}$	${}^{SI_F}R_{A_{F9}} = \begin{bmatrix} {}^{SI_F}X_{A_F} & {}^{SI_F}Y_{A_F} & {}^{SI_U}Z_{A_{F2}} \end{bmatrix}$
10	${}^{SI_U}Z_{A_{F2}}$	${}^{SI_F}\widetilde{Y}_{A_F}$	${}^{SI_F}X_{A_F} = \dfrac{v_{ref2} \times {}^{SI_U}Z_{A_{F2}}}{\left\|v_{ref2} \times {}^{SI_U}Z_{A_{F2}}\right\|},\ {}^{SI_F}Y_{A_F} = {}^{SI_U}Z_{A_{F2}} \times {}^{SI_F}X_{A_F}$	${}^{SI_F}R_{A_{F10}} = \begin{bmatrix} {}^{SI_F}X_{A_F} & {}^{SI_F}Y_{A_F} & {}^{SI_U}Z_{A_{F2}} \end{bmatrix}$

4.2.2.4 Hand

Figure 4.4 shows two coordinate frames. The sensor frame is referred to by subscript SI_H (Sensor Inertial Hand). The anatomical frame is referred to by subscript A_H (Anatomical Hand).
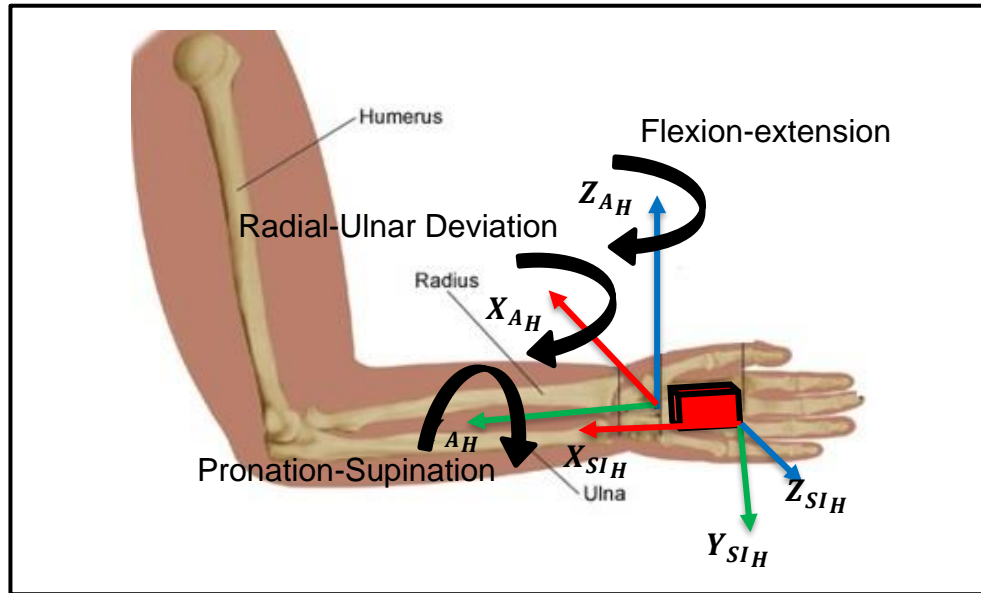
Figure 4.4: Anatomical and Sensor Inertial Frames for the Hand

To determine the anatomical frame's axes, the sensor data was used as follows:

Static Calibrations:

The static calibration position is sitting with the thorax vertical and straight, the upper-arm vertical and aligned with the body, and the forearm and hand in the neutral palm vertical position on the table as shown in Figure 4.4. The acceleration (gravity) data was used to calculate one anatomical reference vector as follows:

$$^{SI_H}\widetilde{Z}_{A_{H1}} \cong -\frac{g}{|g|} \tag{4.18}$$

The subscript A_H and the preceding superscript SI_H signifies that this is an Anatomical Hand axis and that it is expressed in the hand's Sensor Inertial frame. The subscript 1 is used because there is more than one alternative Z-axis.

This is not recommended for use as a primary reference vector (v_{ref1}) because this static calibration position is not considered to be particularly repeatable. Rather it should be used only as a secondary reference vector (v_{ref2}), which is indicated by the tilde ~ symbol over the axis name. It lies only approximately in the *Z*-direction, is a temporary hand *Z*-axis, and the true *Z*-axis is obtained by using the cross product to guarantee that the anatomical frame axes are orthogonal (see Table 4.4).

Dynamic (Functional) Calibrations:

Three calibration movements were used (see Figure 4.4) to calculate the following anatomical reference vectors:

1) Angular velocity ω (gyro) data captured during radial-ulnar deviation was used to calculate:

$$^{SI_H}X_{A_H} = \frac{\omega_{Ud}}{|\omega_{Ud}|} = -\frac{\omega_{Rd}}{|\omega_{Rd}|} \tag{4.19}$$

ω_{Ud} refers to ulnar deviation, while ω_{Rd} refers to radial deviation. According to the right-hand rule and to ensure that the anatomical *X*-axis points medially, if data for ulnar deviation is used, then the sign should remain unchanged. Conversely, if data for radial deviation is used, the vector should be multiplied by -1.

2) Angular velocity data captured during elbow pronation-supination was used to calculate:

$$^{SI_H}Y_{A_H} = -\frac{\omega_{Sup}}{|\omega_{Sup}|} = \frac{\omega_{Pron}}{|\omega_{Pron}|} \tag{4.20}$$

ω_{Sup} refers to supination, while ω_{Pron} refers to pronation.

3) Angular velocity data captured during hand flexion-extension was used to calculate:

$$^{SI_H}Z_{A_{H2}} = \frac{\omega_{Flex}}{|\omega_{Flex}|} = -\frac{\omega_{Ext}}{|\omega_{Ext}|} \tag{4.21}$$

ω_{Flex} refers to flexion, while ω_{Ext} refers to extension. The subscript 2 is used because there is more than one alternative *Z*-axis (see equation 4.18 above).

Given the four anatomical reference vectors above (equations 4.18 to 4.21) and noting that $^{SI_H}\widetilde{Z}_{A_{H1}}$ is only to be used as v_{ref2}, there are 8 ways these can be

91

combined as shown in Table 4.4 together with the corresponding derivations of the anatomical axes and the calibration rotation matrix. The derivations are based on the general approach described by equations 4.1 to 4.4.

Table 4.4: Eight alternative derivations of the calibration rotation matrix for the hand

	v_{ref1}	v_{ref2}	Second and third axes	Calibration rotation matrix
1	${}^{SI_H}X_{A_H}$	${}^{SI_H}\widetilde{Y}_{A_H}$	${}^{SI_H}Z_{A_H} = \dfrac{{}^{SI_H}X_{A_H} \times v_{ref2}}{\left|{}^{SI_H}X_{A_H} \times v_{ref2}\right|},\ {}^{SI_H}Y_{A_H} = {}^{SI_H}Z_{A_H} \times {}^{SI_H}X_{A_H}$	${}^{SI_H}R_{A_{H1}} = \begin{bmatrix}{}^{SI_H}X_{A_H} & {}^{SI_H}Y_{A_H} & {}^{SI_H}Z_{A_H}\end{bmatrix}$
2	${}^{SI_H}X_{A_H}$	${}^{SI_H}\widetilde{Z}_{A_{H2}}$	${}^{SI_H}Y_{A_H} = \dfrac{v_{ref2} \times {}^{SI_H}X_{A_H}}{\left|v_{ref2} \times {}^{SI_H}X_{A_H}\right|},\ {}^{SI_H}Z_{A_H} = {}^{SI_H}X_{A_H} \times {}^{SI_H}Y_{A_H}$	${}^{SI_H}R_{A_{H2}} = \begin{bmatrix}{}^{SI_H}X_{A_H} & {}^{SI_H}Y_{A_H} & {}^{SI_H}Z_{A_H}\end{bmatrix}$
3	${}^{SI_H}X_{A_H}$	${}^{SI_H}\widetilde{Z}_{A_{H1}}$	${}^{SI_H}Y_{A_H} = \dfrac{v_{ref2} \times {}^{SI_H}X_{A_H}}{\left|v_{ref2} \times {}^{SI_H}X_{A_H}\right|},\ {}^{SI_H}Z_{A_H} = {}^{SI_H}X_{A_H} \times {}^{SI_H}Y_{A_H}$	${}^{SI_H}R_{A_{H3}} = \begin{bmatrix}{}^{SI_H}X_{A_H} & {}^{SI_H}Y_{A_H} & {}^{SI_H}Z_{A_H}\end{bmatrix}$
4	${}^{SI_H}Y_{A_H}$	${}^{SI_H}\widetilde{X}_{A_H}$	${}^{SI_H}Z_{A_H} = \dfrac{v_{ref2} \times {}^{SI_H}Y_{A_H}}{\left|v_{ref2} \times {}^{SI_H}Y_{A_H}\right|},\ {}^{SI_H}X_{A_H} = {}^{SI_H}Y_{A_H} \times {}^{SI_H}Z_{A_H}$	${}^{SI_H}R_{A_{H4}} = \begin{bmatrix}{}^{SI_H}X_{A_H} & {}^{SI_H}Y_{A_H} & {}^{SI_H}Z_{A_H}\end{bmatrix}$
5	${}^{SI_H}Y_{A_H}$	${}^{SI_H}\widetilde{Z}_{A_{H2}}$	${}^{SI_H}X_{A_H} = \dfrac{{}^{SI_H}Y_{A_H} \times v_{ref2}}{\left|{}^{SI}Y_{A_H} \times v_{ref2}\right|},\ {}^{SI_H}Z_{A_H} = {}^{SI_H}X_{A_H} \times {}^{SI_H}Y_{A_H}$	${}^{SI_H}R_{A_{H5}} = \begin{bmatrix}{}^{SI_H}X_{A_H} & {}^{SI_H}Y_{A_H} & {}^{SI_H}Z_{A_H}\end{bmatrix}$
6	${}^{SI_H}Y_{A_H}$	${}^{SI_H}\widetilde{Z}_{A_{H1}}$	${}^{SI_H}X_{A_H} = \dfrac{{}^{SI_H}Y_{A_H} \times v_{ref2}}{\left|{}^{SI}Y_{A_H} \times v_{ref2}\right|},\ {}^{SI_H}Z_{A_H} = {}^{SI_H}X_{A_H} \times {}^{SI_H}Y_{A_H}$	${}^{SI_H}R_{A_{H6}} = \begin{bmatrix}{}^{SI_H}X_{A_H} & {}^{SI_H}Y_{A_H} & {}^{SI_H}Z_{A_H}\end{bmatrix}$
7	${}^{SI_H}Z_{A_{H2}}$	${}^{SI_H}\widetilde{X}_{A_H}$	${}^{SI_H}Y_{A_H} = \dfrac{{}^{SI_H}Z_{A_{H2}} \times v_{ref2}}{\left|{}^{SI_H}Z_{A_{H2}} \times v_{ref2}\right|},\ {}^{SI_H}X_{A_H} = {}^{SI_H}Y_{A_H} \times {}^{SI_H}Z_{A_{H2}}$	${}^{SI_H}R_{A_{H7}} = \begin{bmatrix}{}^{SI_H}X_{A_H} & {}^{SI_H}Y_{A_H} & {}^{SI_H}Z_{A_{H2}}\end{bmatrix}$
8	${}^{SI_H}Z_{A_{H2}}$	${}^{SI_H}\widetilde{Y}_{A_H}$	${}^{SI_H}X_{A_H} = \dfrac{v_{ref2} \times {}^{SI_H}Z_{A_{H2}}}{\left|v_{ref2} \times {}^{SI_H}Z_{A_{H2}}\right|},\ {}^{SI_H}Y_{A_H} = {}^{SI_H}Z_{A_{H2}} \times {}^{SI_H}X_{A_H}$	${}^{SI_H}R_{A_{H8}} = \begin{bmatrix}{}^{SI_H}X_{A_H} & {}^{SI_H}Y_{A_H} & {}^{SI_H}Z_{A_{H2}}\end{bmatrix}$

4.3 Joint Rotation Matrices and Joint kinematics

4.3.1 Basic Principles

In what follows, it is assumed that all MIMUs (sensors) share the same global reference frame (SG) determined by gravity and magnetic north.

To find the joint rotation matrix describing the orientation of a distal segment with respect to its adjacent proximal segment, first the orientations of the corresponding sensors in their common global frame (i.e. the sensor outputs) are obtained, which are represented by the following rotation matrices:

$^{SG}R_{SI_P}$: Orientation of the Sensor Inertial frame (SI_P) on the proximal segment with respect to the earth-fixed Sensor Global frame (SG);

$^{SG}R_{SI_D}$: Orientation of the Sensor Inertial frame (SI_D) on the distal segment with respect to the earth-fixed Sensor Global frame (SG).

where the subscripts P and D refer to the proximal and distal segments respectively, which can be the thorax T, upper-arm U, forearm F or hand H. Together with the calibration rotation matrices ($^{SI_T}R_{A_T}$, $^{SI_U}R_{A_U}$, $^{SI_F}R_{A_F}$, $^{SI_H}R_{A_H}$) derived in the previous sections, these can then be used to obtain the orientation of each segment's anatomical frame with respect to the earth-fixed Sensor Global frame (SG) as follows:

$$^{SG}R_{A_P} = {}^{SG}R_{SI_P}{}^{SI_P}R_{A_P} \tag{4.22}$$

$$^{SG}R_{A_D} = {}^{SG}R_{SI_D}{}^{SI_D}R_{A_D} \tag{4.23}$$

Then the joint rotation matrix describing the orientation of the distal segment with respect to its adjacent proximal segment is given by:

$$^{A_P}R_{A_D} = {}^{A_P}R_{SG}{}^{SG}R_{A_D} = \left({}^{SG}R_{A_P}\right)^{T}{}^{SG}R_{A_D} \tag{4.24}$$

The symbol (exponent) **T** refers to the matrix transpose. The joint rotation matrix can be used to derive many other ways of representing the orientation of a distal segment with respect to its adjacent proximal segment (Aurelio Cappozzo, Della Croce, Leardini, & Chiari, 2005), including:

- Euler Angles (or Cardan angles) which are often referred to as roll, pitch and yaw.
- A unit quaternion (also known as Euler parameters).
- The orthogonal projections of the orientation vector (N.B. not strictly a vector).
- Joint angles obtained by projecting axes of one coordinate frame onto planes of the other coordinate frame.

All of these representations are interchangeable. However, when plotting these against time, quite different curves result and so it is far from obvious which representation is most useful. Indeed, the biomechanics community has not reached agreement on this (Aurelio Cappozzo et al., 2005).

4.3.2 Joint Rotation Matrix for the Thorax

Because the thorax has no adjacent proximal segment, its orientation was calculated relative to the camera defined LAB frame. This was done so that the MIMU based results could be compared with the camera-based results. To do this the orientation of the Sensor Global (SG) frame relative to the LAB frame was required, which was calculated using data from the static calibration of the camera system as follows:

$$^{LAB}R_{SG} = {}^{LAB}R_{SM_T} \, {}^{SI_T}R_{SG} = {}^{LAB}R_{SM_T} \left({}^{SG}R_{SI_T}\right)^{\mathbf{T}} \tag{4.25}$$

where $^{LAB}R_{SM_T}$ is the orientation of the marker-based sensor frame (SM_T) relative to the LAB frame and $^{SG}R_{SI_T}$ is the orientation of the corresponding Sensor Inertial frame relative to the Sensor Global frame (i.e. the sensor output). It is assumed that the Sensor Marker frame (SM) is equivalent to the Sensor Inertial frame (SI) as illustrated in Figure 4.5. The derivation of $^{LAB}R_{SM_T}$ is described in Appendix 1.

Then, for all dynamic trials, the orientation of the thorax relative to the LAB frame is given by:

$$^{LAB}R_{A_T} = {}^{LAB}R_{SG}\,{}^{SG}R_{A_T} \tag{4.26}$$
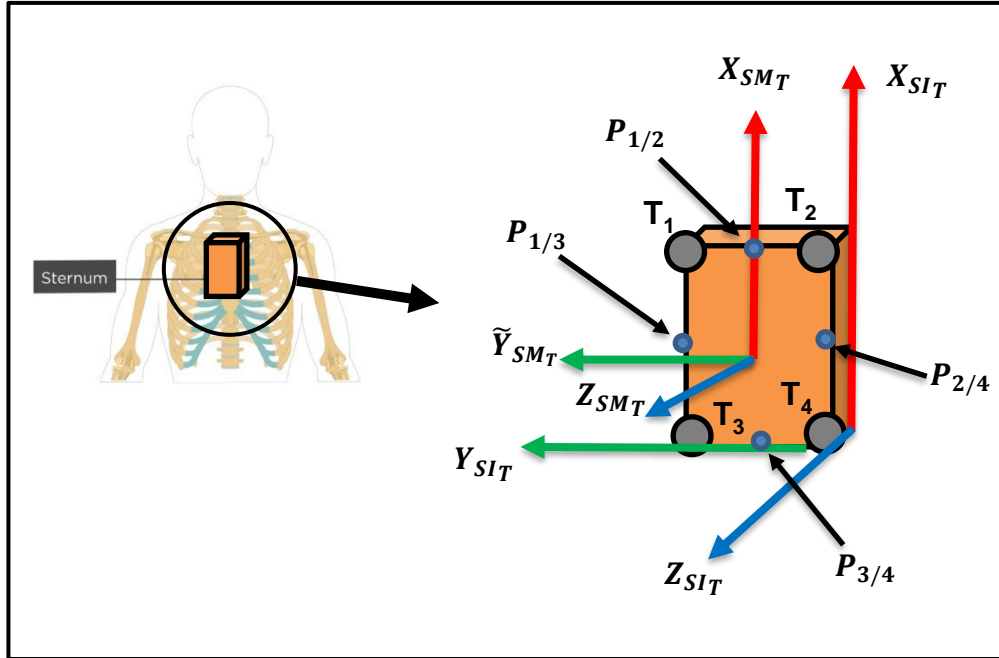
Figure 4.5: Sensor Marker Frame and Sensor Inertial Frame for the thorax

4.3.3 Joint Rotation Matrix for the Shoulder

Using equation 4.24, the joint rotation matrix for the shoulder (orientation of the distal upper-arm with respect to the proximal thorax) is given by:

$$^{A_T}R_{A_U} = {}^{A_T}R_{SG}\,{}^{SG}R_{A_U} = \left({}^{SG}R_{A_T}\right)^{\mathrm{T}}{}^{SG}R_{A_U} \tag{4.27}$$

4.3.4 Joint Rotation Matrix for the Elbow

Using equation 4.24, the joint rotation matrix for the elbow (orientation of the distal forearm with respect to the proximal upper-arm) is given by:

$$^{A_U}R_{A_F} = {}^{A_U}R_{SG}\,{}^{SG}R_{A_F} = \left({}^{SG}R_{A_U}\right)^{\mathrm{T}}{}^{SG}R_{A_F} \tag{4.28}$$

4.3.5 Joint Rotation Matrix for the Wrist

Using equation 4.24, the joint rotation matrix for the wrist (orientation of the distal hand with respect to the proximal forearm) is given by:

$$^{A_F}R_{A_H} = {}^{A_F}R_{SG}\,{}^{SG}R_{A_H} = \left({}^{SG}R_{A_F}\right)^{\mathrm{T}}{}^{SG}R_{A_H} \qquad\qquad (4.29)$$

4.4 Issues with the MIMU orientation estimators

4.4.1 Working with the Xsens orientation estimator

In the first implementation of the methods described above, the orientation estimator (Kalman filter) provided by the supplier of the MIMUs (Xsens) was used to obtain the sensor orientations relative to their common Sensor Global frame: $^{SG}R_{SI_T}$, $^{SG}R_{SI_U}$, $^{SG}R_{SI_F}$, and $^{SG}R_{SI_H}$. However, following difficulties during the testing of the MATLAB code, it appeared that each sensor was referencing a different Sensor Global frame, rather than a common Sensor Global based on vertical and magnetic north. After some investigation, it was concluded that an Xsens heading reset may have occurred prior to data capture. Although there is no record of this in the written protocol, this seemed to explain the anomalies in the results. A heading reset adopts the horizontal projection of the sensor X-axis, at the time of the reset, as the new global X-axis. Therefore, unless the sensors are carefully aligned at the instant of the heading reset, they will have different Sensor Global frames. Furthermore, there also appeared to be issues with the Xsens estimator taking too long to settle, so that the first ~2 seconds of data is not usable. Unfortunately, this appears to affect the results and the written protocol is too vague on the time between starting an MIMU recording session and the movement beginning.

To overcome the first problem, it was decided that the laboratory frame (LAB), defined by the camera system, should be used as the common global frame. This was possible because each sensor had reflective markers attached at each corner so that they could act as technical clusters for the purposes of the CAST

method (see section 3.3.2). These markers were used to construct Sensor Marker (**SM**) frames that are approximately aligned with the Sensor Inertial (**SI**) frames (see Figure 4.5 for example).

Then, using data from the static calibration of the camera system, the orientations of the sensors in the LAB frame were obtained ($^{LAB}R_{SM_T}$, $^{LAB}R_{SM_U}$, $^{LAB}R_{SM_F}$, $^{LAB}R_{SM_H}$). These were used with the corresponding orientations of the sensors in their respective Sensor Global frames (sensor outputs $^{SG_T}R_{SI_T}$, $^{SG_U}R_{SI_U}$, $^{SG_F}R_{SI_F}$, and $^{SG_H}R_{SI_H}$) to derive the orientation of the different Sensor Global frames relative to the LAB frame as follows:

$$^{LAB}R_{SG_K} = {}^{LAB}R_{SM_K}{}^{SI_K}R_{SG_K} = {}^{LAB}R_{SM_K}\left({}^{SG_K}R_{SI_K}\right)^{\mathrm{T}} \tag{4.30}$$

where the subscript **K** refers to the segment, which can be the thorax **T**, upper-arm **U**, forearm **F** or hand **H**. It is assumed that each Sensor Marker frame (**SM$_K$**) is equivalent to the corresponding Sensor Inertial frame (**SI$_K$**). The derivation of $^{LAB}R_{SM_K}$ for the four segments is described in Appendix 1.

Then, for all dynamic trials, the orientation of the segments relative to the LAB frame is given by:

$$^{LAB}R_{A_K} = {}^{LAB}R_{SG_K}{}^{SG_K}R_{A_K} \tag{4.31}$$

Whilst working to debug the corresponding MATLAB code, a new 2019 version of MATLAB was released, which included a MIMU toolbox with alternative orientation estimators that can work with the raw data from the Xsens MIMUs. This led to the solution described in the next section and meant that the considerable effort invested in the solution described above had been unnecessary.

4.4.2 Working with the MATLAB orientation estimators

In 2019, MATLAB introduced a new Sensor Fusion and Tracking toolbox (The MathWorks, 2019). This toolbox includes algorithms that can fuse the data from a 3-axis accelerometer and either (or both of) a 3-axis rate-gyroscope or (and) a

3-axis magnetometer mounted in the same box (i.e. with common sensor axes) to estimate the orientation of the box (e.g. an MIMU box). Specifically, the following orientation estimators (filters) are available, with their MATLAB function names shown in brackets:

1) **Magnetometer and accelerometer filter (ecompass):** This estimator fuses only accelerometer and magnetometer data.
2) **Accelerometer and gyroscope filter (imufilter):** This estimator fuses only accelerometer and rate-gyroscope data.
3) **Accelerometer, gyroscope, and magnetometer filter (ahrsfilter):** This estimator fuses all three types of raw data (accelerometer, rate-gyroscope, and magnetometer).

In all three cases, orientation can be provided in either quaternion or rotation matrix form, which describe the orientation of the Sensor Global (*SG*) frame with respect to the Sensor Inertial (*SI*) frame. In other words, the estimator's output $^{SI_K}R_{SG_K}$. In this case, the *SG* frame axes *X-Y-Z* correspond to North-East-Down (NED).

A comparison of these filters was undertaken to establish the best one for the purposes of this work. In this context, there were two requirements:

a) The estimator must correctly find north and vertical so that all MIMUs share the same global frame (*SG*).
b) The estimator must settle rapidly so that the data collected after the first second of each movement trial (MIMU recording session) is correct, where a movement trial corresponds to one execution of a calibration movement or a functional task as described in section 3.4.2 (chapter 3).

The results of this comparison are as follows:
1) **ecompass:** Although this estimator is susceptible to sensor noise, it correctly finds the location of north and vertical. However, because the algorithm is memoryless (independent of its history), the estimated orientation is not smooth, being significantly affected by accelerometer and magnetometer noise.

2) <u>imufilter</u>: Because this estimator does not process magnetometer data, it does not correctly estimate the direction of north. It simply assumes the sensor's *X*-axis is initially pointing northward and, hence, different MIMUs will not share the same global frame (SG). Furthermore, there is a significant settling time ($time\ constant \cong 2sec$), which means that it does not satisfy the second criterion above.

3) <u>ahrsfilter</u>: This estimator combines the previous algorithms to produce a smooth estimate of sensor orientation, while correctly estimating the direction of north and vertical. However, again there is a significant settling time ($time\ constant \cong 2sec$), which means that it does not satisfy the second criterion above.

Therefore, despite the noisy output, the **ecompass** estimator has been used in this work because it settles quickly as well as correctly estimating the direction of north and vertical.

Using the selected MATLAB filter, it then appeared that the sensors were using the same Sensor Global frame and the mathematics described in section 4.3 could be applied directly, without the need to describe segment orientations relative to the LAB frame as proposed in section 4.4.1.

Chapter 5 – The Results

5.1 Introduction

In this chapter, the alternative calibration methods described in Chapter 4 are compared. Specifically, the alternative calibration rotation matrices listed in Tables 4.1 to 4.4 are compared. Three different sets of results are presented. Firstly, for each body segment, the orientations of the alternative anatomical frames, relative to their common sensor inertial frame, are compared (each one corresponding to one alternative calibration rotation matrix). Secondly, for each joint, the best pair of calibration rotation matrices (i.e. for proximal and distal segments) is found using a sequential assessment process. Finally, for each joint, the best pair of calibration rotation matrices is found using an independent assessment process.

5.2 Calibration rotation matrices

The calibration rotation matrix, $^{SI_k}R_{A_k}$, is a 3X3 matrix that represents the orientation of a body segment's Anatomical frame (A_k) with respect to that segment's Sensor Inertial frame (SI_k), where k is the segment (T, U, F or H). The calibration rotation matrices for each segment have been derived using alternative calibration methods as explained in Chapter 4, section 4.2, and summarised in Tables 4.1 to 4.4 for the thorax, upper-arm, forearm and hand respectively.

The static and dynamic calibration trials have all been repeated 4 times. Thus, each alternative calibration rotation matrix for each segment was derived 4 times. These 4 repetitions were then averaged using a rotation vector method described in (Sharf, Wolf, & Rubin, 2010). Specifically, each of the 4 rotation matrices was converted into its axis-angle representation using a MATLAB function and then into a rotation vector by multiplying the absolute angle (magnitude) by the unit vector (axis). Then a simple arithmetic average of the 4 rotation vectors was calculated, which has been shown to be a robust and meaningful average (Sharf

et al., 2010). Finally, the average rotation vector was converted back into axis-angle and then into an "averaged" calibration rotation matrix. This averaging of 4 repeats was done for each alternative calibration rotation matrix for each segment. As well as being a relatively simple calculation, this method of deriving an average rotation produces results that are close to computationally intensive bi-invariant solutions, which produce orientation curves that are independent of how one selects either the fixed or the moving reference frames (Sharf et al., 2010).

The columns of a calibration rotation matrix are the three-unit vectors for the axes of the Anatomical frame (A_k) expressed in the Sensor Inertial frame (SI_k). Therefore, the results can be presented by showing the orientations of the alternative anatomical frames in their sensor inertial frames. In the following sections, the results for participant 1 are presented.

5.2.1 Thorax

The 8 alternative calibration rotation matrices for the thorax ($^{SI_T}R_{A_T}$) have been computed as described in Table 4.1. The columns of each rotation matrix represent the axes of the corresponding anatomical frame and the alternatives are shown in Figure 5.1.

Figure 5.1: Eight alternative thorax anatomical frames for participant 1, expressed in their sensor inertial frame. *X*-axis in red, *Y*-axis in green, and *Z*-axis in blue.

The alternative frames are approximately aligned with the sensor inertial frame, which is a result of the thorax sensor being physically aligned with the anatomy so that, for example, the calibration rotation matrix is approximately equal to the identity matrix. This was done so that an anatomical frame based on careful sensor alignment (an approximate geometric relationship between sensor frame and anatomical frame) could be compared with anatomical frames based on the alternative calibration approaches.

5.2.2 Upper-arm

The 8 alternative calibration rotation matrices for the upper-arm ($^{SI_U}R_{A_U}$) have been computed as described in Table 4.2. The columns of each rotation matrix represent the axes of the corresponding anatomical frame and the alternatives are shown in Figure 5.2.

Figure 5.2: Eight alternative upper-arm anatomical frames for participant 1, expressed in their sensor inertial frame. *X*-axis in red, *Y*-axis in green, and *Z*-axis in blue.

The alternative frames are approximately aligned with the sensor inertial frame, which is a result of the upper-arm sensor being physically aligned with the anatomy so that, for example, the calibration rotation matrix is approximately equal to the identity matrix. As before, this was done so that an anatomical frame based on careful sensor alignment (an approximate geometric relationship between sensor frame and anatomical frame) could be compared with anatomical frames based on the alternative calibration approaches.

5.2.3 Forearm

The 10 alternative calibration rotation matrices for the forearm ($^{SI_F}R_{A_F}$) have been computed as described in Table 4.3. The columns of each rotation matrix represent the axes of the corresponding anatomical frame and the alternatives are shown in Figure 5.3.

Figure 5.3: Ten alternative forearm anatomical frames for participant 1, expressed in their sensor inertial frames. *X*-axis in red, *Y*-axis in green, and *Z*-axis in blue.

The alternative frames are approximately aligned with the sensor inertial frame, which is a result of the forearm sensor being physically aligned with the anatomy so that, for example, the calibration rotation matrix is approximately equal to the identity matrix. As before, this was done so that an anatomical frame based on careful sensor alignment (an approximate geometric relationship between sensor frame and anatomical frame) could be compared with anatomical frames based on the alternative calibration approaches.

5.2.4 Hand

The 8 alternative calibration rotation matrices for the hand ($^{SI_H}R_{A_H}$) have been computed as described in Table 4.4. The columns of each rotation matrix represent the axes of the corresponding anatomical frame and the alternatives are shown in Figure 5.4.
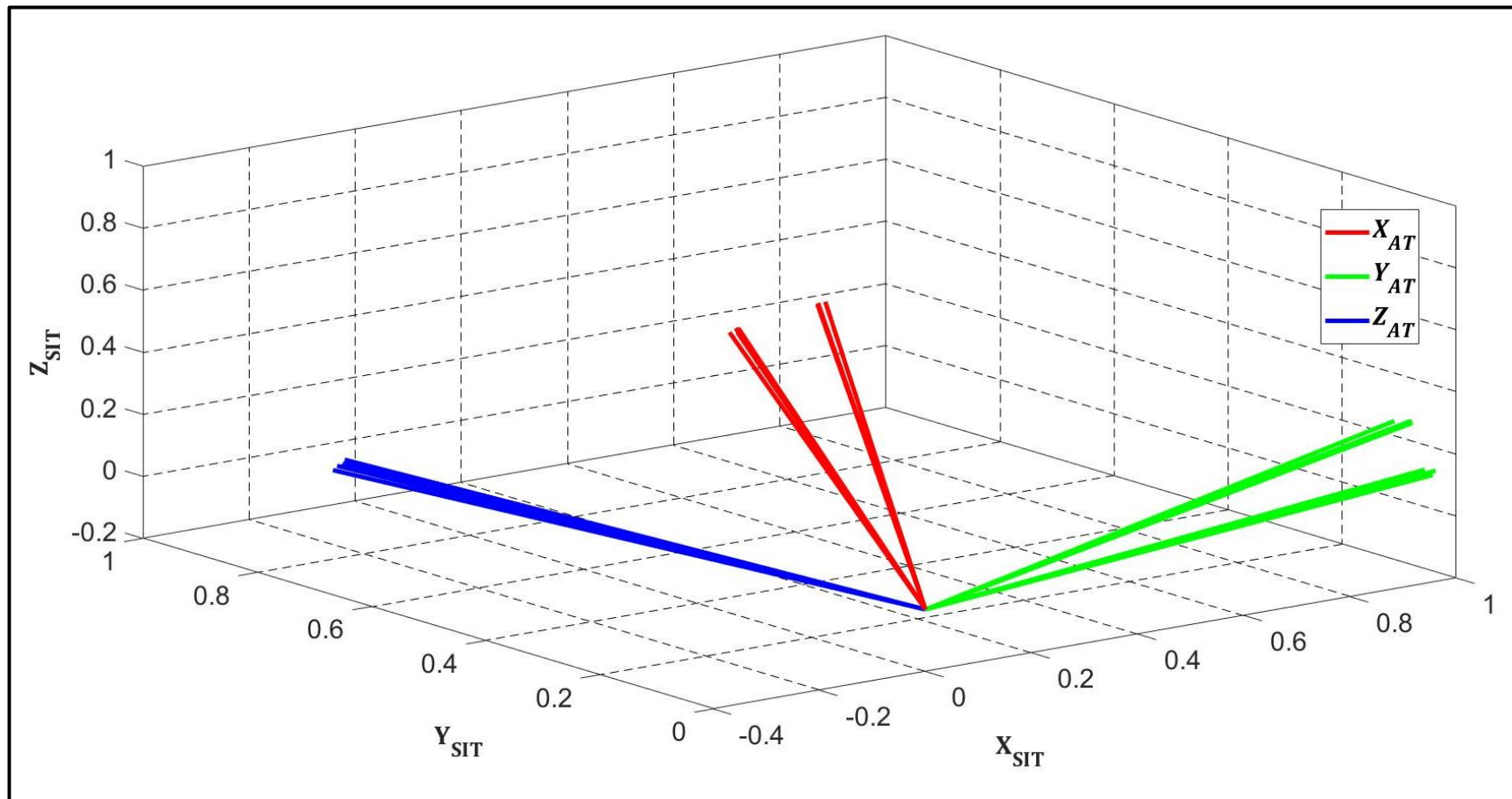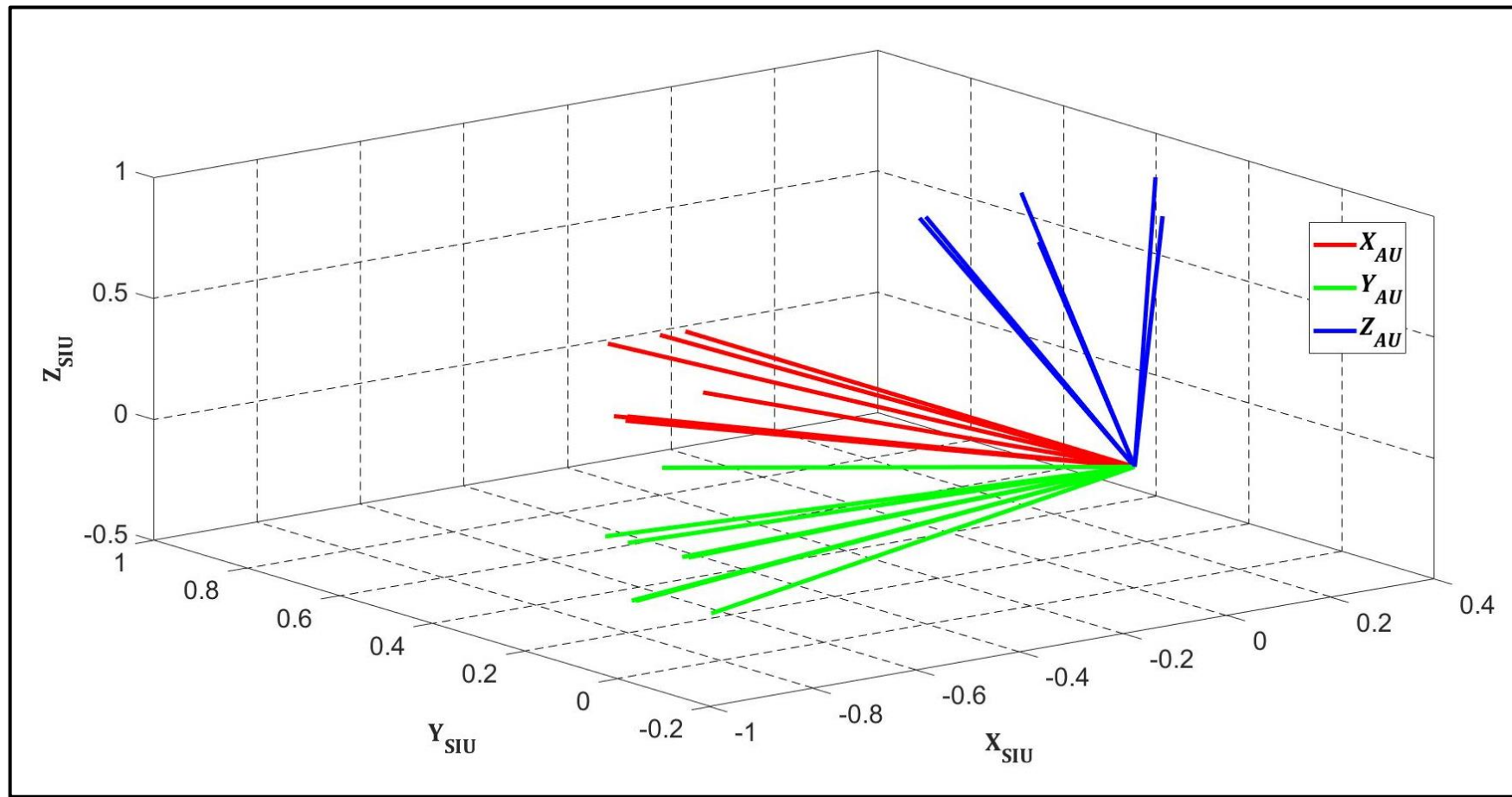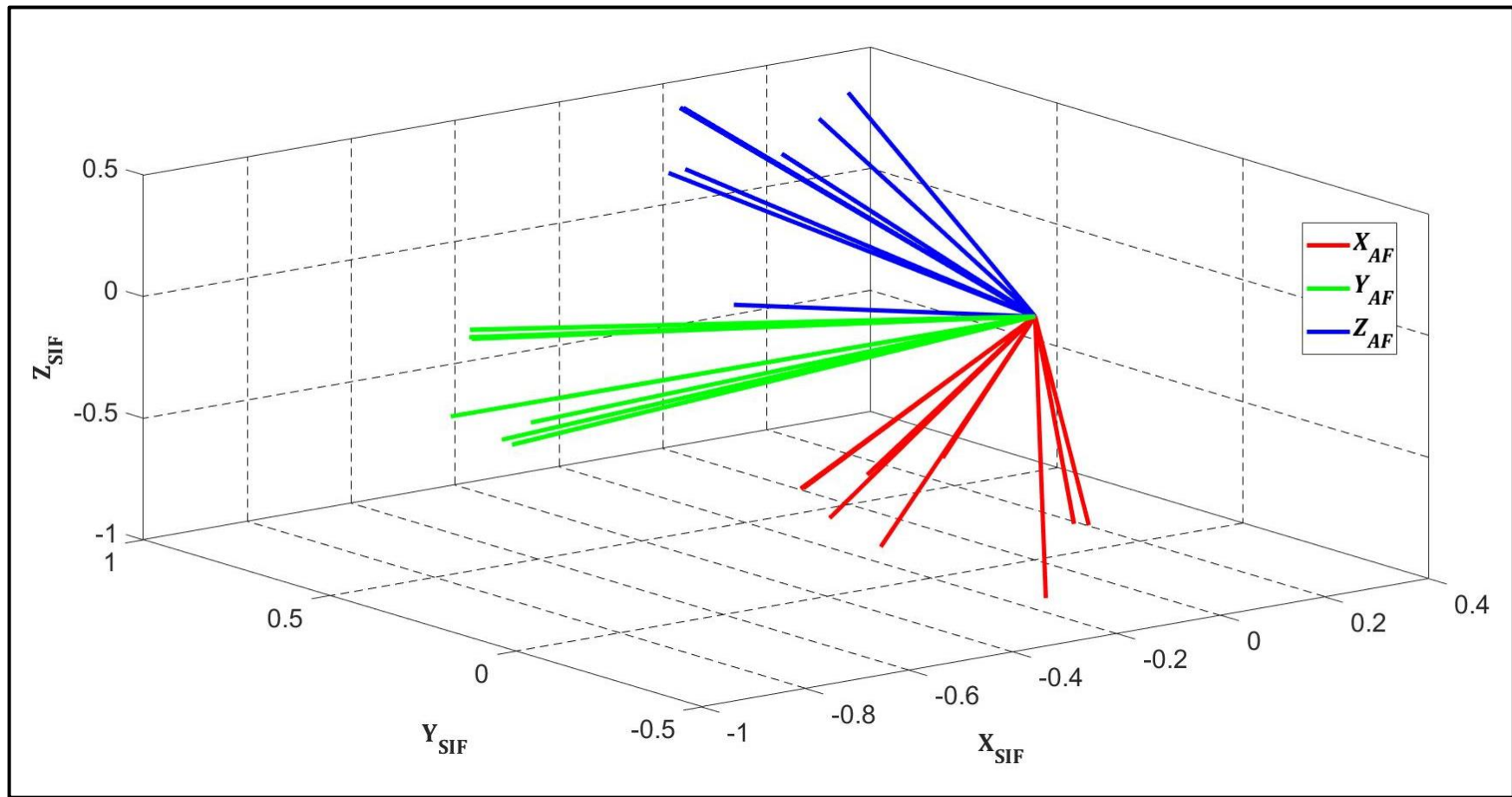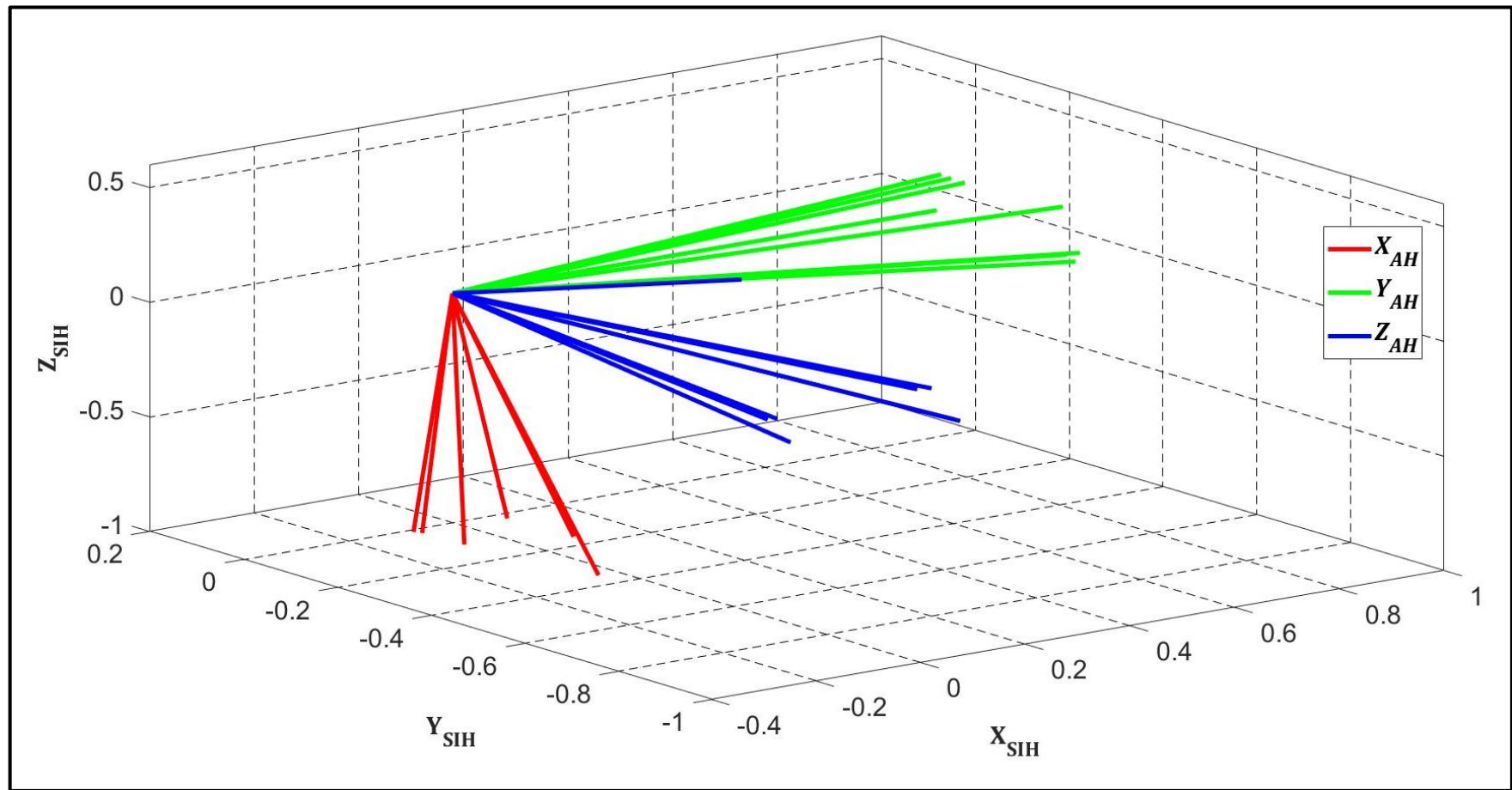
Figure 5.4: Eight alternative hand anatomical frames for participant 1, expressed in their sensor inertial frame. *X*-axis in red, *Y*-axis in green, and *Z*-axis in blue.

The alternative frames are approximately aligned with the sensor inertial frame, which is a result of the hand sensor being physically aligned with the anatomy so that, for example, the calibration rotation matrix is approximately equal to the identity matrix. As before, this was done so that an anatomical frame based on careful sensor alignment (an approximate geometric relationship between sensor frame and anatomical frame) could be compared with anatomical frames based on the alternative calibration approaches.

5.3 Sequential assessment of alternative calibration methods

Using the methods explained in Chapter 4, section 4.3, for each anatomical joint, the alternative calibration rotation matrices described in the previous section have been used to calculate alternative sequences of sensor (MIMU) derived joint rotation matrices ($^{A_P}R_{A_{D_{MIMU}}}$). These describe the orientation of the joint's distal segment relative to its proximal segment (henceforth referred to as joint orientation) throughout 4 functional tasks, each repeated 4 times, as described in Chapter 3, section 3.4.2. Each alternative sequence of joint orientations corresponds to a particular pair of calibration rotation matrices.

The alternative MIMU sequences were compared with the equivalent sequence of V3D joint rotation matrices ($^{A_P}R_{A_{D_{V3D}}}$) obtained from an assumed gold standard: a VICON camera based motion capture system (stereophotogrammetry system), with the data post-processed using Visual 3D (V3D), as described in Chapter 3, section 3.5.1 These comparisons were done separately for five participants to establish whether the same calibration methods can be used with different individuals, a necessity if the methods are to be useful.

To compare the alternative joint orientation sequences, for every sample (camera frame), an error rotation matrix was calculated between the MIMU derived joint orientation and the V3D derived joint orientation as follows (Equation 5.1).

$$^{A_{D_{V3D}}}R_{A_{D_{MIMU}}} = \left[^{A_P}R_{A_{D_{V3D}}}\right]^{\mathbf{T}} \cdot {}^{A_P}R_{A_{D_{MIMU}}} \tag{5.1}$$

where ${}^{A_P}R_{A_{D_{MIMU}}}$ is the joint rotation matrix based on MIMU data, and ${}^{A_P}R_{A_{D_{V3D}}}$ is the joint rotation matrix based on V3D data.

This describes the rotation error between the MIMU distal frame and the V3D distal frame, where the proximal frame is adopted as the common reference frame. Then, for a whole sequence, the error rotation matrices were converted into error rotation vectors and averaged to give a single error measure, namely the average error rotation vector, henceforth simply referred to as the error rotation vector. Where a scalar was required for minimisation purposes, the magnitude of the error rotation vector has been used. This was done for each alternative sequence of joint orientations, corresponding to a particular pair of calibration rotation matrices.

In this section, a sequential approach is used where, firstly, the best thorax calibration rotation matrix, that minimises the magnitude of the error rotation vector, is found for the lab to thorax pseudo joint. This is then used as the proximal calibration rotation matrix for the shoulder joint and the best distal (upper-arm) calibration rotation matrix is found. In turn, this is used as the proximal calibration rotation matrix for the elbow joint and the best distal (forearm) calibration rotation matrix is found. Finally, this is used as the proximal calibration rotation matrix for the wrist joint and the best distal (hand) calibration rotation matrix is found.

The sequential approach has the advantage of minimising the number of calibration trials by using only one calibration rotation matrix per segment, even when that segment is involved in two joints. However, this means that it is a suboptimal method because it does not find the optimum pair of calibration rotation matrices for each joint, unlike the independent approach described in section 5.4.

All of these calculations have been implemented in MATLAB with the exception of the V3D joint rotation matrices (${}^{A_P}R_{A_{D_{V3D}}}$), which were outputs from the Visual 3D post-processing of the camera data. The following subsections describe the results of the 4 sequential stages of assessment for the lab-thorax, shoulder, elbow and wrist joints respectively.

5.3.1 Thorax

The error rotation vectors between each alternative MIMU sequence and the gold standard (V3D) sequence for the thorax and for participant 1 are presented in Figures 5.5 and 5.6. The magnitude (absolute angle) of the error rotation vector was used to select the best alternative (best thorax calibration rotation matrix). Note that, for the lab-thorax pseudo joint there is no proximal calibration rotation matrix because the proximal frame is the lab frame, not an anatomical frame. Alternative 7 has the lowest error.
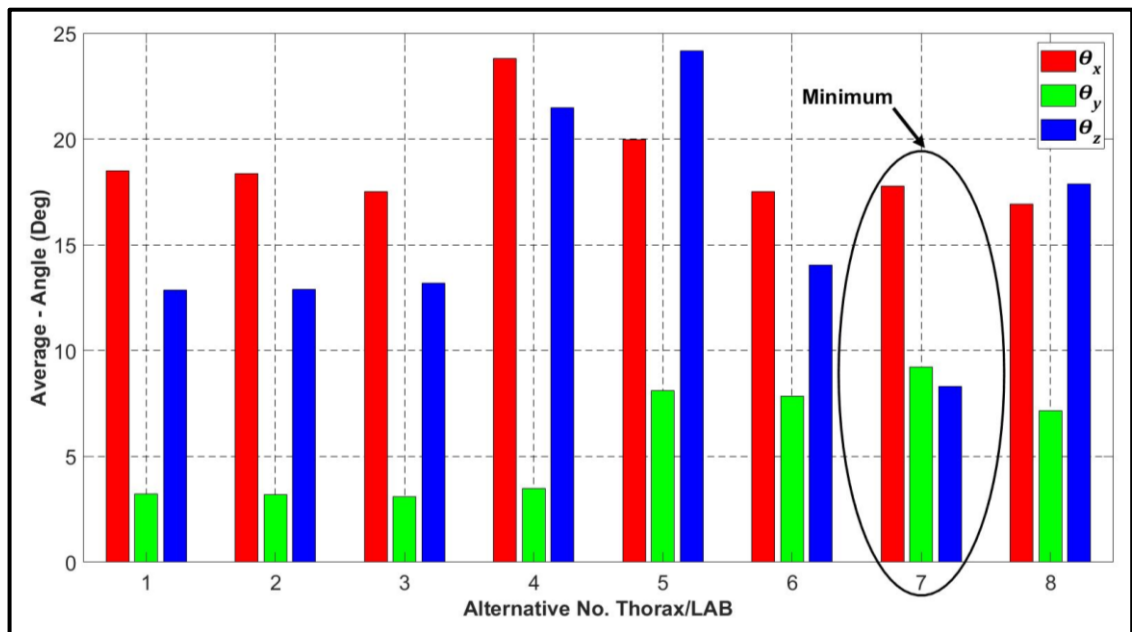
Figure 5.5: Error rotation vectors for the 8 alternative thorax calibration rotation matrices for participant 1

Figure 5.6: Magnitudes of the error rotation vectors for the 8 alternative thorax calibration rotation matrices for participant 1

Table 5.1 shows the numerical error data for the best thorax calibration rotation matrix for all five participants (e.g. alternative 7 for participant 1). This error rotation vector can be used to provide a graphical representation of the error between the MIMU derived joint orientation and the V3D joint orientation. One example is shown in Figure 5.7 – alternative 7 for participant 1.

Table 5.1: Error rotation vector for the lab-thorax pseudo joint

Lab-Thorax Joint					
	Thorax	**Rotation vector components**			**Magnitude**
Participant	Alternative	θ_x	θ_y	θ_z	θ
1	7	17.8°	9.2°	8.3°	21.7°
2	4	3.9°	1.3°	7.7°	8.7°
3	7	-17°	2.6°	12.9°	21.5°
4	1 *or 7 (+7%)*	-15.6° *or -16.9°*	9.3° *or 1.9°*	2.2° *or 9.6°*	18.3° *or 19.5°*
5	1	-14.7°	16.6°	9.5°	24.1°

113

Considering column 2 of Table 5.1, there is insufficient agreement between participants, which is necessary if a majority vote on the best alternative is to have an acceptably low probability of occurring by chance. However, after looking at the average errors across all alternatives for all participants, a good second choice for participant 4 was identified, which only increased the error by 7% (about 1º). This leads to agreement between 3 out of 5 participants and the probability of this occurring by chance alone is around 12% (see Appendix 2).
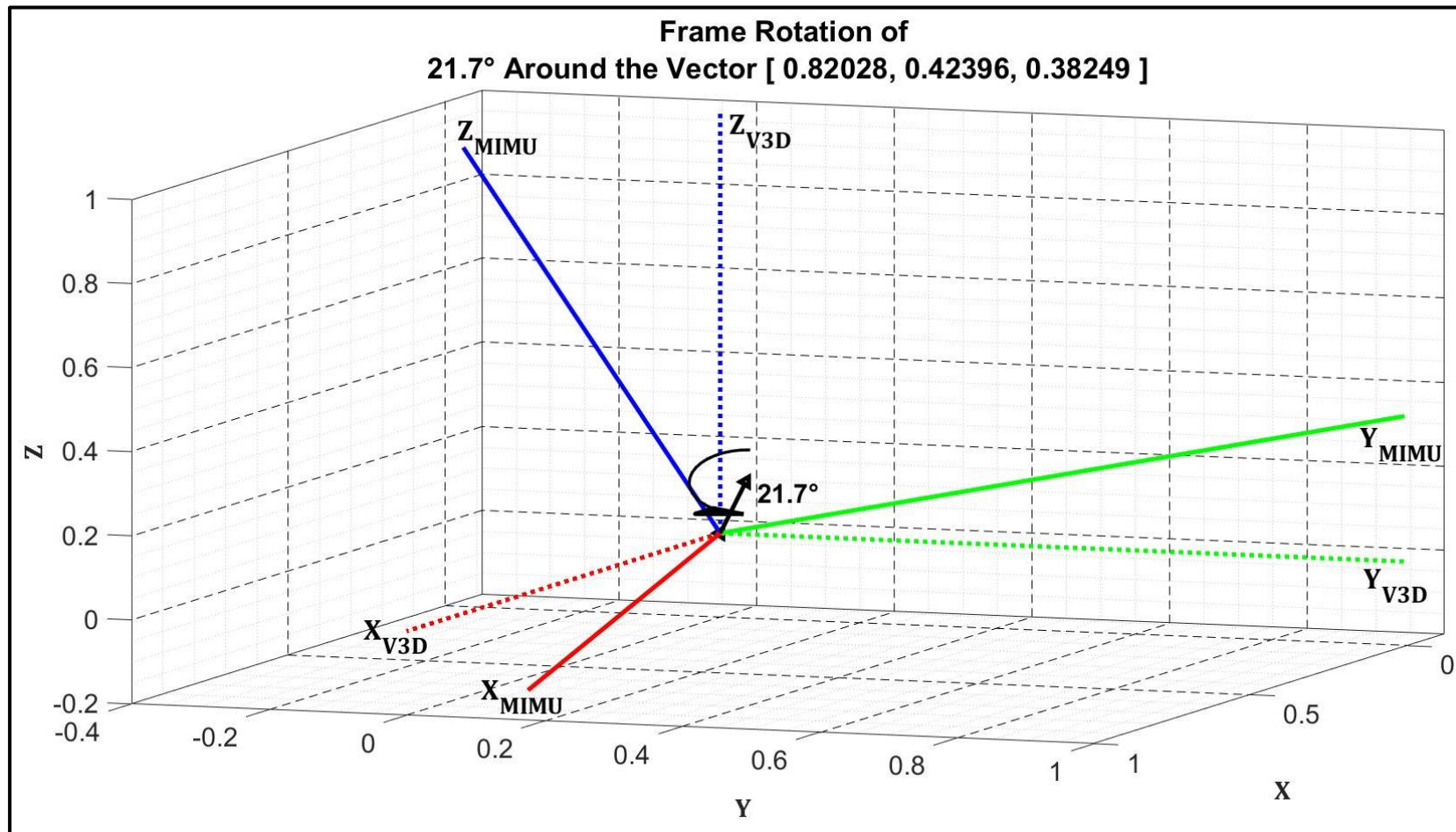
Figure 5.7: The lab-thorax error rotation vector for participant 1, which is a graphical representation of the average error between MIMU joint orientation and V3D joint orientation. The axis-angle description is shown graphically by the black arrow showing the unique axis and angle of rotation.

5.3.2 Shoulder

The error rotation vectors between each alternative MIMU sequence and the gold standard (V3D) sequence for the shoulder and for participant 1 are presented in Figures 5.8 and 5.9. The magnitude (absolute angle) of the error rotation vector was used to select the best alternative (best upper-arm calibration rotation matrix), noting that the proximal (thorax) calibration rotation matrix has been established at the previous stage (see previous section). Alternative 5 has the lowest error.

Figure 5.8: Error rotation vectors for the 8 alternative upper-arm calibration rotation matrices (used with alternative 7 for the thorax) for participant 1.
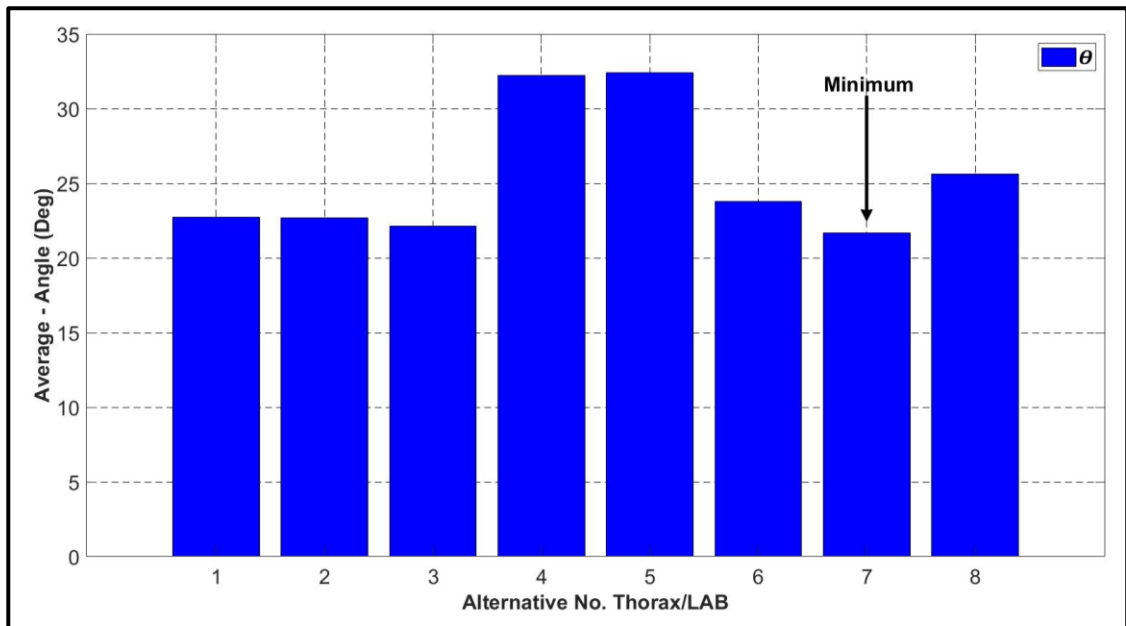
Figure 5.9: Magnitudes of the error rotation vectors for the 8 alternative upper-arm calibration rotation matrices (used with alternative 7 for the thorax) for participant 1

Table 5.2 shows the numerical error data for the best upper-arm calibration rotation matrix for all five participants (e.g. alternative 5 for participant 1, used with alternative 7 for the thorax). This error rotation vector can be used to provide a graphical representation of the error between the MIMU derived joint orientation and the V3D joint orientation. One example is shown in Figure 5.10 – thorax alternative 7 and upper-arm alternative 8 for participant 1.

Considering column 3 of Table 5.2, there is agreement between 3 out of 5 participants, which means a majority vote on the best alternative has an acceptably low probability of occurring by chance. Nevertheless, after looking at the average errors across all alternatives for all participants, a good second choice for participant 1 was identified, which only increased the error by 6% (about 1°). This leads to agreement between 4 out of 5 participants and the probability of this occurring by chance alone is less than 1% (see Appendix 2).

Table 5.2: Error rotation vectors for the shoulder joint

| Shoulder Joint						
	Thorax	**Upper-arm**	**Rotation vector components**			**Magnitude**
Participant	Alternative	Alternative	θ_x	θ_y	θ_z	θ
1	7	5 *or 8 (6%)*	-2.3º *or 9.9º*	18.9º *or 17.9º*	4.8º *or 3.5º*	19.6º *or 20.8º*
2	4	8	-4.9º	13.3º	-0.3º	14.2º
3	7	8	0.8º	-23.3º	4.8º	23.8º
4	7	6	20.4º	-6.5º	6.2º	22.3º
5	1	8	-5º	-4.1º	1.9º	6.8º

Figure 5.10: The shoulder error rotation vector for participant 1, which is a graphical representation of the average error between MIMU joint orientation and V3D joint orientation. The axis-angle description is shown graphically by the black arrow showing the unique axis and angle of rotation

5.3.3 Elbow

The error rotation vectors between each alternative MIMU sequence and the gold standard (V3D) sequence for the elbow and for participant 1 are presented in Figures 5.11 and 5.12. The magnitude (absolute angle) of the error rotation vector was used to select the best alternative (best forearm calibration rotation matrix), noting that the proximal (upper-arm) calibration rotation matrix has been established at the previous stage (see previous section). Alternative 10 has the lowest error.
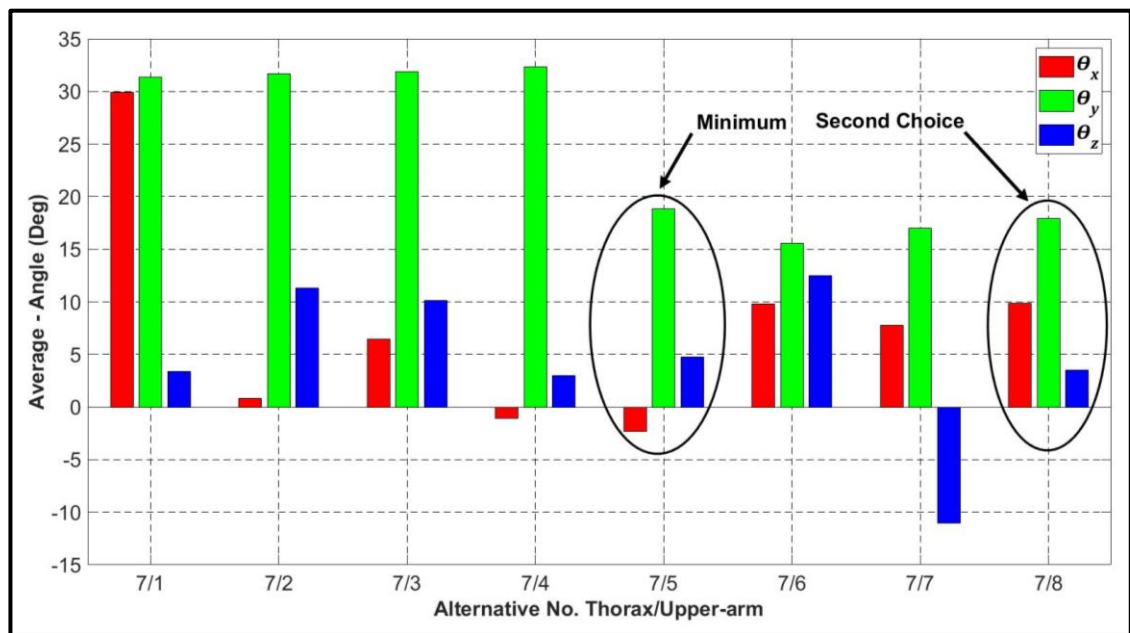

Figure 5.11: Error rotation vectors for the 10 alternative forearm calibration rotation matrices (used with alternative 8 for the upper-arm) for participant 1
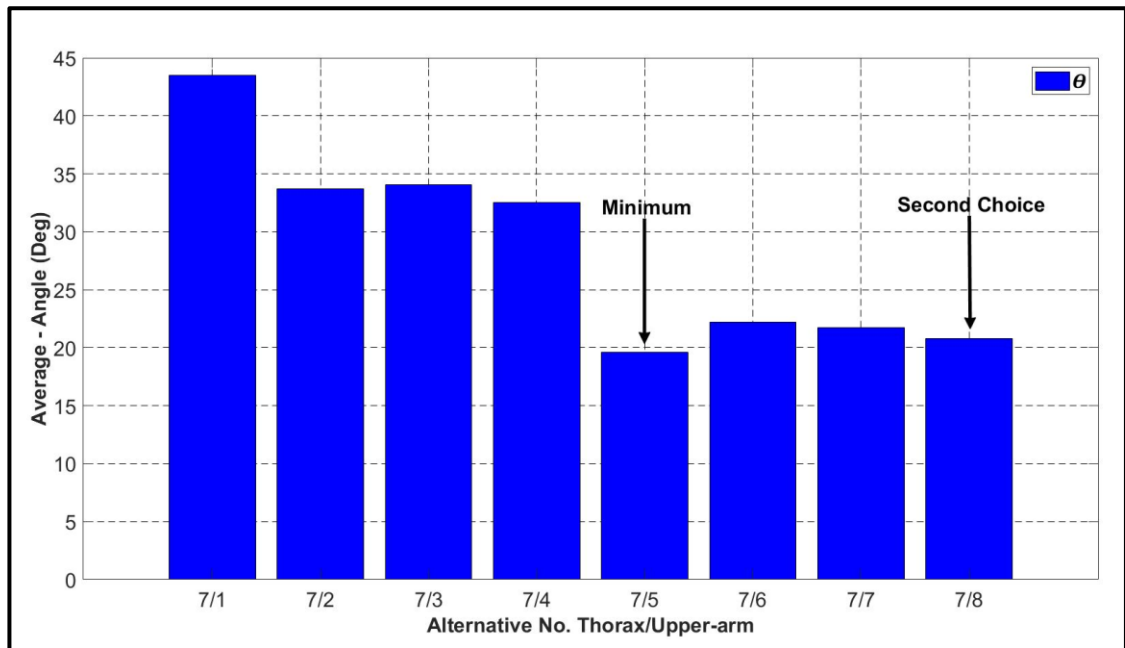
Figure 5.12: Magnitudes of the error rotation vectors for the 10 alternative forearm calibration rotation matrices (used with alternative 8 for the upper-arm) for participant 1

Table 5.3 shows the numerical error data for the best forearm calibration rotation matrix for all five participants (e.g. alternative 10 for participant 1, used with alternative 8 for the upper-arm). This error rotation vector can be used to provide a graphical representation of the error between the MIMU derived joint orientation and the V3D joint orientation. One example is shown in Figure 5.13 – upper-arm alternative 8 and forearm alternative 10 for participant 1.

Considering column 3 of Table 5.3, there is insufficient agreement between participants, which is necessary if a majority vote on the best alternative is to have an acceptably low probability of occurring by chance. However, after looking at the average errors across all alternatives for all participants, a second choice for participant 5 was identified, which increased the error by 18% (about 5°). This leads to agreement between 3 out of 5 participants and the probability of this occurring by chance alone is around 8% (see Appendix 2).

Table 5.3: Error rotation vectors for the elbow joint

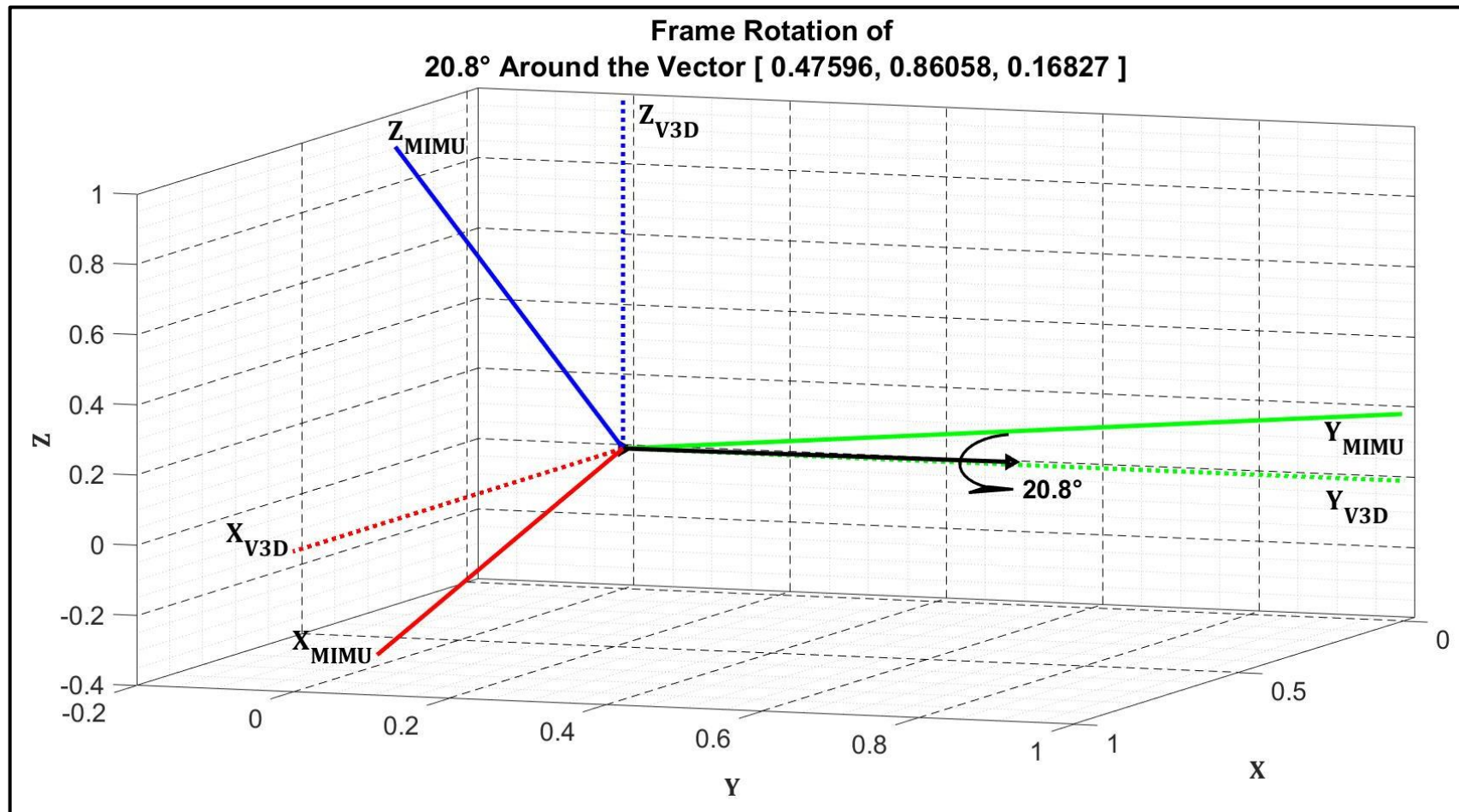| Elbow Joint						
	Upper-arm	**Forearm**	**Rotation vector components**			**Magnitude**
Participant	Alternative	Alternative	θ_x	θ_y	θ_z	θ
1	8	10	17.9º	-3.3º	-0.5º	18.2º
2	8	2	11º	-16.5º	9.8º	22.1º
3	8	6	16.6º	-4.1º	1.2º	17.1º
4	6	10	12.5º	-13º	6.3º	19.1º
5	8	4 *or 10 (18%)*	23.6º *or 14.2º*	19.2º *or -29.9º*	-5º *or -15.6º*	30.8º *or 36.5º*

Figure 5.13 : The elbow error rotation vector for participant 1, which is a graphical representation of the average error between MIMU joint orientation and V3D joint orientation. The axis-angle description is shown graphically by the black arrow showing the unique axis and angle of rotation.

5.3.4 Wrist

The error rotation vectors between each alternative MIMU sequence and the gold standard (V3D) sequence for the wrist and for participant 1 are presented in Figures 5.14 and 5.15. The magnitude (absolute angle) of the error rotation vector was used to select the best alternative (best hand calibration rotation matrix), noting that the proximal (forearm) calibration rotation matrix has been established at the previous stage (see previous section). Alternative 3 has the lowest error.
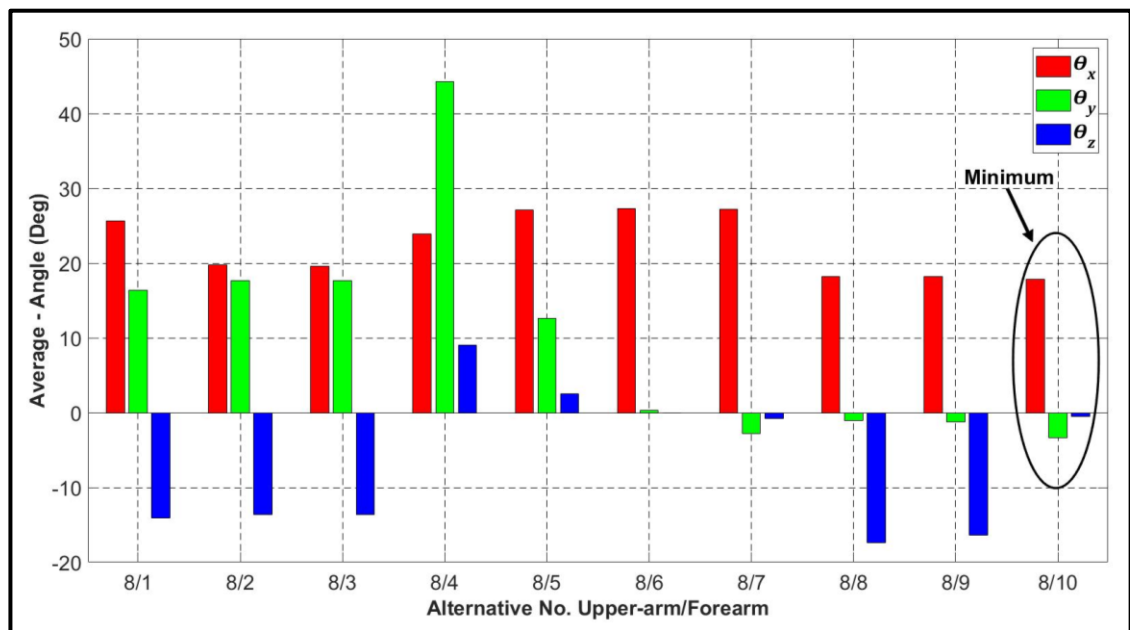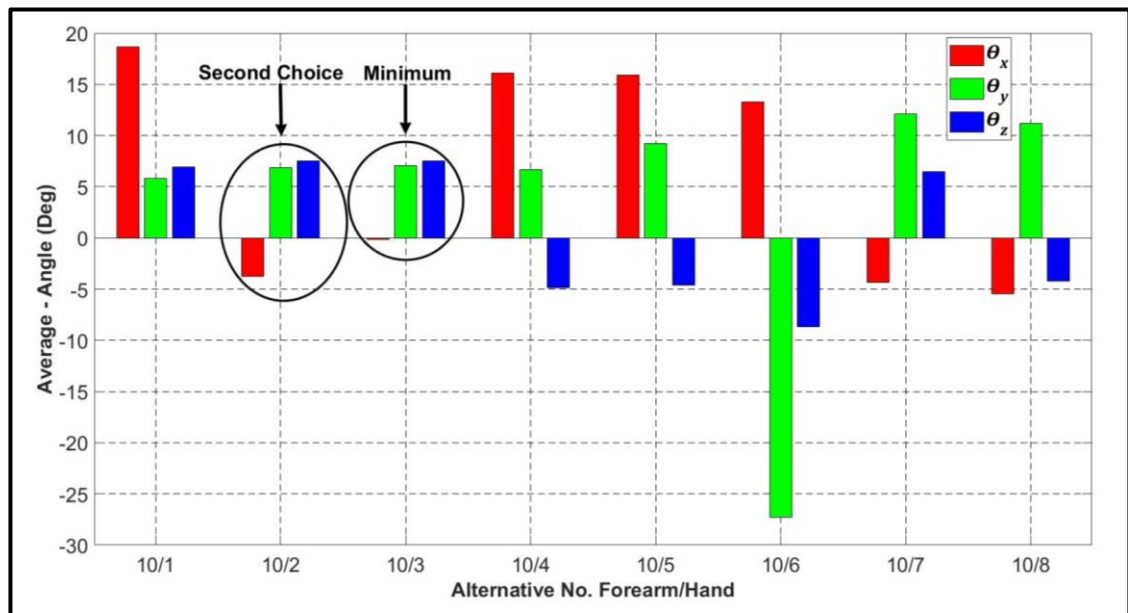

Figure 5.14: Error rotation vectors for the 8 alternative hand calibration rotation matrices (used with alternative 10 for the forearm) for participant 1
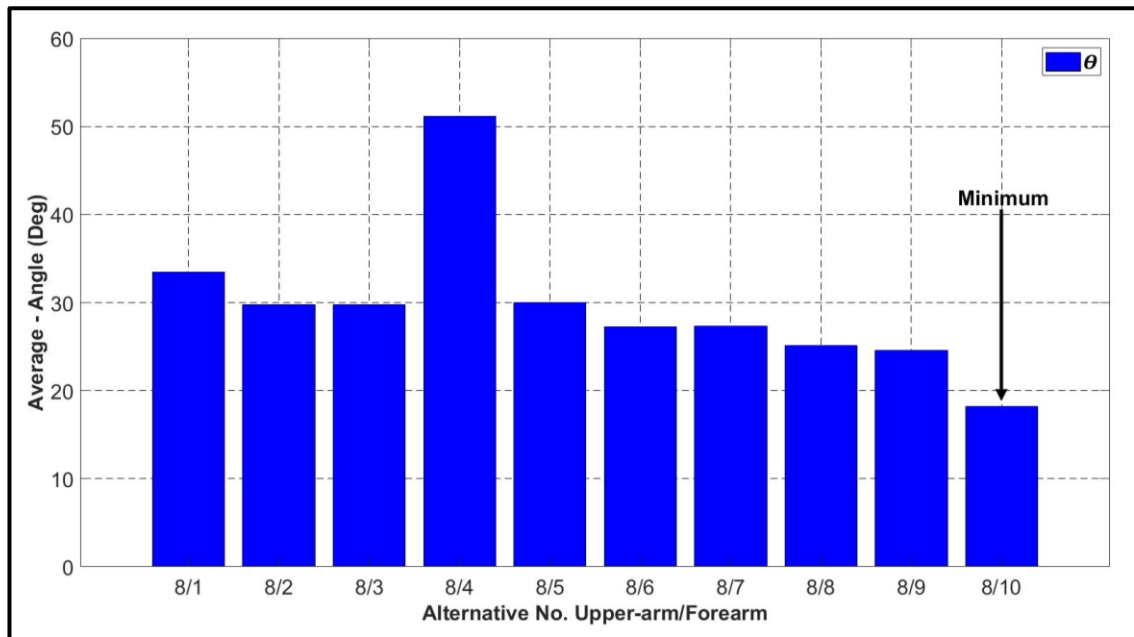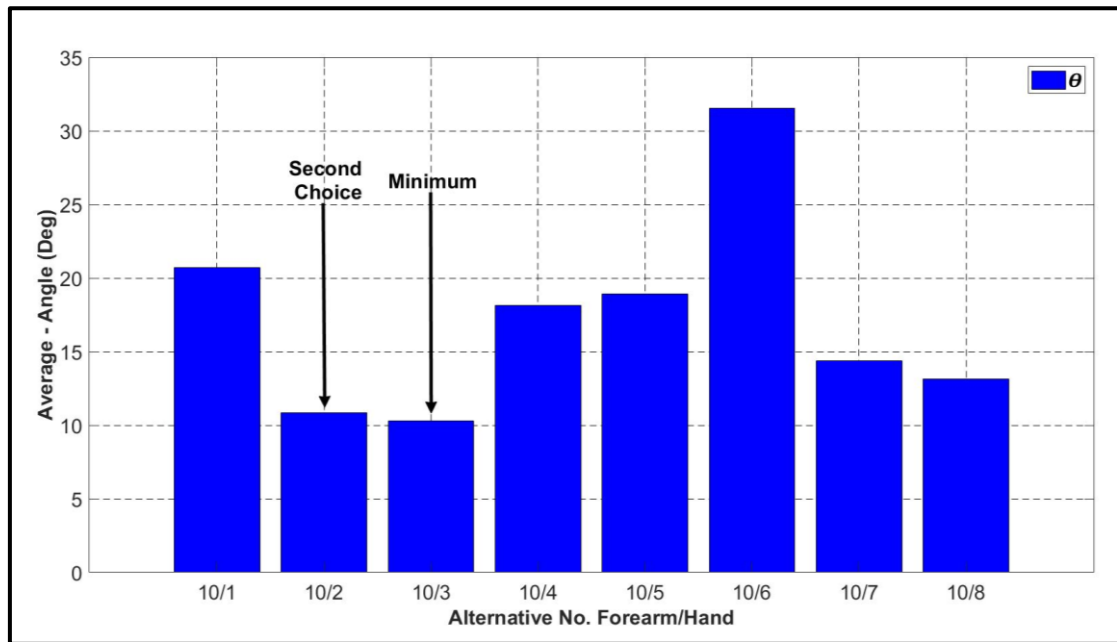
Figure 5.15: Magnitude of the error rotation vectors for the 8 alternative hand calibration rotation matrices (used with alternative 10 for the forearm) for participant 1

Table 5.4 shows the numerical error data for the best hand calibration rotation matrix for all five participants (e.g. alternative 3 for participant 1, used with alternative 10 for the forearm). This error rotation vector can be used to provide a graphical representation of the error between the MIMU derived joint orientation and the V3D joint orientation. One example is shown in Figure 5.16 – forearm alternative 10 and hand alternative 2 for participant 1.

Considering column 3 of Table 5.4, there is insufficient agreement between participants, which is necessary if a majority vote on the best alternative is to have an acceptably low probability of occurring by chance. However, after looking at the average errors across all alternatives for all participants, a good second choice for participant 1 was identified, which only increased the error by 6% (0.6°). This leads to agreement between 3 out of 5 participants and the probability of this occurring by chance alone is around 12% (see Appendix 2).

Table 5.4: Error rotation vectors for the wrist joint

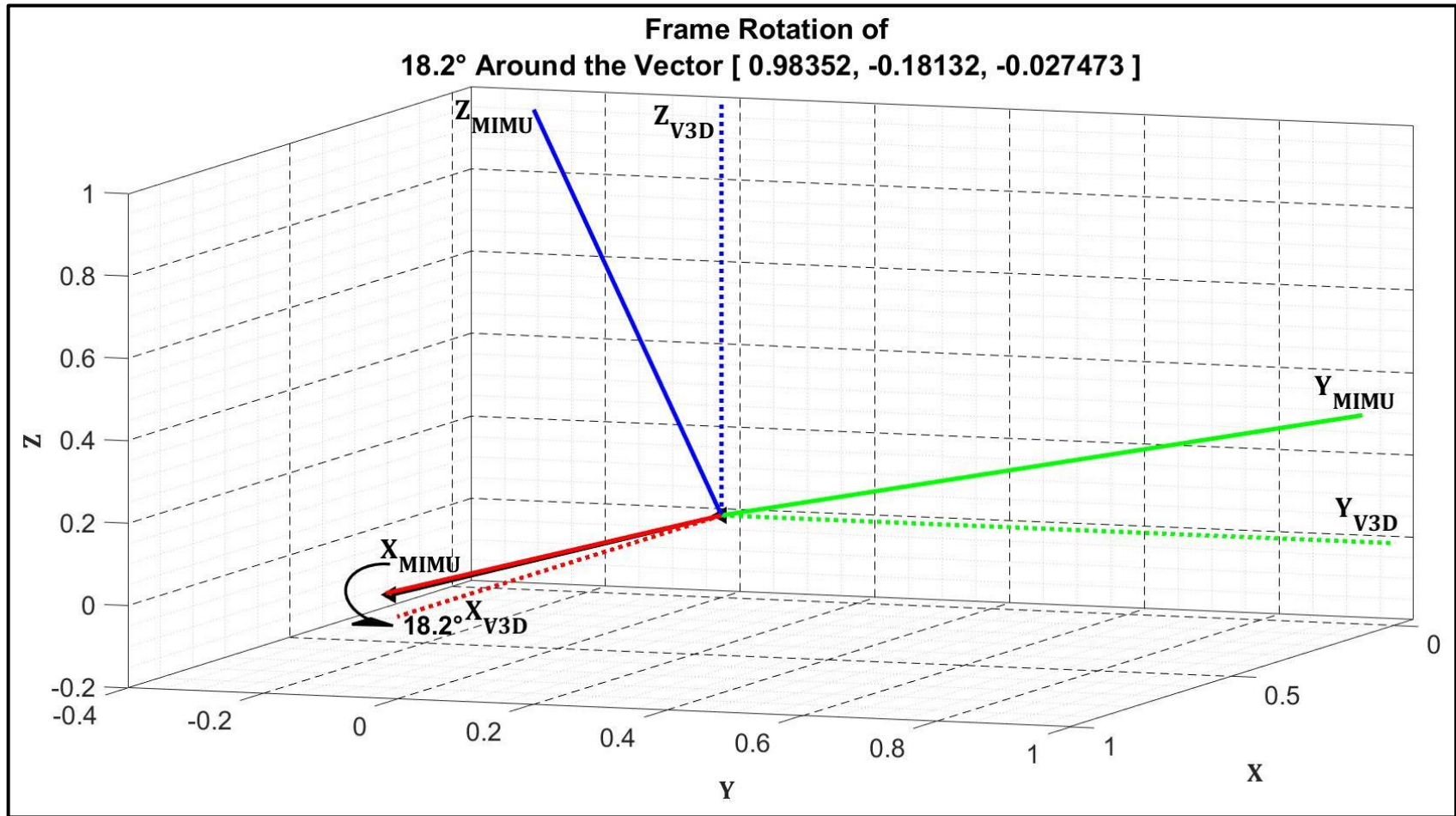|			Wrist Joint			
	Forearm	**Hand**	**Rotation vector components**			**Magnitude**
Participant	Alternative	Alternative	$\boldsymbol{\theta_x}$	$\boldsymbol{\theta_y}$	$\boldsymbol{\theta_z}$	$\boldsymbol{\theta}$
1	10	3 or 2 (6%)	-0.2º or -3.7º	7º or 6.9º	7.5º or 7.5º	10.3º or 10.9º
2	2	6	22.9º	-5.7º	11.2º	26.1º
3	6	2	-3.6º	8.5º	17.6º	19.9º
4	10	2	10.5º	-17.9º	7.7º	22.1º
5	10	6	14º	19.7º	23.1º	33.4º

Figure 5.16: The wrist error rotation vector for participant 1, which is a graphical representation of the average error between MIMU joint orientation and V3D joint orientation. The axis-angle description is shown graphically by the black arrow showing the unique axis and angle of rotation

127

5.4 Independent assessment of alternative calibration methods

In this section, for each joint, the best pair of calibration rotation matrices (for the proximal and distal segments) is found in an independent manner. In other words, the assessment process is not sequential and the results for each joint do not depend on any other joints. For example, for the shoulder, there are 8 calibration alternatives for the thorax and 8 for the upper-arm, leading to 64 combinations (pairs). Table 5.5 shows the number of calibration alternatives and hence combinations (pairs) for each joint.

Table 5.5: Number of alternative calibration rotation matrices and, hence, the number of combinations (pairs) for each joint

Joint	Proximal segment	Distal segment	Combinations
Lab-thorax	Not applicable	8	8
Shoulder	8	8	8×8=64
Elbow	8	10	8×10=80
Wrist	10	8	10×8=80

Therefore, the calibration alternatives are optimised for each joint. However, there is no guarantee that the two calibration rotation matrices selected for a particular body segment (i.e. for the joints that are proximal and distal to it) will be the same.

In the case of the lab-thorax pseudo joint, there is no proximal calibration rotation matrix because the proximal frame is the lab frame, not an anatomical frame. Therefore, the results presented in Table 5.1 apply. The following sections present the independent assessment results for the shoulder, elbow and wrist.

5.4.1 Shoulder

In the case of the shoulder, there are 8 alternative calibration rotation matrices for the proximal segment (thorax) and 8 alternatives for the distal segment (upper-arm). Therefore, the error rotation vectors for 64 alternative combinations (pairs) were compared over 4 functional tasks, each repeated 4 times, to find the best pair for each participant (see Table 5.6).

For example, for participant 1, Figures 5.17 and 5.18 show the error rotation vectors for the 64 alternative pairs of calibration rotation matrices. The best pair, with the smallest magnitude of error rotation vector (absolute angle), was combination 39 (alternative 5 for upper-arm and alternative 7 for thorax). As before, the error rotation vector can be used to provide a graphical representation of the error between the MIMU derived joint orientation and the V3D joint orientation (Figure 5.19).

Table 5.6: Error rotation vectors for the shoulder joint

Shoulder Joint						
	Thorax	**Upper-arm**	**Rotation vector components**			**Magnitude**
Participant	Alternative	Alternative	θ_x	θ_y	θ_z	θ
1	7	5	-2.3º	18.9º	4.8º	19.6º
2	8	8	7.2º	4.2º	-2.7º	8.8º
3	1	8	2º	-13.5º	-12.7º	18.6º
4	1	3	14.1º	-1.1º	9.5º	17º
5	8	8	-0.7º	-4.5º	-0.6º	4.6º

Figure 5.17: 64 error rotation vectors for the shoulder joint for participant 1 – combination 39 has the minimum error. The distal and proximal segments' alternatives are given by $D_{Alt} = round\ up\left(\frac{n}{8}\right)$ and $P_{Alt} = n - ((D_{Alt} - 1) \times 8)$, where n is the combination.

Figure 5.18: 64 error rotation vector magnitudes (absolute angles) for the shoulder joint for participant 1 – combination 39 has the minimum error. The distal and proximal segments' alternatives are given by $D_{Alt} = round\ up\left(\frac{n}{8}\right)$ and $P_{Alt} = n - ((D_{Alt} - 1) \times 8)$, where n is the combination.

132

Figure 5.19: The shoulder error rotation vector for participant 1, which is a graphical representation of the average error between MIMU joint orientation and V3D joint orientation. The axis-angle description is shown graphically by the black arrow showing the unique axis and angle of rotation.

5.4.2 Elbow

In the case of the elbow, there are 8 alternative calibration rotation matrices for the proximal segment (upper-arm) and 10 alternatives for the distal segment (forearm). Therefore, the error rotation vectors for 80 alternative combinations (pairs) were compared over 4 functional tasks, each repeated 4 times, to find the best pair for each participant (see Table 5.7).

For example, for participant 1, Figures 5.20 and 5.21 show the error rotation vectors for the 80 alternative pairs of calibration rotation matrices. The best pair, with the smallest magnitude of error rotation vector (absolute angle), was combination 79 (alternative 10 for forearm and alternative 7 for upper-arm). As before, the error rotation vector can be used to provide a graphical representation of the error between the MIMU derived joint orientation and the V3D joint orientation (Figure 5.22).

Table 5.7: Error rotation vectors for the elbow joint

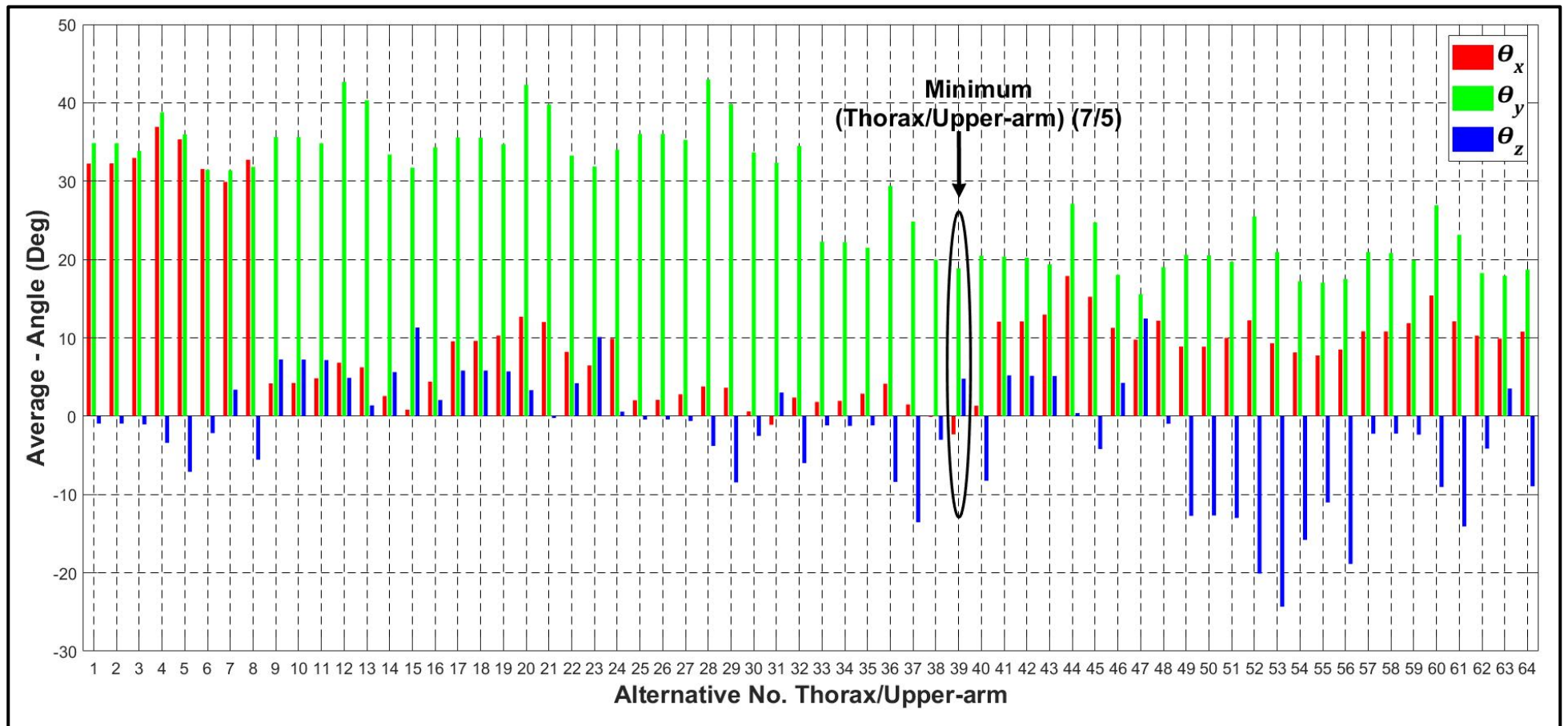| Elbow Joint						
	Upper-arm	Forearm	Rotation vector components			Magnitude
Participant	Alternative	Alternative	θ_x	θ_y	θ_z	θ
1	7	10	9.2º	-0.7º	1.1º	9.3º
2	5	2	17.9º	0.7º	5.3º	18.7º
3	7	6	10.1º	-4.4º	0.6º	11.1º
4	1	10	6.9º	-3.7º	-13.1º	15.3º
5	8	4	23.6º	19.2º	-5º	30.8º

Figure 5.20: 80 error rotation vectors for the elbow joint for participant 1 – alternative 79 has the minimum error. The distal and proximal

segments' alternatives are given by $D_{Alt} = round\ up\left(\frac{n}{8}\right)$ and $P_{Alt} = n - ((D_{Alt} - 1) \times 8)$, where n is the combination.

135

Figure 5.21: 80 error rotation vector magnitudes (absolute angles) for the elbow joint for participant 1 – alternative 79 has the minimum error. The distal and proximal segments' alternatives are given by $D_{Alt} = round\ up\left(\frac{n}{8}\right)$ and $P_{Alt} = n - ((D_{Alt} - 1) \times 8)$, where n is the combination.
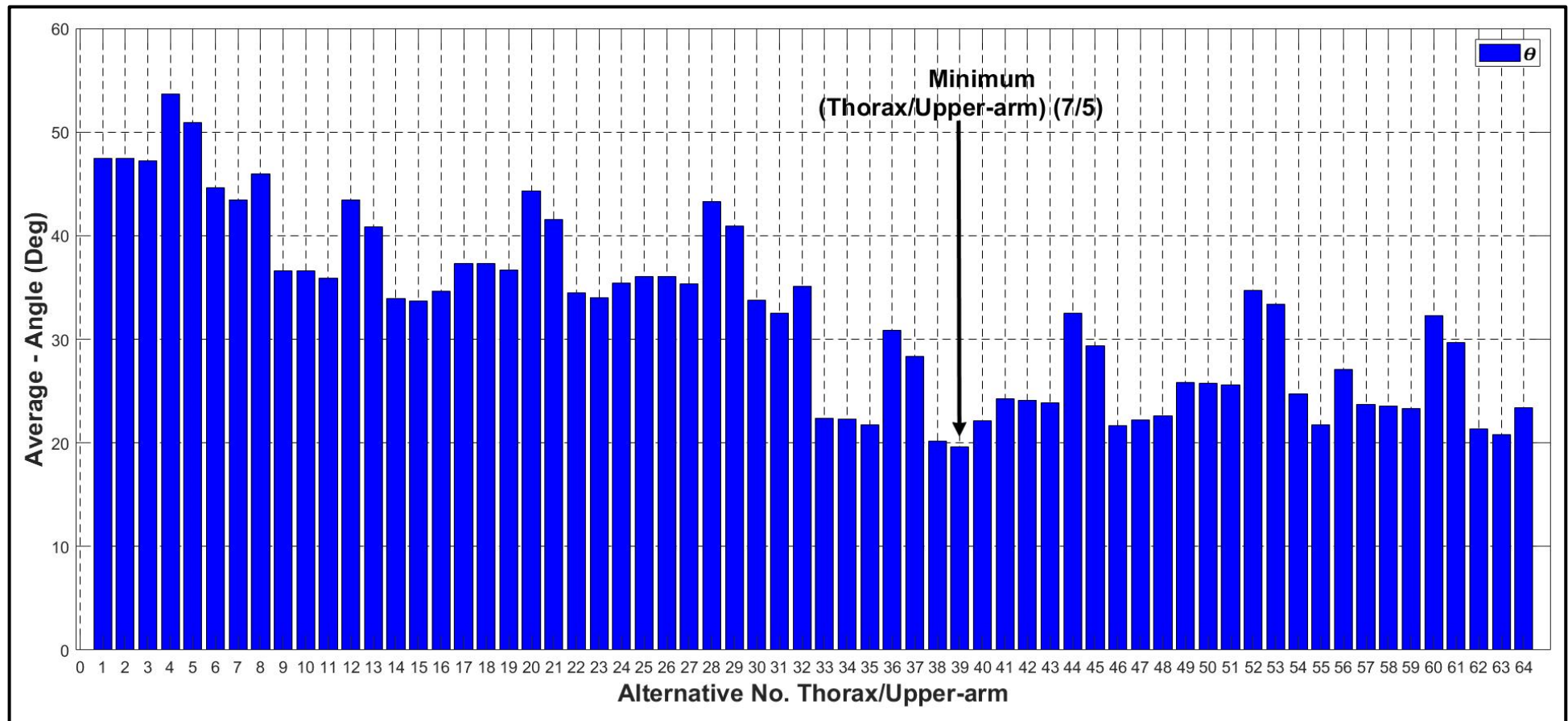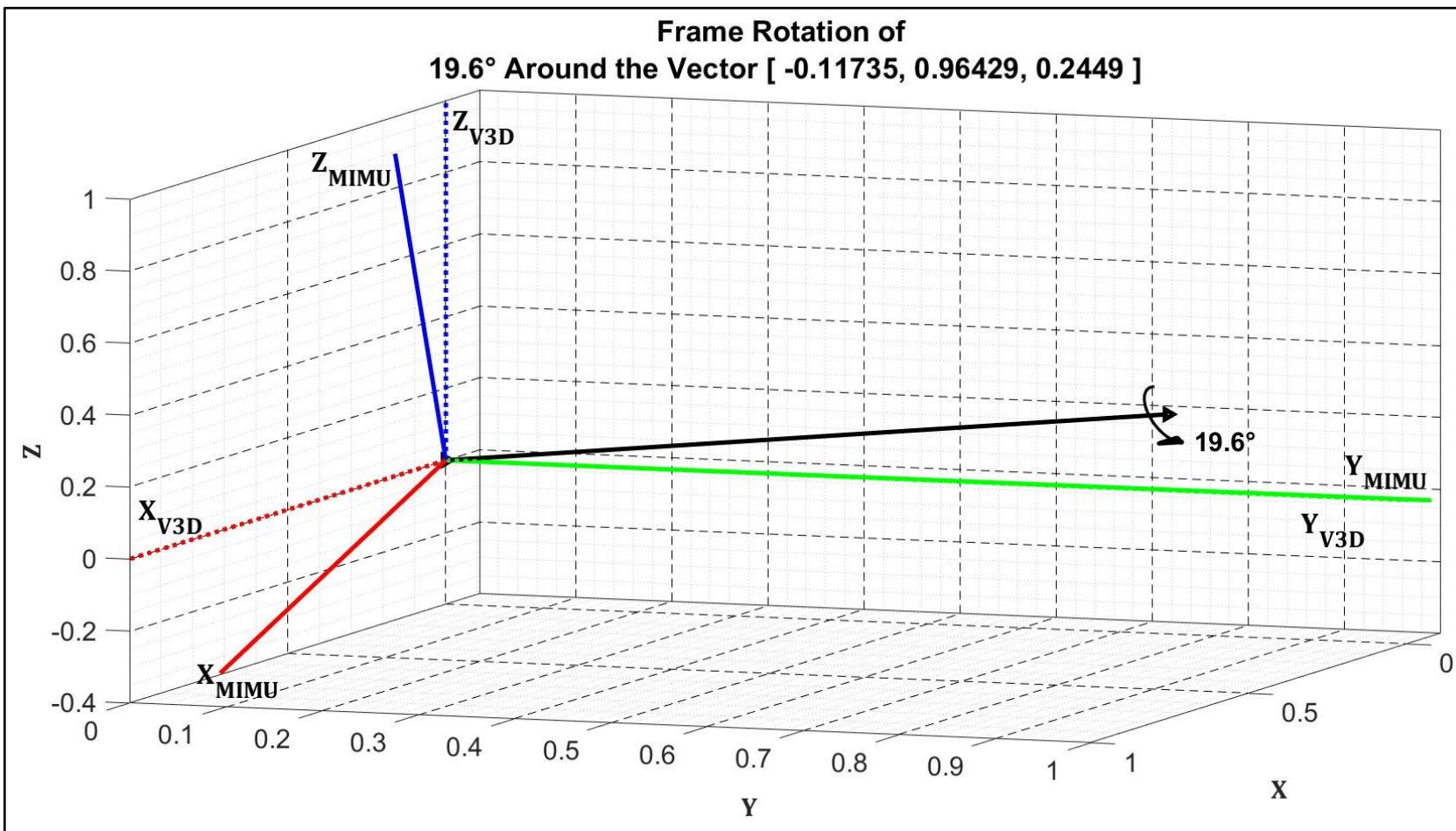
Figure 5.22: The elbow error rotation vector for participant 1, which is a graphical representation of the average error between MIMU joint orientation and V3D joint orientation. The axis-angle description is shown graphically by the black arrow showing the unique axis and angle of rotation.

5.4.3 Wrist

In the case of the wrist, there are 10 alternative calibration rotation matrices for the proximal segment (forearm) and 8 alternatives for the distal segment (hand). Therefore, the error rotation vectors for 80 alternative combinations (pairs) were compared over 4 functional tasks, each repeated 4 times, to find the best pair for each participant (see Table 5.8).

For example, for participant 1, Figures 5.23 and 5.24 show the error rotation vectors for the 80 alternative pairs of calibration rotation matrices. The best pair, with the smallest magnitude of error rotation vector (absolute angle), was combination 30 (alternative 3 for hand and 10 for forearm). As before, the error rotation vector can be used to provide a graphical representation of the error between the MIMU derived joint orientation and the V3D joint orientation (Figure 5.25).

Table 5.8: Error rotation vectors for the wrist joint

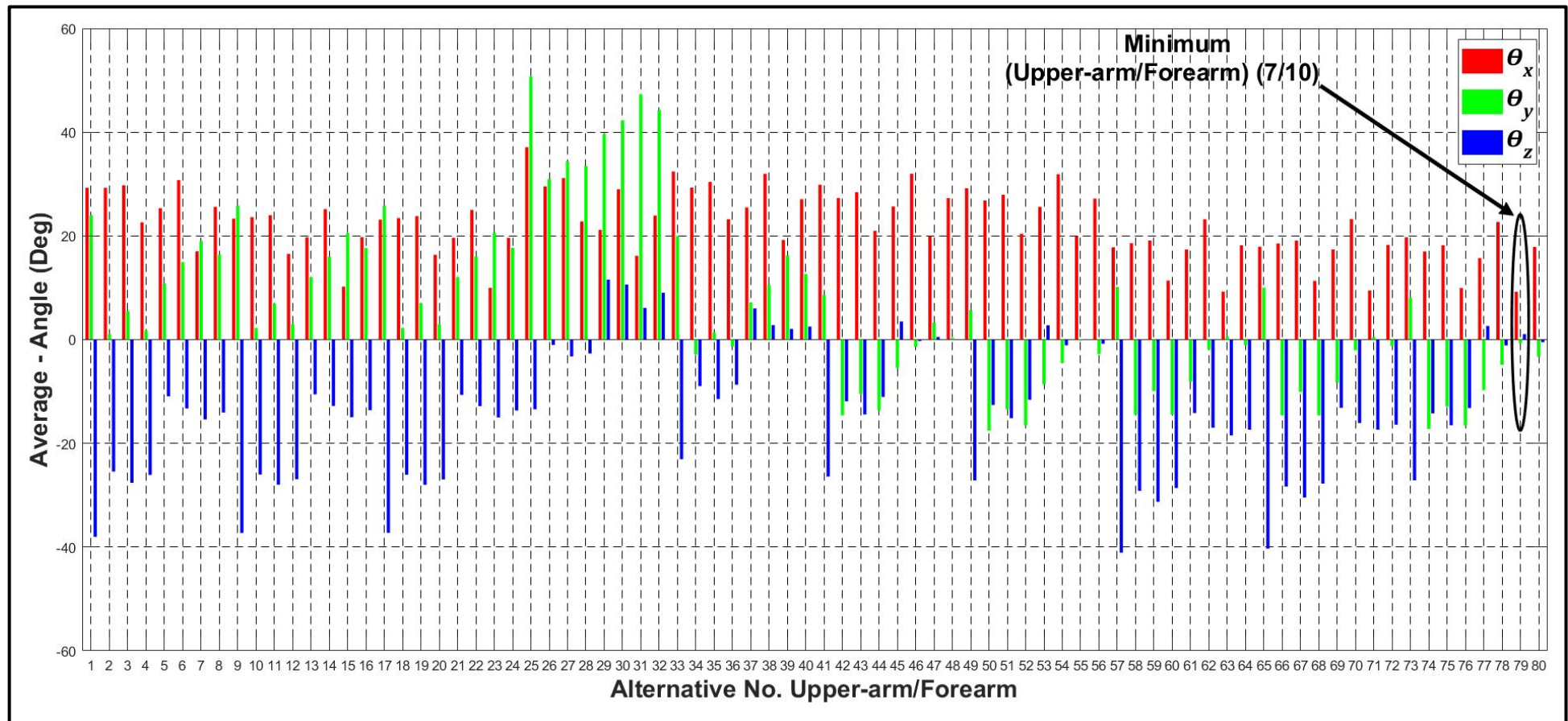| Wrist Joint						
	Forearm	**Hand**	**Rotation vector components**			**Magnitude**
Participant	Alternative	Alternative	θ_x	θ_y	θ_z	θ
1	10	3	-0.2º	7º	7.5º	10.3º
2	10	6	12.4º	9.7º	8.5º	17.9º
3	5	7	3.6º	-1.1º	10.7º	11.3º
4	5	2	5.2º	-5.3º	-0.3º	7.5º
5	4	7	5.9º	-9.1º	15º	18.5º

Figure 5.23: 80 error rotation vectors for the wrist joint for participant 1 – alternative 30 has the minimum error. The distal and proximal segments' alternatives are given by $D_{Alt} = round\ up\left(\frac{n}{10}\right)$ and $P_{Alt} = n - ((D_{Alt} - 1) \times 10)$, where n is the combination.
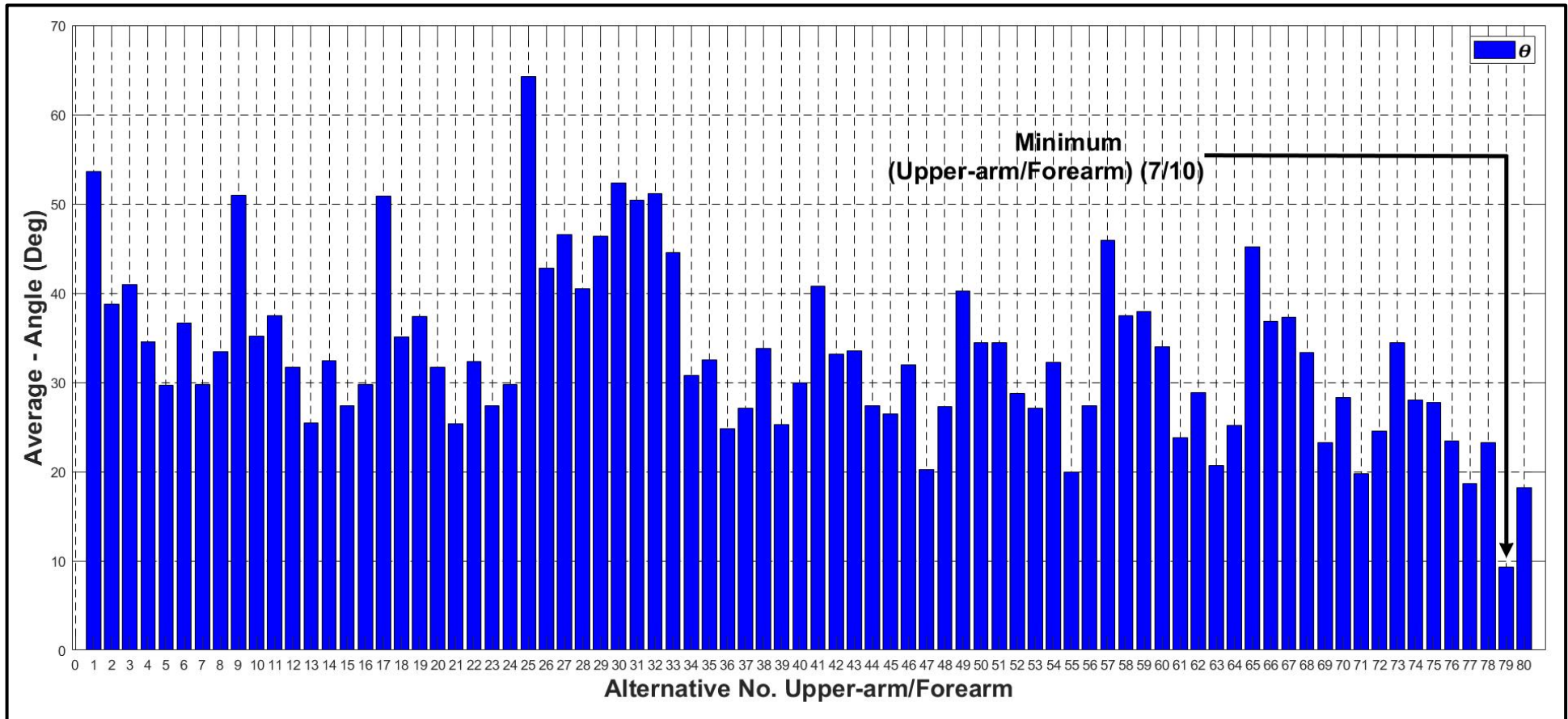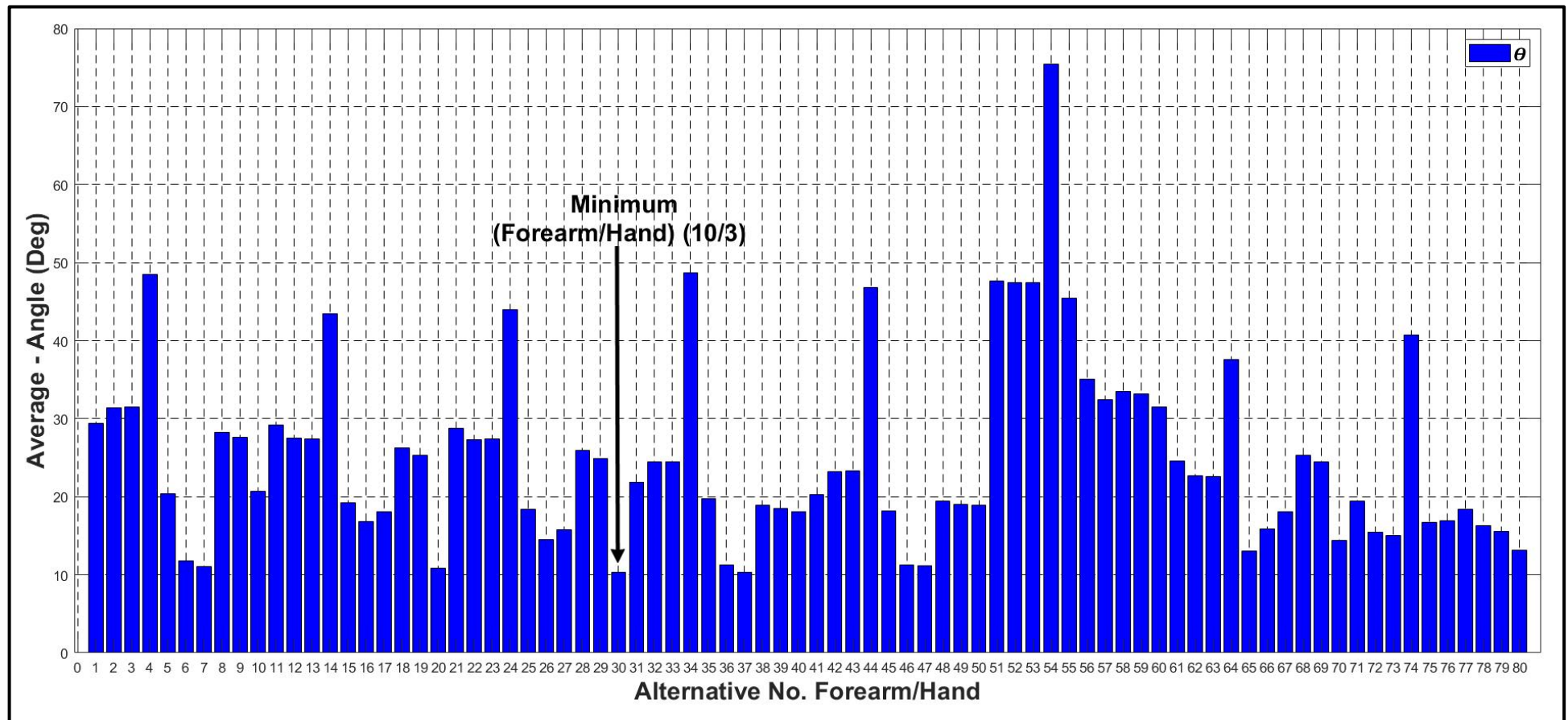
Figure 5.24: 80 error rotation vector magnitudes (absolute angles) for the wrist joint for participant 1 – alternative 30 has the minimum error. The distal and proximal segments' alternatives are given by $D_{Alt} = round\ up\left(\frac{n}{10}\right)$ and $P_{Alt} = n - ((D_{Alt} - 1) \times 10)$, where n is the combination.
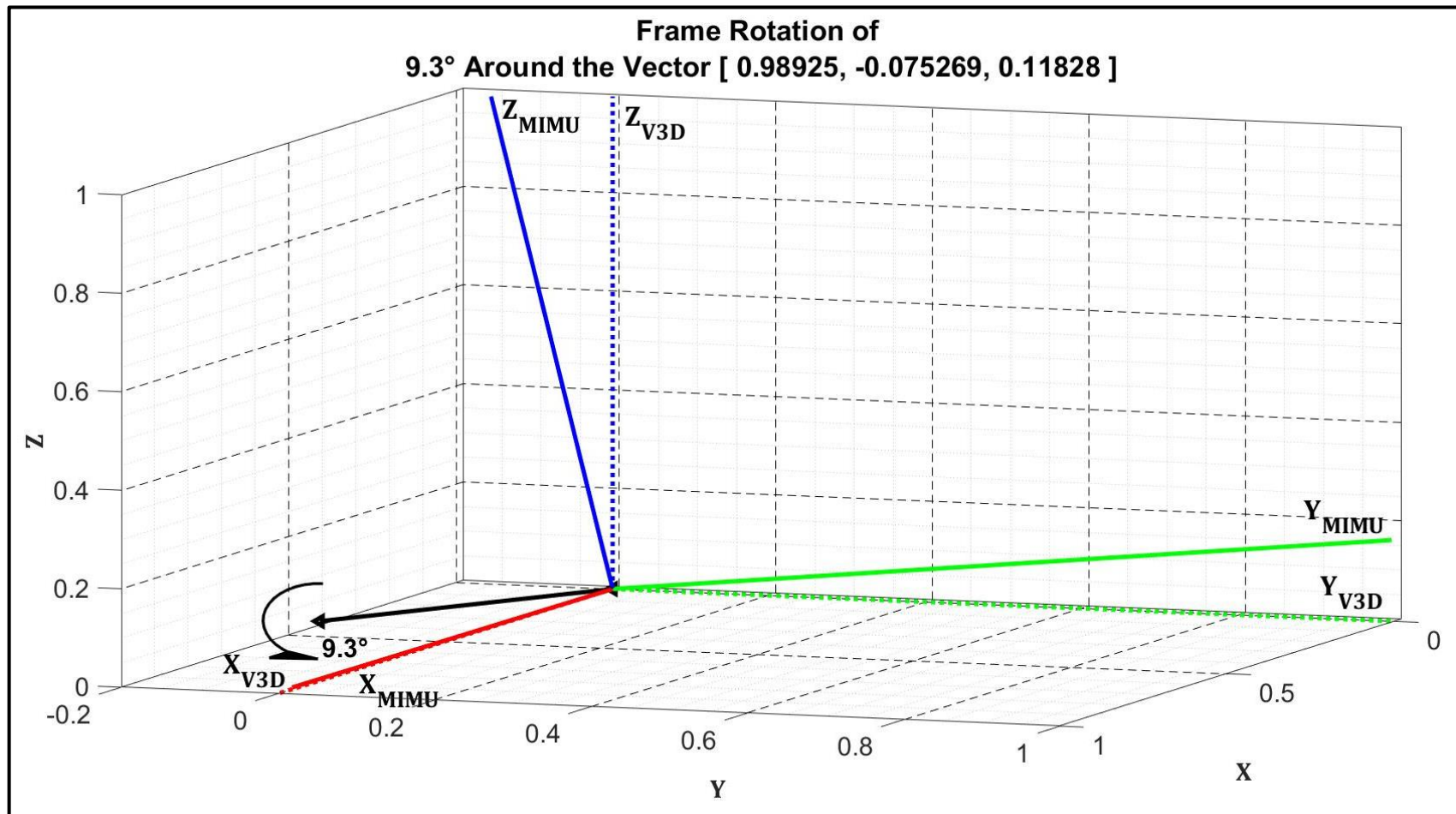
140
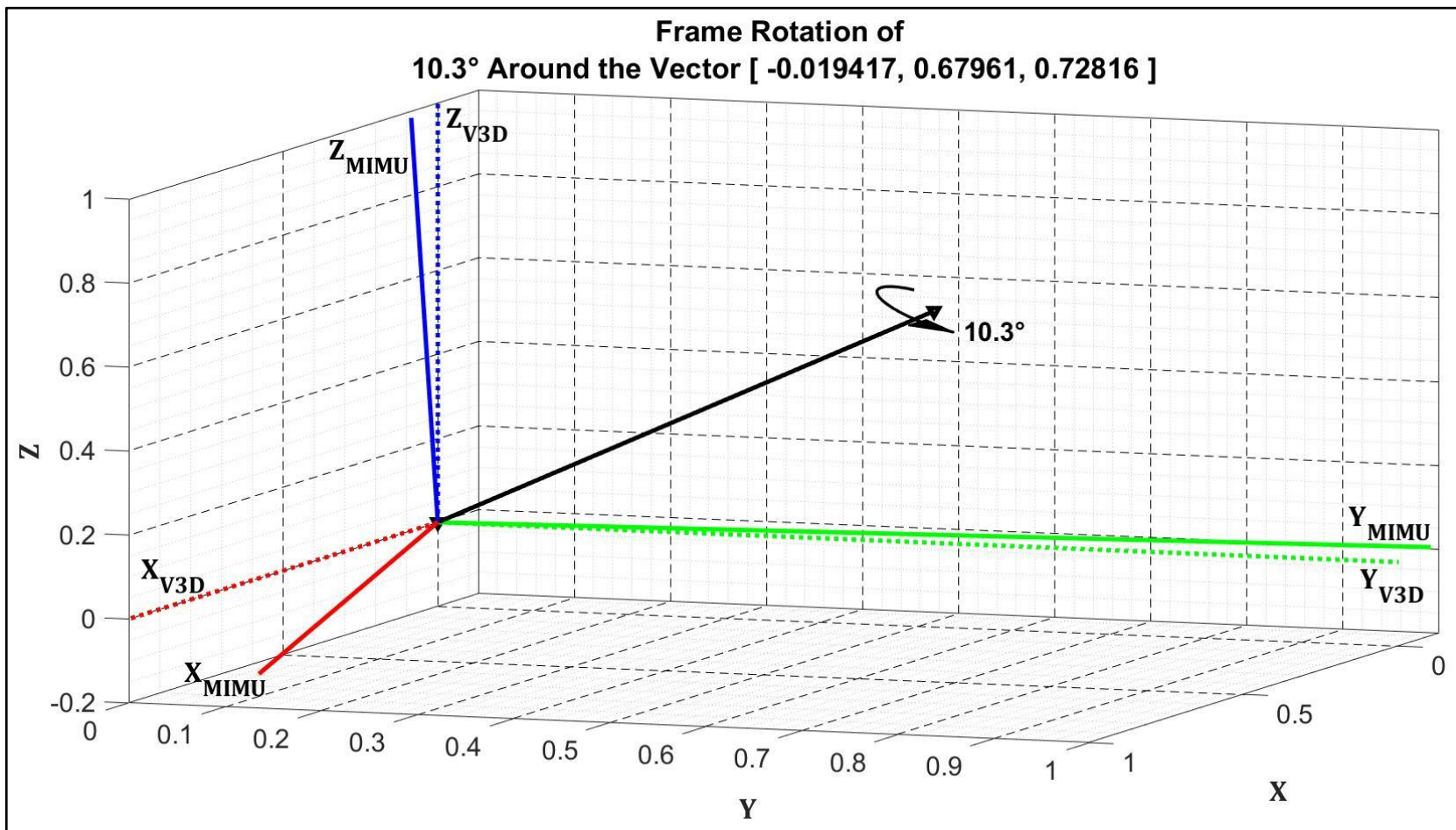
Figure 5.25: The wrist error rotation vector for participant 1, which is a graphical representation of the average error between MIMU joint orientation and V3D joint orientation. The axis-angle description is shown graphically by the black arrow showing the unique axis and angle of rotation.

5.5 Conclusions

This chapter has compared the alternative calibration methods described in Chapter 4. This has been done in three different ways, reported in sections 5.2, 5.3 and 5.4 respectively. Firstly, the alternative calibration rotation matrices listed in Tables 4.1 to 4.4 (for thorax, upper-arm, forearm and hand respectively) are compared by considering the orientations of the corresponding sensor (MIMU) defined anatomical frames (one for each calibration rotation matrix). The results are shown in Figures 5.1 to 5.4 for thorax, upper-arm, forearm and hand respectively; and these show that there is considerable variation between these sensors defined anatomical frames. This confirmed the need for the comprehensive comparisons reported in sections 5.3 and 5.4.

Secondly, for each joint, the best pair of calibration rotation matrices (i.e. for proximal and distal segments) was found using a sequential assessment process. This was done as a way to ensure that only one calibration method was required for each body segment. In other words, for a given body segment, to ensure that the same calibration rotation matrix is used in the calculation of both proximal and distal joint orientations.

Finally, for each joint, the best pair of calibration rotation matrices was found using an independent assessment process. Although this may lead to more accurate joint orientation results, there is no guarantee that the two calibration rotation matrices selected for a particular body segment (i.e. for the joints that are proximal and distal to it) will be the same.

The results from both sequential and independent assessment processes are summarised in Table 5.9. Comparing the results from the two assessment methods for a given participant, it is clear that there is a trade-off between minimising the number of calibration trials, which the sequential method does by using only one calibration matrix per segment, and maximizing accuracy, which the independent method does by finding optimum pairs of calibration rotation matrices for each joint. However, there are some common results across the two methods. Further work, based on the independent assessment method, could

consider lower ranked alternatives as well as the optimum alternatives, which may show greater agreement between the two methods.

Comparing the results from the two assessment methods across participants it is clear that, regardless of which assessment method is adopted, there is no one set of solutions that is optimal across participants. This could be considered a negative result, indicating that there is no one calibration approach that suits all participants. However, as mentioned above, further work could consider lower ranked alternatives as well as the optimum alternatives, which may show greater agreement between the results for different participants.

Nevertheless, it is possible to draw tentative conclusions from Table 5.9 with regard to recommendations for a set of calibration rotation matrices and the associated calibration methods. These are based only on the results for the sequential method to ensure that each segment only needs one calibration rotation matrix, which is used for both its proximal and distal joints. This minimises the number of calibration movements required. Then, based on the maximum agreement between participants, the results summarised in the top half of Table 5.9 lead to the following recommendations:

Thorax – Use calibration rotation matrix 7. This requires the following calibration movements: flexion-extension of the thorax (forward-backward lean), including the static position (thorax straight and upright).

Upper-arm – Use calibration rotation matrix 8. This requires the following calibration movements: shoulder flexion-extension; and shoulder internal-external rotation.

Forearm – Use calibration rotation matrix 10. This requires the following calibration movements: shoulder internal-external rotation; and forearm pronation-supination.

Hand – Use calibration rotation matrix 2. This requires the following calibration movements: wrist flexion-extension; and radial-ulnar deviation.

Table 5.9: Summary of best calibration methods

Sequential assessment							
Participant	Lab-Thorax Joint	Shoulder Joint		Elbow Joint		Wrist Joint	
	Thorax	Thorax	Upper-arm	Upper-arm	Forearm	Forearm	Hand
P1	7	7	8	8	10	10	2
P2	4	4	8	8	2	2	6
P3	7	7	8	8	6	6	2
P4	7	7	6	6	10	10	2
P5	1	1	8	8	10	10	6
Independent assessment							
Participant	Lab-Thorax Joint	Shoulder Joint		Elbow Joint		Wrist Joint	
	Thorax	Thorax	Upper-arm	Upper-arm	Forearm	Forearm	Hand
P1	7	7	5	7	10	10	3
P2	4	8	8	5	2	10	6
P3	7	1	8	7	6	5	7
P4	1	1	3	1	10	5	2
P5	1	8	8	8	4	4	7

Chapter 6 – Discussion and Conclusions

6.1 Summary

Around 50% of stroke survivors suffer as a result of losing significant upper-limb control. This can cause a remarkably negative impact on activities of daily living (ADLs) and hence quality of life (Barker et al., 2008). Upper-limb impairments may typically include: Reductions in muscle activations; inability to extend the shoulder, elbow, and wrist joints; and impaired coordination between upper-limb segments (Barker et al., 2008; Burgar et al., 2011; Harris & Eng, 2010; Timmermans et al., 2009). There are a wide range of different rehabilitation interventions, which all aim to promote upper limb recovery after stroke. These interventions include conventional physiotherapy, robot assisted therapy, and FES assisted therapy. Studies of FES assisted therapy have shown promising results in restoring reaching and grasping function.

However, the problem with existing FES systems is that they are: either too simple and inflexible to allow bespoke upper-limb therapy to be set up for each patient; or they require specialist skills to set up and therefore require clinical engineering involvement for each patient. To overcome this limitation, the Salford team have produced a flexible upper-limb FES system, which enables therapists to setup patient and task-specific finite state machine (FSM) controllers (Smith et al., 2017, 2019; Sun et al., 2016, 2018). Transitions conditions for moving from one state to another (i.e. between movement phases) are governed by user-defined rules, which use inputs from body-worn MIMUs (Sun, 2014).

However, the system limitations are as follows:

- Significant therapist input is still required to set up the state-machine controller and to adapt the controller as the patient's status changes;
- It uses individual MIMUs to provide segment orientations, but does not combine information from pairs of MIMUs on adjoining segments to give anatomical joint angles, which are more meaningful;

- The controller cannot automatically adapt the stimulation profiles as the patient changes (e.g. fatigues or improves their performance with practise).

This PhD has focussed on solving the second problem listed above: the estimation of anatomical joint angles using data from MIMUs on adjoining upper-limb segments. The solving of this problem would be of benefit to numerous other clinical applications, as well as the FES problem introduced above. For example, regular clinical assessments of rehabilitation progress are important and, ideally, these should be based on objective measurement of upper-limb and body movements during functional task practise in order to assess the effects of muscle weaknesses and coordination dysfunctions.

Using body segment orientations, rather than anatomical joint angles, allows users to compensate for muscle weaknesses and coordination dysfunctions by moving proximal segments to change the orientation of a more distal segment, without using their anatomical joints correctly as needed for good rehabilitation. This may also be associated with reduced patient effort to use their weaker muscles and hence reduced efficacy of the intervention. However, the MIMU orientation data cannot be interpreted anatomically, to give joint angles, unless the orientations of the MIMUs are known with respect to their corresponding segment anatomical coordinate frames. Therefore, for each body segment, anatomical calibration must be performed to obtain the relationships between each MIMU sensor coordinate frame and its corresponding anatomical coordinate frame.

6.1.1 Limitations with existing MIMU calibration studies

The anatomical calibration problem is still an open research question because no study has comprehensively compared alternative approaches to determine the best calibration method. In particular, no study has compared the many alternative methods of defining the two reference vectors (v_{ref1} and v_{ref2}). For this reason, a review and critical comparison was undertaken of the calibration methods used by other researchers in upper-limb applications to inform the author's work (summarised in Table 2.2, Chapter 2).

The anatomical calibration methods found were classified as involving one or more of the following: (1) anatomical alignment of sensors; (2) static measurements; or (3) dynamic measurements. Anatomical alignment involves aligning the sensor axes with anatomical axes defined by bony landmarks such as the styloid processes, humeral epicondyles, and humeral tubercle. Static measurements involve positioning the arm in a known posture and using the gravity vector (measured by the 3-axis accelerometer) to achieve anatomical calibration. Dynamic measurements involve moving a joint in a defined way and using the angular velocity vector (measured by the 3-axis rate-gyro) to achieve anatomical calibration.

No comparison of the alternatives has been found in the literature apart from that of (Bouvier et al., 2015), which did not cover all of the alternatives and only assessed accuracy and precision. (Bouvier et al., 2015) did not compare calibration methods in term of speed, and simplicity. Furthermore, they did not include thorax orientation with respect to the global (LAB) coordinate frame. In summary, no study has:

1) Included all segments of the upper-limb, and the thorax;

2) Compared all of the alternatives for defining the two reference vectors;

3) Made a comprehensive comparison covering accuracy, speed, and simplicity.

Therefore, the author has undertaken a comprehensive comparison of alternative calibration methods by comparing MIMUs derived joint kinematics with gold standard data derived from stereophotogrammetry.

6.1.2 Experimental data collection using synchronised stereophotogrammetry and MIMUs

To enable comparison of joint kinematics derived from multiple body worn MIMUs with equivalent gold standard data, synchronised data were collected from MIMUs (Xsens) and stereophotogrammetry (VICON multi-camera system). Five healthy volunteers with no history of right upper-limb complaints participated. The two systems were synchronised at 50 Hz and used to record upper-limb

movement trials. The camera data was exported to Visual 3D (V3D) and processed to derive sequences of joint rotation matrices for each movement trial, which were then exported to MATLAB to be compared with the corresponding MIMUs derived sequences of joint rotation matrices.

After static calibration of the VICON camera system, each participant performed two types of movement trials as follows:

1. Calibration movements consisting of uni-axial rotations, which were used to derive anatomical axes from angular velocity data. These movements also included systematic pauses in the motion, which were used to derive anatomical axes from gravity (accelerometer) data.

2. Four functional tasks, which were used to compare the MIMUs derived joint kinematics with camera system derived results (the gold standard).

All movement trials were repeated four times.

6.1.3 Deriving Joint Kinematics from MIMUs Data

Mathematical methods for processing MIMUs data have been presented. Firstly, anatomical calibration is discussed in section 4.2, including the basic principles and the alternative approaches that were compared for defining each body segment's anatomical coordinate frame. For each alternative, the mathematics for calculating the corresponding calibration rotation matrix has been summarised in Tables 4.1 to 4.4 for the thorax, upper-arm, forearm and hand respectively. Secondly, the derivation of joint rotation matrices and, hence, joint kinematics is discussed in section 4.3. This combines the sensor outputs (their orientations) and the calibration rotation matrices to obtain the orientations of the anatomical frames. Then the anatomical orientations of segments that are proximal and distal to a joint are used to calculate that joint's rotation matrix, from which other descriptions of the joint kinematics can be derived.

Finally, this chapter describes the difficulties encountered with the MIMU orientation estimators. In the first implementation of the methods described above, the orientation estimator (Kalman filter) provided by the supplier of the

MIMUs (Xsens) was used to obtain the sensor orientations relative to their common Sensor Global frame. However, following difficulties during the testing of the MATLAB code, it appeared that each sensor was referencing a different Sensor Global frame, rather than a common Sensor Global based on vertical and magnetic north. Whilst working to debug the corresponding MATLAB code, a new 2019 version of MATLAB was released, which included a MIMU toolbox with alternative orientation estimators that can work with the raw data from the Xsens MIMUs. Using one of the MATLAB estimators resolved the problem and the considerable effort already invested in finding a solution had been unnecessary.

6.1.4 Comparison of calibration methods

In Chapter 5, the alternative calibration methods described in Chapter 4 have been compared in three different ways. Firstly, the alternative calibration rotation matrices listed in Tables 4.1 to 4.4 (for thorax, upper-arm, forearm, and hand respectively) are compared by considering the orientations of the corresponding sensor (MIMU) defined anatomical frames (one for each calibration rotation matrix). The results show that there is considerable variation between the alternative sensor defined anatomical frames. This confirmed the need for comprehensive comparisons, which were undertaken using two assessment processes as follows:

1) Sequential assessment to ensure that that only one calibration rotation matrix was required for each body segment to minimise the number of calibration movements required.

2) Independent assessment, which may lead to more accurate joint orientation results, but there is no guarantee that the two calibration rotation matrices selected for a particular body segment (i.e. for the joints that are proximal and distal to it) will be the same.

Although the results were not conclusive, it is possible to draw tentative conclusions from the results, summarised in Table 5.9, with regard to recommendations for a set of calibration rotation matrices and the associated calibration methods. These are based only on the results for the sequential

method to ensure that each segment only needs one calibration rotation matrix, which is used for both its proximal and distal joints. This minimises the number of calibration movements required. Then, based on the maximum agreement between participants, the results summarised in the top half of Table 5.9 lead to the following recommendations:

Thorax – Use calibration rotation matrix 7. This requires the following calibration movements: flexion-extension of the thorax (forward-backward lean), including the static position (thorax straight and upright).

Upper-arm – Use calibration rotation matrix 8. This requires the following calibration movements: shoulder flexion-extension; and shoulder internal-external rotation.

Forearm – Use calibration rotation matrix 10. This requires the following calibration movements: shoulder internal-external rotation; and forearm pronation-supination.

Hand – Use calibration rotation matrix 2. This requires the following calibration movements: wrist flexion-extension; and radial-ulnar deviation.

6.2 Conclusions

1. While many papers have been published on sensor-to-segment calibration, there has been no comprehensive comparison of the alternative approaches to establish their relative merits. A recent, clinically focused review highlighted the difficulty faced by researchers in the absence of the systematic approach presented here (Poitras et al., 2019).

2. The results reported in this thesis demonstrate that there is considerable variation between the alternative sensor defined anatomical frames and, hence, confirm the need for comprehensive comparisons.

3. The comparisons reported in this thesis have led to the tentative recommendations summarised above in section 6.1.4.

4. Nevertheless, the methods reported are a sound foundation for future work to provide stronger recommendations, with formal measures of confidence.

6.3 Limitations and Future Work

The results presented in Chapter 5 have only led to tentative recommendations for the best set of calibration rotation matrices and the associated calibration methods. This is due to a number of limitations, the most critical of which are:

- Doubts about the quality of the experimental protocol because it was not recorded in sufficient detail. For example, the initialisation of the MIMUs and the time allowed for their orientation estimators to settle was not recorded in sufficient detail.
- The low number of participants.
- The limited nature of the analyses conducted thus far.
- Problems with some commercial MIMU real-time orientation estimators.

Therefore, in the first instance, future work should address these limitations.

Firstly, the experimental protocol should be revisited and, if it is felt necessary, improved before further experimental data is collected. Most importantly, the protocol should be recorded in sufficient detail for the experiments to be repeated with a high level of confidence that the protocol is always the same.

Secondly, to provide greater confidence in the conclusions, a larger number of participants should be recruited. With data from only 5 participants, any recommendations are often based on 3 from 5 judgements, which is insufficient to provide any worthwhile quantification of confidence. Therefore, the recommendations made here should be considered to be tentative.

Thirdly, although 5 participants seem insufficient, it may be that the confidence in the results could be increased with further analyses. In particular, further work could consider lower ranked alternatives as well as the optimum alternatives, which may show greater agreement between the results for different participants.

Finally, although the MATLAB orientation estimator (filter) that became available in 2019 led to usable MIMUs data, it is not a real-time filter embedded in a commercially available MIMU. Conversely, the commercial estimator that was

initially used (Xsens) led to many difficulties and, hence, a lack of trust in its accuracy. Therefore, it is important that a validated protocol is developed for testing MIMU real-time estimators. This should be done by a team that is independent of any commercial suppliers. The other future work suggested above should be preceded by testing of the MIMU real-time estimators using such a protocol.

6.4 Novel contributions

- The first comprehensive comparison of alternative calibration methods.
- Given the set of anatomical reference vectors, all possible derivations of the calibration matrices were compared.
- The average error rotation vector was used, which has been shown to be a robust method for averaging rotations (Sharf et al., 2010). Furthermore, its magnitude provides a single scalar for minimisation purposes.
- Overall, the methods developed provide a strong basis for future work, including for both upper-limb and lower-limb.

Appendix 1 – Derivation of the sensor marker frame for the four segments (thorax, upper-arm, forearm, and hand)

$$(^{LAB}R_{SM_T}, \, ^{LAB}R_{SM_U}, \, ^{LAB}R_{SM_F}, \, ^{LAB}R_{SM_H})$$

Thorax – $^{LAB}R_{SM_T}$

The markers (on the upper corners of the sensor) data has been used to calculate a new coordinate system called (**SM**) which nearly aligned with sensor inertial coordinate system (**SI**). For Thorax, four markers have been used to create **SM** as follows (Figure A1.1):

The mathematical equations:

$$X_{SM_T} = P_{\frac{1}{2}} - P_{\frac{3}{4}}$$

X_{SM_T}:

$$X_{SM_T}$$
$$= \left[\frac{x_{T1} + x_{T2} - x_{T3} - x_{T4}}{2}, \frac{y_{T1} + y_{T2} - y_{T3} - y_{T4}}{2}, \frac{z_{T1} + z_{T2} - z_{T3} - z_{T4}}{2} \right],$$

$$X_{SM_T} = \frac{X_{SM_T}}{|X_{SM_T}|}$$

$$\widetilde{Y}_{SM_T} = P_{\frac{1}{3}} - P_{\frac{2}{4}}$$

$\widetilde{Y}_{SM_T}$:

$$\widetilde{Y}_{SM_T}$$
$$= \left[\frac{x_{T1} + x_{T3} - x_{T2} - x_{T4}}{2}, \frac{y_{T1} + y_{T3} - y_{T2} - y_{T4}}{2}, \frac{z_{T1} + z_{T3} - z_{T2} - z_{T4}}{2} \right],$$

$$\widetilde{Y}_{SM_T} = \frac{\widetilde{Y}_{SM_T}}{|\widetilde{Y}_{SM_T}|}$$

Z_{SM_T}:

$$Z_{SM_T} = \frac{X_{SM_T} \times \widetilde{Y}_{SM_T}}{|X_{SM_T} \times \widetilde{Y}_{SM_T}|}, \, Y_{SM_T} = Z_{SM_T} \times X_{SM_T}$$

$$\mathbf{X_{A_T}} = \mathbf{Z_{SM_T}}$$

$$\mathbf{Y_{A_T}} = \mathbf{X_{SM_T}}$$

$$\mathbf{Z_{A_T}} = \mathbf{Y_{SM_T}}$$

$$^{LAB}\mathbf{R}_{SM_T} = \begin{bmatrix} \mathbf{X_{SM_T}} & \mathbf{Y_{SM_T}} & \mathbf{Z_{SM_T}} \end{bmatrix}$$

$\mathbf{X_{SM_T}}$, $\mathbf{Y_{SM_T}}$, $\mathbf{Z_{SM_T}}$ are a new coordinate system aligned with sensor inertial coordinate system with respect to LAB coordinate (which comes from marker data). Also, these are unit vectors and $\mathbf{X_{A_T}}$, $\mathbf{Y_{A_T}}$, $\mathbf{Z_{A_T}}$ are anatomical local axes for thorax.

Figure A1.1: Sensor Marker Frame for the thorax

Figure A1.2 shows all coordinate frames: anatomical, sensor inertial, sensor marker, and LAB -coordinate frames for thorax.
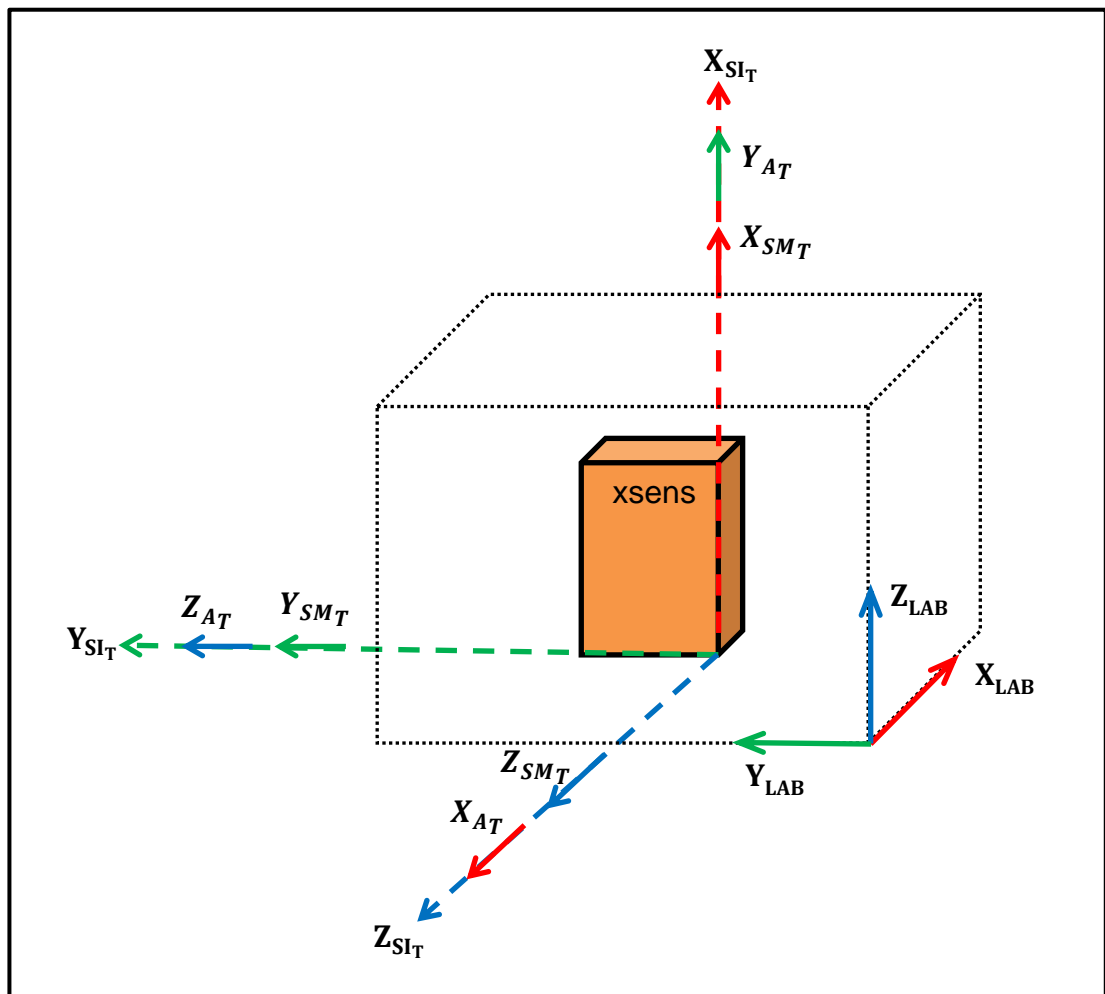
Figure A1.2: $\mathbf{SI_T}$, $\mathbf{A_T}$, $\mathbf{SM_T}$, and $\mathbf{LAB}$ coordinate frames for thorax

Upper-arm – $^{LAB}R_{SM_U}$

The markers (on the upper corners of the sensor) data has been used to calculate a new coordinate system called (**SM**) which nearly aligned with sensor inertial coordinate system (**SI**). For Upper-arm, four markers have been used to create **SM** as follows (Figure A1.3):

$$\mathbf{X_{SM_U}} = \mathbf{P_{\frac{3}{4}}} - \mathbf{P_{\frac{1}{2}}}$$

$\mathbf{X_{SM_U}}$:

$$X_{SM_U} = \left[\frac{x_{U3} + x_{U4} - x_{U1} - x_{U2}}{2}, \frac{y_{U3} + y_{U4} - y_{U1} - y_{U2}}{2}, \frac{z_{U3} + z_{U4} - z_{U1} - z_{U2}}{2} \right],$$

$$\mathbf{X_{SM_U}} = \frac{X_{SM_U}}{|X_{SM_U}|}$$

$$\widetilde{\mathbf{Y}}_{\mathbf{SM_U}} = \mathbf{P}_{\frac{2}{4}} - \mathbf{P}_{\frac{1}{3}}$$

$\widetilde{\mathbf{Y}}_{SM_U}$:

$$\tilde{Y}_{SM_U} = \left[\frac{x_{U2} + x_{U4} - x_{U1} - x_{U3}}{2}, \frac{y_{U2} + y_{U4} - y_{U1} - y_{U3}}{2}, \frac{z_{U2} + z_{U4} - z_{U1} - z_{U3}}{2} \right],$$

$$\widetilde{\mathbf{Y}}_{\mathbf{SM_U}} = \frac{\tilde{Y}_{SM_U}}{|\tilde{Y}_{SM_U}|}$$

$\mathbf{Z_{SM_U}}$:

$$\mathbf{Z_{SM_U}} = \frac{\mathbf{X_{SM_U}} \times \widetilde{\mathbf{Y}}_{SM_U}}{|\mathbf{X_{SM_U}} \times \widetilde{\mathbf{Y}}_{SM_U}|}, \mathbf{Y_{SM_U}} = \mathbf{Z_{SM_U}} \times \mathbf{X_{SM_U}}$$

$$\mathbf{X_{A_U}} = \mathbf{Y_{SM_U}}$$

$$\mathbf{Y_{A_U}} = -\mathbf{X_{SM_U}}$$

$$\mathbf{Z_{A_U}} = \mathbf{Z_{SM_U}}$$

$${}^{LAB}R_{SM_U} = [\mathbf{X_{SM_U}} \ \mathbf{Y_{SM_U}} \ \mathbf{Z_{SM_U}}]$$

$\mathbf{X_{SM_U}}$, $\mathbf{Y_{SM_U}}$, $\mathbf{Z_{SM_U}}$ are a new coordinate system aligned with sensor coordinate system with respect to LAB coordinate (which comes from marker data). $\mathbf{X_{A_U}}$, $\mathbf{Y_{A_U}}$, $\mathbf{Z_{A_U}}$ are anatomical axes for upper-arm.
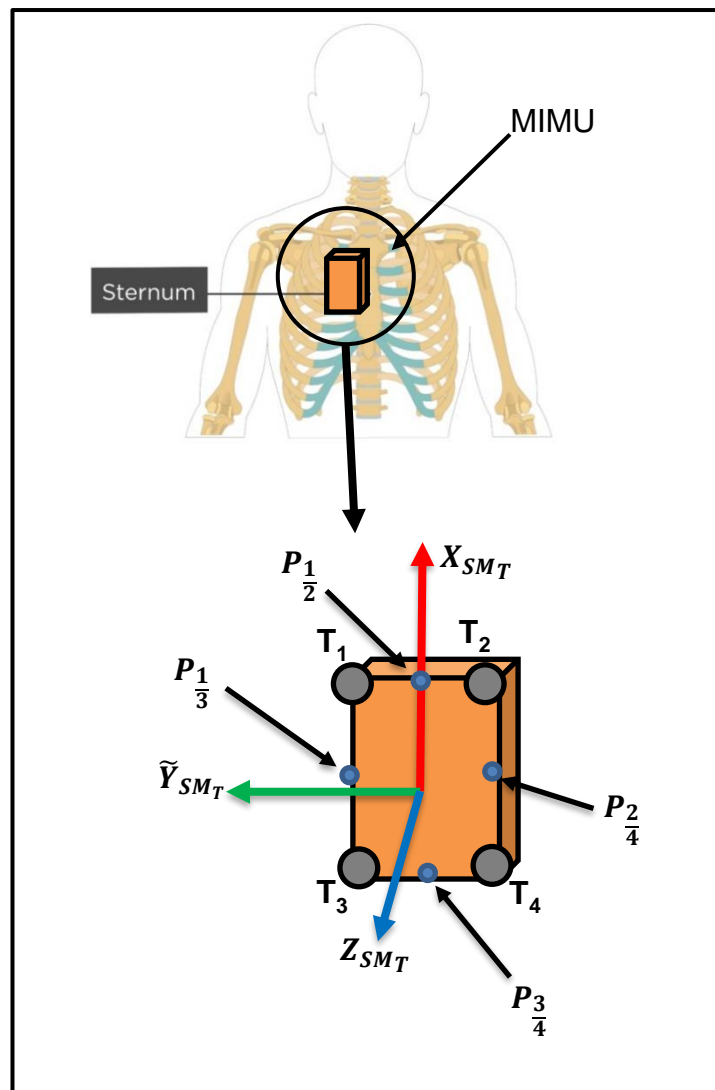
Figure A1.3: Sensor Marker Frame for upper-arm

Figure A1.4 shows all coordinate frames: anatomical, sensor inertial, sensor marker, and LAB -coordinate frames for upper-arm.

Figure A1.4: **SI**ᵤ, **A**ᵤ, **SM**ᵤ, and **LAB** coordinate frames for upper-arm

Forearm – $^{LAB}R_{SM_F}$

The markers (on the upper corners of the sensor) data has been used to calculate a new coordinate system called (**SM**) which nearly aligned with sensor inertial coordinate system (**SI**). For Forearm, four markers have been used to create **SM** as follows (Figure A1.5):

$$X_{SM_F} = P_{\frac{3}{4}} - P_{\frac{1}{2}}$$

$\mathbf{X_{SM_F}}$:

$$X_{SM_F} = \left[\frac{x_{F3} + x_{F4} - x_{F1} - x_{F2}}{2}, \frac{y_{F3} + y_{F4} - y_{F1} - y_{F2}}{2}, \frac{z_{F3} + z_{F4} - z_{F1} - z_{F2}}{2} \right],$$

$$\mathbf{X_{SM_F}} = \frac{X_{SM_F}}{|X_{SM_F}|}$$

$$\mathbf{\widetilde{Y}_{SM_F}} = \mathbf{P_2}_{\frac{}{4}} - \mathbf{P_1}_{\frac{}{3}}$$

$\mathbf{\widetilde{Y}_{SM_F}}$:

$\widetilde{Y}_{SM_F}$

$$= \left[\frac{x_{F2} + x_{F4} - x_{F1} - x_{F3}}{2}, \frac{y_{F2} + y_{F4} - y_{F1} - y_{F3}}{2}, \frac{z_{F2} + z_{F4} - z_{F1} - z_{F3}}{2}\right],$$

$$\mathbf{\widetilde{Y}_{SM_F}} = \frac{\widetilde{Y}_{SM_F}}{|\widetilde{Y}_{SM_F}|}$$

$\mathbf{Z_{SM_F}}$:

$$\mathbf{Z_{SM_F}} = \frac{\mathbf{X_{SM_F}} \times \mathbf{\widetilde{Y}_{SM_F}}}{|\mathbf{X_{SM_F}} \times \mathbf{\widetilde{Y}_{SM_F}}|} , \mathbf{Y_{SM_F}} = \mathbf{Z_{SM_F}} \times \mathbf{X_{SM_F}}$$

$$\mathbf{X_{A_F}} = -\mathbf{Z_{SM_F}}$$

$$\mathbf{Y_{A_F}} = -\mathbf{X_{SM_F}}$$

$$\mathbf{Z_{A_F}} = \mathbf{Y_{SM_F}}$$

$$^{LAB}R_{SM_F} = \left[\mathbf{X_{SM_F}} \ \mathbf{Y_{SM_F}} \ \mathbf{Z_{SM_F}}\right]$$

$\mathbf{X_{SM_F}}$, $\mathbf{Y_{SM_F}}$, $\mathbf{Z_{SM_F}}$ are a new coordinate system aligned with sensor coordinate system with respect to LAB coordinate (which comes from marker data). $\mathbf{X_{A_F}}$, $\mathbf{Y_{A_F}}$, $\mathbf{Z_{A_F}}$ are anatomical axes for Forearm.
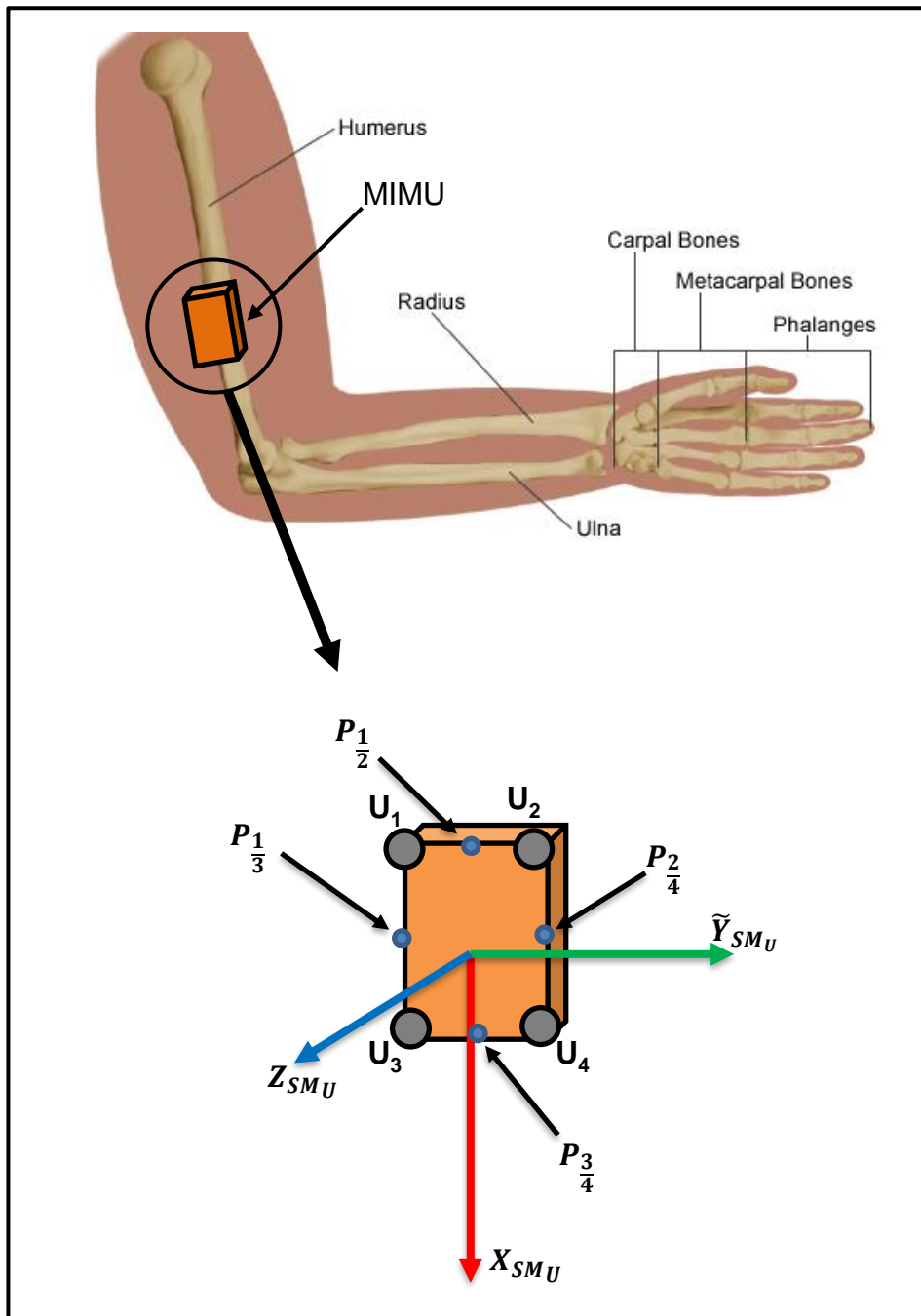
Figure A1.5: Sensor Marker Frame for forearm

Figure A1.6 shows all coordinate frames: anatomical, sensor inertial, sensor marker, and LAB -coordinate frames for forearm.
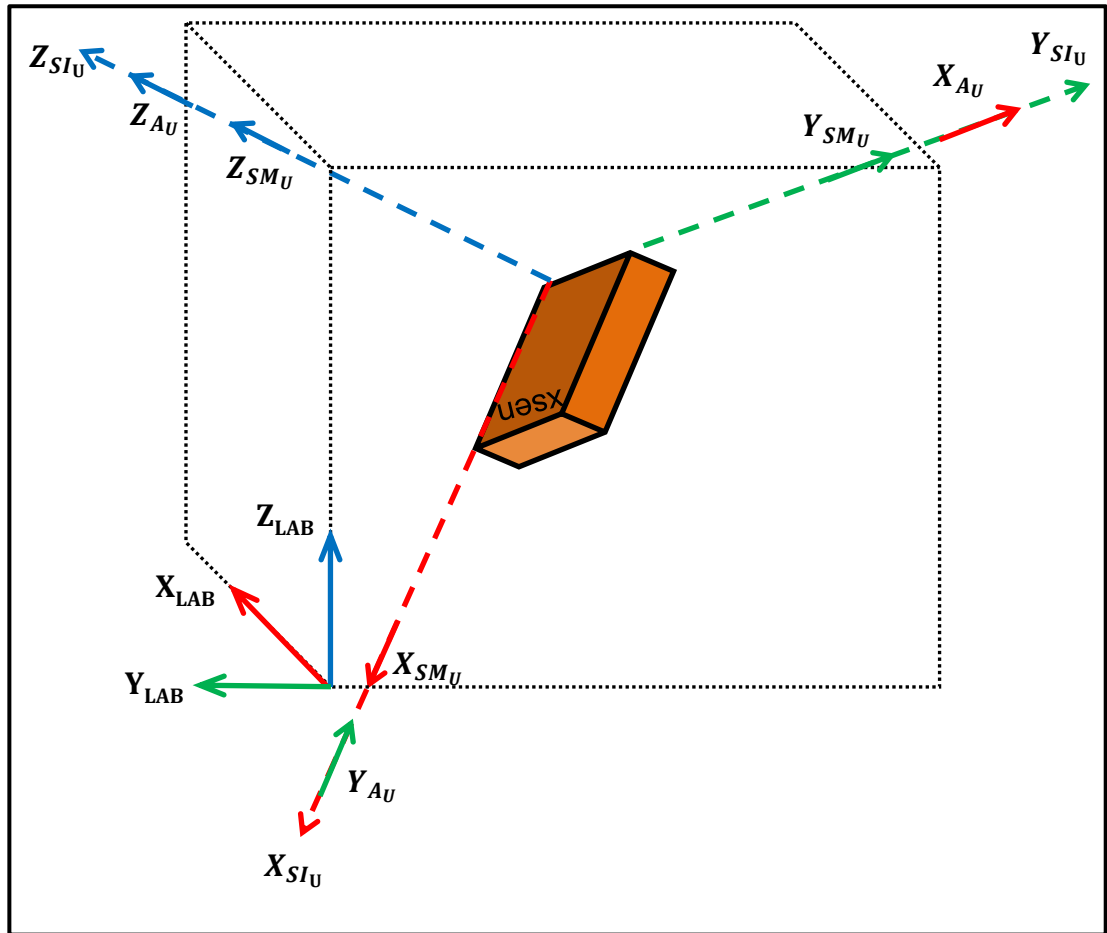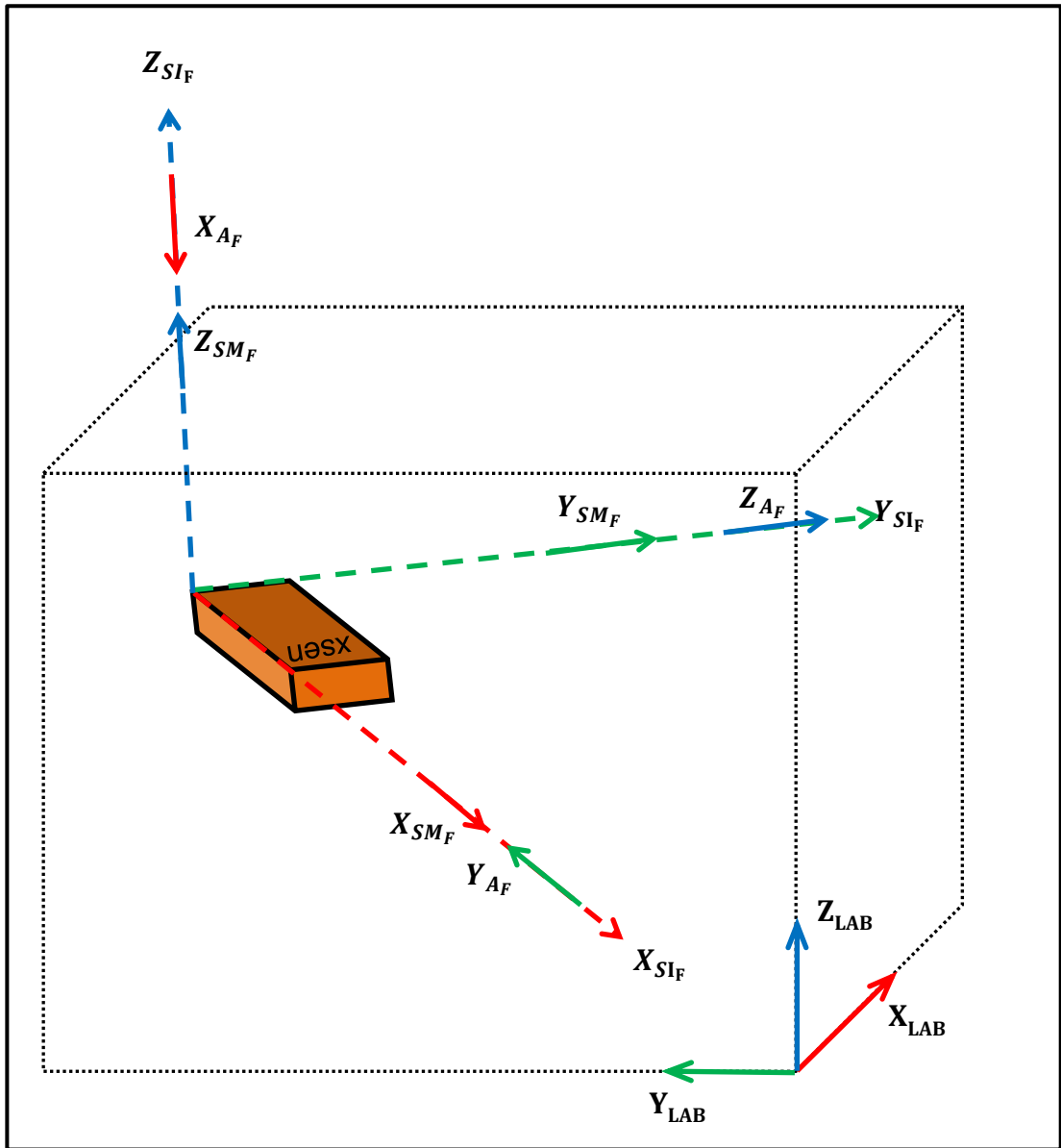
Figure A1.6: **SI_F**, **A_F**, **SM_F**, and **LAB** coordinate frames for upper-arm

Hand – $^{LAB}R_{SM_H}$

The markers (on the upper corners of the sensor) data has been used to calculate a new coordinate system called (**SM**) which nearly aligned with sensor inertial coordinate system (**SI**). For Hand, three markers have been used to create **SM** as follows (Figure A1.7):

X_{SM_H}:

$$X_{SM_H} = [x_{H1} - x_{H3} , y_{H1} - y_{H3} , z_{H1} - z_{H3}],$$

$$\mathbf{X_{SM_H}} = \frac{X_{SM_H}}{\left|X_{SM_H}\right|}$$

$\widetilde{\mathbf{Y}}_{\mathbf{SM_H}}$:

$$\tilde{Y}_{SM_H} = [x_{H1} - x_{H2}, y_{H1} - y_{H2}, z_{H1} - z_{H2}],$$

$$\widetilde{\mathbf{Y}}_{\mathbf{SM_H}} = \frac{\tilde{Y}_{SM_H}}{\left|\tilde{Y}_{SM_H}\right|}$$

$\mathbf{Z_{SM_H}}$:

$$\mathbf{Z_{SM_H}} = \frac{\mathbf{X_{SM_H}} \times \widetilde{\mathbf{Y}}_{\mathbf{SM_H}}}{\left|\mathbf{X_{SM_H}} \times \widetilde{\mathbf{Y}}_{\mathbf{SM_H}}\right|}, \mathbf{Y_{SM_H}} = \mathbf{Z_{SM_H}} \times \mathbf{X_{SM_H}}$$

$$\mathbf{X_{A_H}} = -\mathbf{Z_{SM_H}}$$

$$\mathbf{Y_{A_H}} = \mathbf{X_{SM_H}}$$

$$\mathbf{Z_{A_H}} = -\mathbf{Y_{SM_H}}$$

$$^{LAB}R_{SM_H} = \begin{bmatrix} \mathbf{X_{SM_H}} & \mathbf{Y_{SM_H}} & \mathbf{Z_{SM_H}} \end{bmatrix}$$

$\mathbf{X_{SM_H}}$, $\mathbf{Y_{SM_H}}$, $\mathbf{Z_{SM_H}}$ are a new coordinate system aligned with sensor coordinate system with respect to LAB coordinate (which comes from marker data). $\mathbf{X_{A_H}}$, $\mathbf{Y_{A_H}}$, $\mathbf{Z_{A_H}}$ are anatomical axes for Hand.
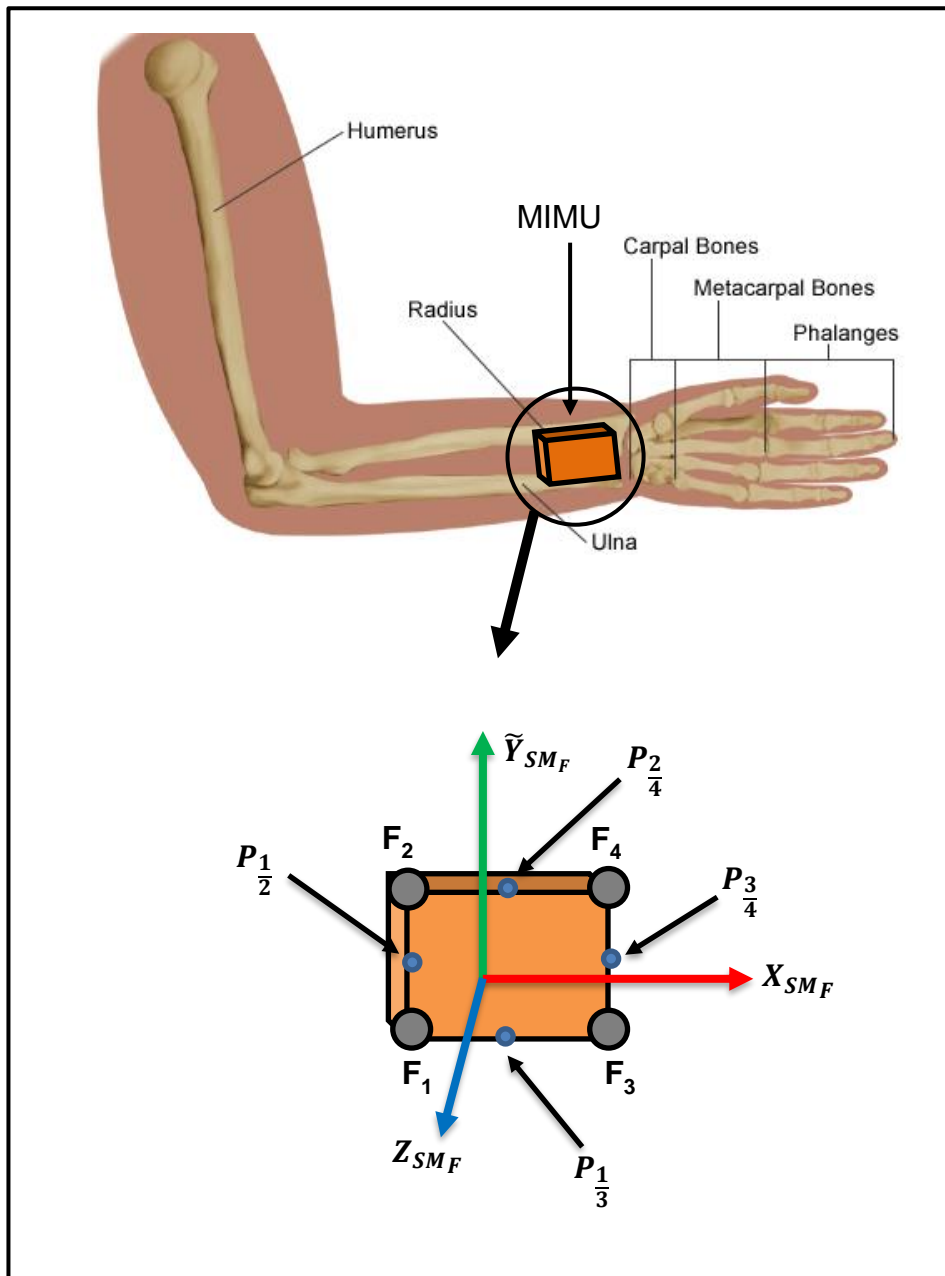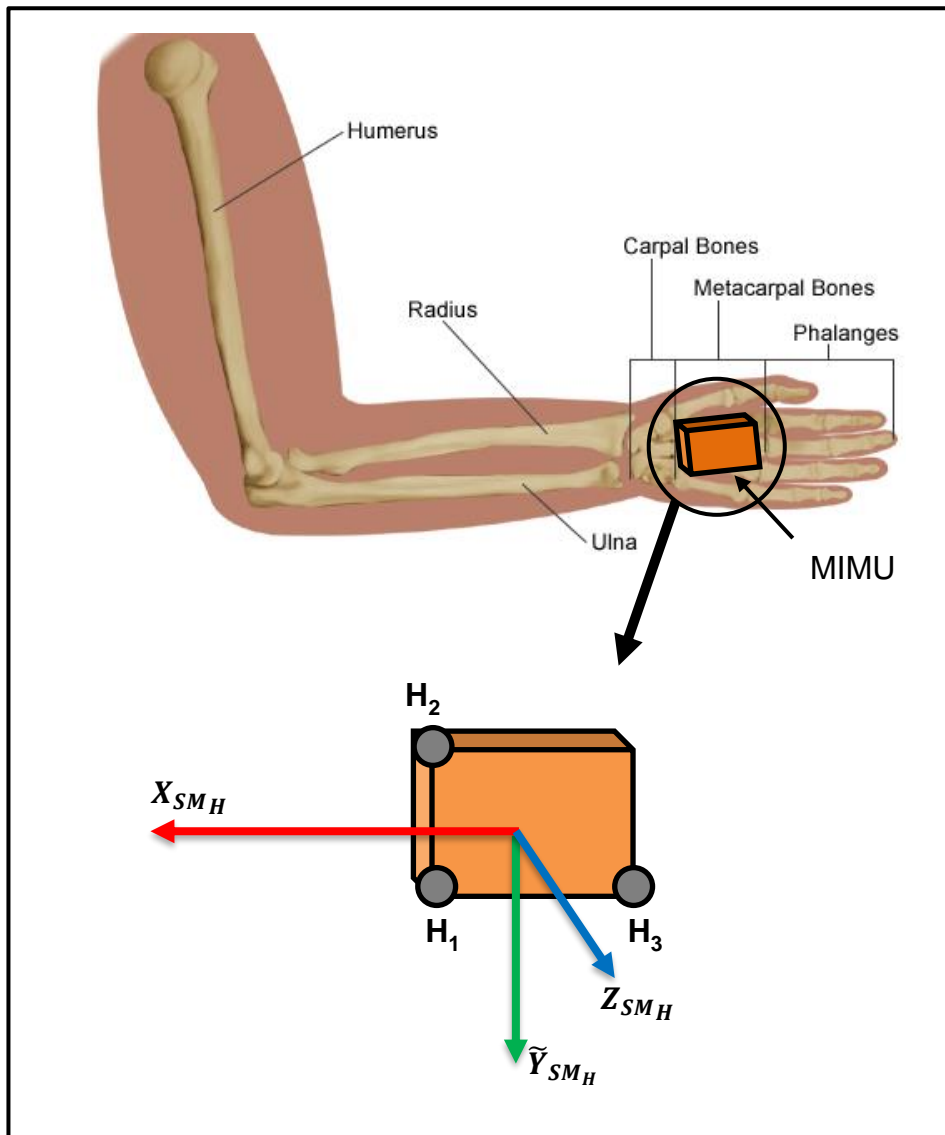
Figure A1.7: Sensor Marker Frame for hand

Figure A1.8 shows all coordinate frames: anatomical, sensor inertial, sensor marker, and LAB -coordinate frames for hand.
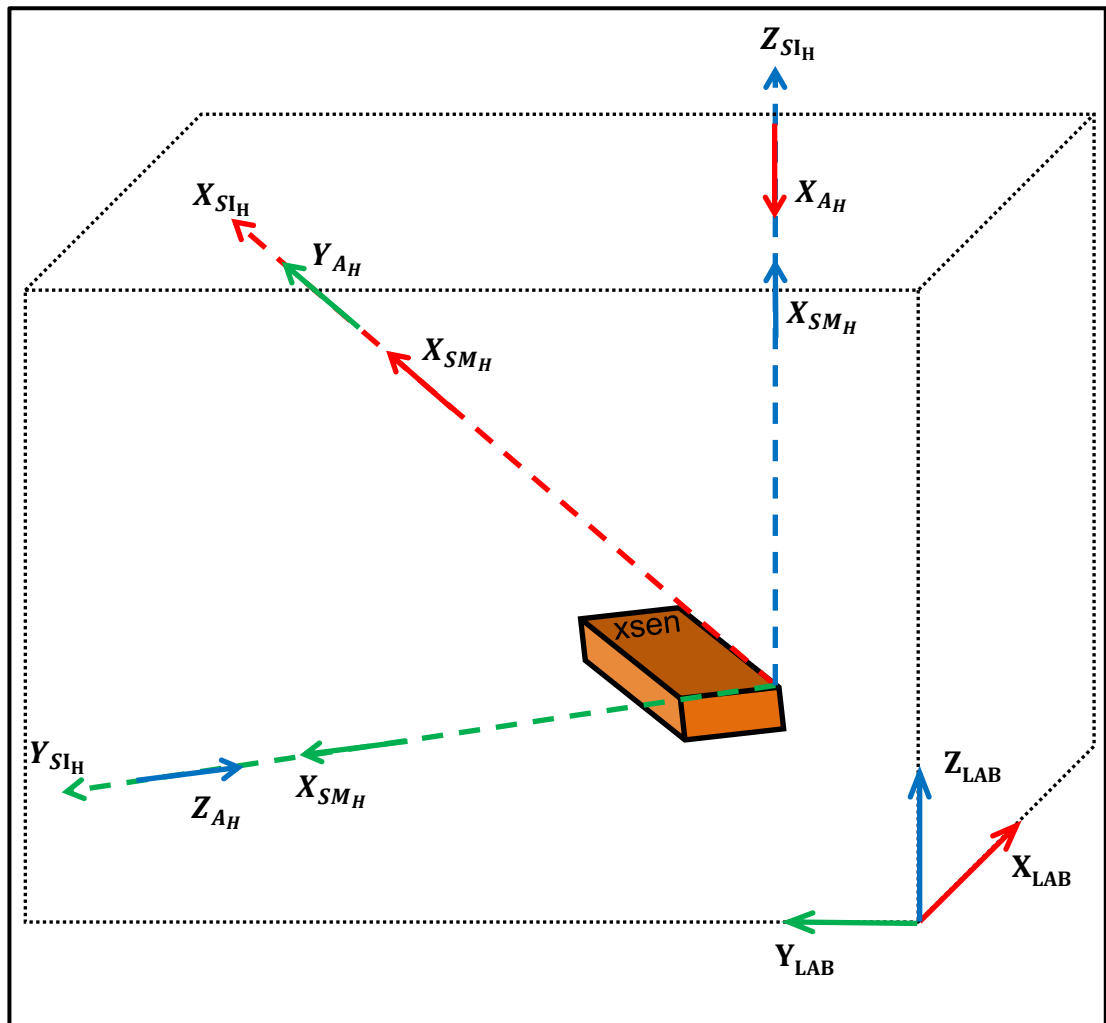
Figure A1.8: **SI_H**, **A_H**, **SM_H**, and **LAB** coordinate frames for upper-arm

Appendix 2 – Probabilities for upper-limb segments

Probabilities for Table 5.9 in Abdullah's thesis

For most segments, this is the equivalent of asking what the probability is of getting agreement when we throw an eight-sided dice five times (i.e. for 5 participants).

Firstly, the number of permutations of 5 calibration rotation matrices (one for each participant) have been derived, taken from 8 alternative matrices, that give each level of agreement between the 5 participants as follows. This has been done for eight alternatives to begin with, which applies to all segments except the forearm.

1. Agreement between 5 from 5 – number of permutations

The only way to achieve agreement between *5 from 5* participants (5 eight-sided dice rolls) is if they all have the same calibration matrix, of which there are eight alternatives. Therefore, there are eight permutations that achieve this – [1 1 1 1 1] or [2 2 2 2 2]... or [8 8 8 8 8].

2. Agreement between 4 from 5 – number of permutations

The following five patterns give agreement between *4 from 5* participants (5 eight-sided dice rolls):

1 1 1 1 0

1 1 1 0 1

1 1 0 1 1

1 0 1 1 1

0 1 1 1 1

Where 1 represents the calibration matrix in agreement and 0 represents any of the other 7 possibilities. Therefore, for one calibration matrix (e.g. 1 as shown in

the patterns above), there are 35 ways to get agreement between *4 from 5* (5 patterns multiplied by 7 possibilities for 0).

Finally, this logic applies if 1 is replaced by any of the eight alternative matrices. So, the total number of permutations that give agreement between *4 from 5* participants is 8 x 35 = 280.

3. <u>Agreement between 3 from 5 – number of permutations</u>

The following ten patterns give agreement between *3 from 5* participants (5 eight-sided dice rolls):

1 1 1 0 0   1 0 1 1 0   0 1 1 1 0   0 0 1 1 1

1 1 0 1 0   1 0 1 0 1   0 1 1 0 1

1 1 0 0 1   1 0 0 1 1   0 1 0 1 1

Where 1 represents the calibration matrix in agreement and 0 represents any of the other 7 possibilities. Therefore, for one calibration matrix (e.g. 1 as shown in the patterns above), there are 490 ways to get agreement between *3 from 5* (10 patterns multiplied by 7^2 possibilities for [0 0]).

Finally, this logic applies if 1 is replaced by any of the eight alternative matrices. So, the total number of permutations that give agreement between *3 from 5* participants is 8 x 490 = 3,920.

From the three cases above, a general formula can be deduced for the number of permutations:

$$N_P = 8 \times K \times 7^{(5-X)}$$

Where K is the number of patterns that give agreement between X *from 5* participants (5 eight-sided dice rolls).

4. <u>Agreement between 2 from 5 – number of permutations</u>

The following ten patterns give agreement between *2 from 5* participants (5 eight-sided dice rolls):

1 1 0 0 0   1 0 1 0 0   0 1 1 0 0   0 0 1 1 0

              1 0 0 1 0   0 1 0 1 0   0 0 1 0 1

              1 0 0 0 1   0 1 0 0 1   0 0 0 1 1

Where 1 represents the calibration matrix in agreement and 0 represents any of the other 7 possibilities. Therefore, applying the general formula derived above we get:

$$N_P = 8 \times K \times 7^{(5-X)} = 8 \times 10 \times 7^3 = 27,440$$

However, this led to too many permutations in total (i.e. more than 8^5). This is because *2 from 5* is a special case where the 7^3 possibilities for [0 0 0] can lead to duplicates of *3 from 5* and also two agreement pairs (e.g. 1 1 0 3 3), some of which are duplicates.

For one calibration matrix (e.g. 1 as shown in the patterns above), there are seven ways that duplicates of *3 from 5* can arise – [2 2 2] or [3 3 3]… or [8 8 8].

For one calibration matrix (e.g. 1 as shown in the patterns above), two agreement pairs can occur because of three patterns of the 7^3 possibilities for [0 0 0] as follows:

2 2 0

2 0 2

0 2 2

Where 2 represents the second agreement pair and 0 represents any of the other 6 possibilities (not including the calibration matrices of the agreeing pairs – 1 and 2). This logic applies if 2 is replaced by any of the seven alternative matrices (not including 1). So, the number of the 7^3 possibilities for [0 0 0] that give two agreement pairs is 7 x 3 x 6 = 126. Half of these (63) are duplicates because the primary and secondary agreement pairs can be swapped as follows:

1 1 0 3 3 or 1 1 0 *3 3*

Where the bolded italics is the primary agreement pair (i.e. not formed from the 7^3 possibilities for [0 0 0]).

So, there are 7 duplicates of *3 from 5* and 63 duplicates of two agreement pairs and, hence, the general formula is modified as follows in the *2 from 5* case:

$$N_P = 8 \times K \times (7^{(5-X)} - 70) = 8 \times 10 \times (7^3 - 70) = 21{,}840$$

5. <u>No agreement – number of permutations</u>

The number of permutations where there is no agreement is equal to the number of permutations without repetition, which is given by:

$$N_P = \frac{n!}{(n-k)!} = \frac{8!}{(8-5)!} = 6{,}720$$

Where 8 is the number of alternatives and 5 is the length of the permutation.

6. <u>Summary of results</u>

Level of agreement	Number of permutations	Probability
5 from 5	8	0.0002
4 from 5	280	0.0085
3 from 5	3,920	0.1196
2 from 5	21,840	0.6665
No agreement	6,720	0.2051
TOTAL	**32,768**	**0.9999**

The total number of permutations is equal to 8^5 as it should be, which gives confidence that the more complex logic for the *2 from 5* case is correct.

Interestingly, when rolling an eight-sided dice five times, the most likely outcome is an agreement pair or two agreement pairs (*p=0.6665*).

7. <u>The forearm – ten alternative matrices</u>

In this case the formulae are modified as follows for a ten-sided dice:

For $X > 2$: $N_P = 10 \times K \times 9^{(5-X)}$

For $X = 2$: $N_P = 10 \times K \times \left(9^{(5-X)} - 117\right) = 10 \times 10 \times (9^3 - 117) = 61{,}200$

Where the number of permutations that give two agreement pairs is 9 x 3 x 8 = 216, half of which are duplicates (108), and there are 9 duplicates of *3 from 5*. So there are 117 duplicates in total.

For no agreement: $N_P = \dfrac{n!}{(n-k)!} = \dfrac{10!}{(10-5)!} = 30{,}240$

The table of permutations and probabilities is then as follows:

Level of agreement	Number of permutations	Probability
5 from 5	10	0.0001
4 from 5	450	0.0045
3 from 5	8,100	0.081
2 from 5	61,200	0.612
No agreement	30,240	0.3024
TOTAL	**100,000**	**1**

The total number of permutations is equal to 10^5 as it should be.

REFERENCES

Al-Ani, A., Howard, D., & Kenney, L. (2017). Calibration Methods for Magneto-Inertial Measurement Units in Upper-Limb FES. In *IFESS Conference 2017*.

B Morrow, M. M., Lowndes, B. R., Fortune, E., Kaufman, K. R., Susan Hallbeck, M., Kern, P. E., … Appl Biomech Author manuscript, J. (2017). Validation of Inertial Measurement Units for Upper Body Kinematics HHS Public Access Author manuscript. *J Appl Biomech*, *33*(3), 227–232. https://doi.org/10.1123/jab.2016-0120

Bachmann, E. R., McGhee, R. B., Yun, X., & Zyda, M. J. (2001). Inertial and magnetic posture tracking for inserting humans into networked virtual environments. In *Proceedings of the ACM symposium on Virtual reality software and technology - VRST '01* (p. 9). New York, New York, USA: ACM Press. https://doi.org/10.1145/505008.505011

Baker, L. L., Wederich, C. L., Newsam, C., & Waters, R. L. (2000). *Neuro Muscular Electrical Stimulation A Practical Guide* (4th Ed). Los Amigos Research Institute, Inc.

Barker, R. N., Brauer, S. G., & Carson, R. G. (2008). Training of reaching in stroke survivors with severe and chronic upper limb paresis using a novel nonrobotic device: a randomized clinical trial. *Stroke; a Journal of Cerebral Circulation*, *39*(6), 1800–1807. https://doi.org/10.1161/STROKEAHA.107.498485

Bear, M. F., Connors, B. W., & Paradiso, M. A. (1996). *Neuroscience: Exploring the Brain* (3rd Editio). Lippincott Williams & Wilkins.

Bodor, R., Jackson, B., Masoud, O., & Papanikolopoulos, N. (2003). Image-based reconstruction for view-independent human motion recognition. In *Proceedings 2003 IEEE/RSJ International Conference on Intelligent Robots and Systems (IROS 2003) (Cat. No.03CH37453)* (Vol. 2, pp. 1548–1553). IEEE. https://doi.org/10.1109/IROS.2003.1248864

Bonnet, S., Bassompierre, C., Godin, C., Lesecq, S., & Barraud, A. (2009).

Calibration methods for inertial and magnetic sensors. *Sensors and Actuators A: Physical*, *156*(2), 302–311. https://doi.org/10.1016/j.sna.2009.10.008

Bouvier, B., Duprey, S., Claudon, L., Dumas, R., & Savescu, A. (2015). Upper limb kinematics using inertial and magnetic sensors: Comparison of sensor-to-segment calibrations. *Sensors*, *15*(8), 18813–18833. https://doi.org/10.3390/s150818813

Broeks, J. G., Lankhorst, G. J., Rumping, K., & Prevo, A. J. (1999). The long-term outcome of arm function after stroke: results of a follow-up study. *Disability and Rehabilitation*, *21*(8), 357–364. https://doi.org/10.1080/096382899297459

Burgar, C. G., Lum, P. S., Scremin, A. M. E., Garber, S. L., Van der Loos, H. F. M., Kenney, D., & Shor, P. (2011). Robot-assisted upper-limb therapy in acute rehabilitation setting following stroke: Department of Veterans Affairs multisite clinical trial. *Journal of Rehabilitation Research and Development*, *48*(4), 445–458. Retrieved from http://www.ncbi.nlm.nih.gov/pubmed/21674393

Burke, R. E. (2007). Sir Charles Sherrington's the integrative action of the nervous system: A centenary appreciation. *Brain*, *130*(4), 887–894. https://doi.org/10.1093/brain/awm022

Caplan, L. R. (2010). *Stroke*. New York: Demos Health Publishing.

Cappozzo, A. (1983). Stereophotogrammetric system for kinesiological studies. *Medical & Biological Engineering & Computing*, *21*(2), 217–223. Retrieved from http://www.ncbi.nlm.nih.gov/pubmed/6887999

Cappozzo, A, Catani, F., Della Croce, U., & Leardini, A. (1995). Position and orietnation in space of bones during movement. *Clin. Biomech.*, *10*(4), 171–178. https://doi.org/10.1016/0268-0033(95)91394-T

Cappozzo, Aurelio, Della Croce, U., Leardini, A., & Chiari, L. (2005). Human movement analysis using stereophotogrammetry Part 1: theoretical

background. *Gait & Posture*, *21*(2), 186–196. https://doi.org/10.1016/j.gaitpost.2004.01.010

Chiari, L., Della Croce, U., Leardini, A., & Cappozzo, A. (2005). Human movement analysis using stereophotogrammetry Part 2: instrumental errors. *Gait & Posture*, *21*(2), 197–211. https://doi.org/10.1016/j.gaitpost.2004.04.004

Chizek, H. J., Kobetic, R., Marsolais, E. B., Abbas, J. J., Donner, I. H., & Simon, E. (1988). Control of functional neuromuscular stimulation systems for standing and locomotion in paraplegics. *Proceedings of the IEEE, 76*(9), 1155–1165. https://doi.org/10.1109/5.9661

Coley, B., Jolles, B. M., Farron, A., Bourgeois, A., Nussbaumer, F., Pichonnaz, C., & Aminian, K. (2007). Outcome evaluation in shoulder surgery using 3D kinematics sensors. *Gait & Posture*, *25*(4), 523–532. https://doi.org/10.1016/j.gaitpost.2006.06.016

Cordillet, S., Bideau, N., Bideau, B., & Nicolas, G. (2019). Estimation of 3D knee joint angles during cycling using inertial sensors: Accuracy of a novel sensor-to-segment calibration procedure based on pedaling motion. *Sensors (Switzerland)*, *19*(11). https://doi.org/10.3390/s19112474

Crago, P. E., Lan, N., Veltink, P. H., Abbas, J. J., & Kantor, C. (1996). New control strategies for neuroprosthetic systems. *Journal of Rehabilitation Research and Development*, *33*(2), 158–172. Retrieved from http://www.ncbi.nlm.nih.gov/pubmed/8724171

Craig, J. J. (2005). *Introduction to Robotics: Mechanics and Control* (3rd Ed). Upper Saddle River, New Jersey: Pearson Prentice Hall.

Crook, S. E., & Chappell, P. H. (1998). A portable system for closed loop control of the paralysed hand using functional electrical stimulation. *Medical Engineering & Physics*, *20*(1), 70–76.

Cutti, A. G., Ferrari, A., Garofalo, P., Raggi, M., Cappello, A., & Ferrari, A. (2010). 'Outwalk': a protocol for clinical gait analysis based on inertial and magnetic

sensors. *Medical & Biological Engineering & Computing*, *48*(1), 17–25. https://doi.org/10.1007/s11517-009-0545-x

Cutti, A. G., Giovanardi, A., Rocchi, L., Davalli, A., & Sacchetti, R. (2008). Ambulatory measurement of shoulder and elbow kinematics through inertial and magnetic sensors. *Medical & Biological Engineering & Computing*, *46*(2), 169–178. https://doi.org/10.1007/s11517-007-0296-5

de Kroon, J. R., Ijzerman, M. J., Chae, J., Lankhorst, G. J., & Zilvold, G. (2005). Relation between stimulation characteristics and clinical outcome in studies using electrical stimulation to improve motor control of the upper extremity in stroke. *Journal of Rehabilitation Medicine*, *37*(2), 65–74. https://doi.org/10.1080/16501970410024190

De Kroon, J., Van der Lee, J., IJzerman, M., & Lankhorst, G. (2002). Therapeutic electrical stimulation to improve motor control and functional abilities of the upper extremity after stroke: a systematic review. *Clinical Rehabilitation*, *16*(4), 350–360. https://doi.org/10.1191/0269215502cr504oa

de Vries, W. H. K., Veeger, H. E. J., Cutti, A. G., Baten, C., & van der Helm, F. C. T. (2010). Functionally interpretable local coordinate systems for the upper extremity using inertial & magnetic measurement systems. *Journal of Biomechanics*, *43*(10), 1983–1988. https://doi.org/10.1016/j.jbiomech.2010.03.007

Ehara, Y, Fujimoto, H., Miyazaki, S., Tanaka, S., & Yamamoto, S. (1995). Comparison of the performance of 3D camera systems. *Gait & Posture*, *3*(3), 166–169. https://doi.org/10.1016/0966-6362(95)99067-U

Ehara, Yoshihiro, Fujimoto, H., Miyazaki, S., Mochimaru, M., Tanaka, S., & Yamamoto, S. (1997). Comparison of the performance of 3D camera systems II. *Gait & Posture*, *5*(3), 251–255. https://doi.org/10.1016/S0966-6362(96)01093-4

Favre, J., Aissaoui, R., Jolles, B. M., de Guise, J. A., & Aminian, K. (2009). Functional calibration procedure for 3D knee joint angle description using

inertial sensors. *Journal of Biomechanics*, *42*(14), 2330–2335. https://doi.org/10.1016/j.jbiomech.2009.06.025

Ferrari, A., Cutti, A. G., Garofalo, P., Raggi, M., Heijboer, M., Cappello, A., & Davalli, A. (2010). First in vivo assessment of "Outwalk": a novel protocol for clinical gait analysis based on inertial and magnetic sensors. *Medical & Biological Engineering & Computing*, *48*(1), 1–15. https://doi.org/10.1007/s11517-009-0544-y

Ferrarin, M., Palazzo, F., Riener, R., & Quintern, J. (2001). Model-based control of FES-induced single joint movements. *IEEE Transactions on Neural Systems and Rehabilitation Engineering*, *9*(3), 245–257. https://doi.org/10.1109/7333.948452

Galinski, D., & Dehez, B. (2012). Evaluation of initialization procedures for estimating upper limb kinematics with MARG sensors. In *2012 4th IEEE RAS & EMBS International Conference on Biomedical Robotics and Biomechatronics (BioRob)* (pp. 1801–1806). IEEE. https://doi.org/10.1109/BioRob.2012.6290305

Grood, E. S., & Suntay, W. J. (1983). A Joint Coordinate System for the Clinical Description of Three-Dimensional Motions: Application to the Knee. *Journal of Biomechanical Engineering*, *105*(2), 136. https://doi.org/10.1115/1.3138397

Harris, J. E., & Eng, J. J. (2010). Strength training improves upper-limb function in individuals with stroke: a meta-analysis. *Stroke; a Journal of Cerebral Circulation*, *41*(1), 136–140. https://doi.org/10.1161/STROKEAHA.109.567438

Heller, A., Wade, D. T., Wood, V. A., Sunderland, A., Hewer, R. L., & Ward, E. (1987). Arm function after stroke: measurement and recovery over the first three months. *Journal of Neurology, Neurosurgery, and Psychiatry*, *50*(6), 714–719. https://doi.org/10.1136/jnnp.50.6.714

Hillman, M. (2004). 2 Rehabilitation Robotics from Past to Present – A Historical

Perspective. In Z. Z. Bien & D. Stefanov (Eds.), *Advances in Rehabilitation Robotics* (pp. 25–44). Berlin, Heidelberg: Springer Berlin Heidelberg. https://doi.org/10.1007/10946978_2

Howlett, O. A., Lannin, N. A., Ada, L., & McKinstry, C. (2015). Functional Electrical Stimulation Improves Activity After Stroke: A Systematic Review With Meta-Analysis. *Archives of Physical Medicine and Rehabilitation*, *96*(5), 934–943. https://doi.org/10.1016/j.apmr.2015.01.013

Hughes, A. M., Freeman, C. T., Burridge, J. H., Chappell, P. H., Lewin, P. L., Pickering, R. M., & Rogers, E. (2009). Shoulder and elbow muscle activity during fully supported trajectory tracking in neurologically intact older people. *Journal of Electromyography and Kinesiology : Official Journal of the International Society of Electrophysiological Kinesiology*, *19*(6), 1025–1034. https://doi.org/10.1016/j.jelekin.2008.09.015

Knutson, J. S., Hoyen, H. A., Kilgore, K. L., & Peckham, P. H. (2004). Simulated neuroprosthesis state activation and hand-position control using myoelectric signals from wrist muscles. *The Journal of Rehabilitation Research and Development*, *41*(3b), 461. https://doi.org/10.1682/JRRD.2003.04.0053

Kwakkel, G., Wegen, E. Van, Burridge, J., Winstein, C., Dokkum, L. van, Murphy, M. A., … Krakauer, J. (2019). Standardized measurement of quality of upper limb movement after stroke: Consensus-based core recommendations from the Second Stroke Recovery and Rehabilitation Roundtable. *International Journal of Stroke*, *14*(8), 174749301987351. https://doi.org/10.1177/1747493019873519

Lang, C. E., MacDonald, J. R., Reisman, D. S., Boyd, L., Jacobson Kimberley, T., Schindler-Ivens, S. M., … Scheets, P. L. (2009). Observation of Amounts of Movement Practice Provided During Stroke Rehabilitation. *Archives of Physical Medicine and Rehabilitation*, *90*(10), 1692–1698. https://doi.org/10.1016/j.apmr.2009.04.005

Lin, J. F. S., & Kulić, D. (2012). Human pose recovery using wireless inertial measurement units. *Physiological Measurement*, *33*(12), 2099–2115.

https://doi.org/10.1088/0967-3334/33/12/2099

Liu, T., Inoue, Y., & Shibata, K. (2009). Development of a wearable sensor system for quantitative gait analysis. *Measurement*, *42*(7), 978–988. https://doi.org/10.1016/j.measurement.2009.02.002

Liu, Y. T., Zhang, Y. A., & Zeng, M. (2019). Sensor to segment calibration for magnetic and inertial sensor based motion capture systems. *Measurement: Journal of the International Measurement Confederation*, *142*, 1–9. https://doi.org/10.1016/j.measurement.2019.03.048

Luinge, H. J., & Veltink, P. H. (2005). Measuring orientation of human body segments using miniature gyroscopes and accelerometers. *Medical and Biological Engineering and Computing*, *43*(2), 273–282. https://doi.org/10.1007/BF02345966

Luinge, H. J., Veltink, P. H., & Baten, C. T. M. (2007). Ambulatory measurement of arm orientation. *Journal of Biomechanics*, *40*(1), 78–85. https://doi.org/10.1016/j.jbiomech.2005.11.011

Luinge, Henk J, & Veltink, P. H. (2004). Inclination measurement of human movement using a 3-D accelerometer with autocalibration. *IEEE Transactions on Neural Systems and Rehabilitation Engineering : A Publication of the IEEE Engineering in Medicine and Biology Society*, *12*(1), 112–121. https://doi.org/10.1109/TNSRE.2003.822759

Lynch, C. L., & Popovic, M. R. (2008). Functional Electrical Stimulation. *IEEE Control Systems Magazine*, *28*(2), 40–50. https://doi.org/10.1109/MCS.2007.914689

Management of Stroke Rehabilitation Working Group. (2010). VA/DOD Clinical practice guideline for the management of stroke rehabilitation. *Journal of Rehabilitation Research and Development*, *47*(9), 1–43. Retrieved from http://www.ncbi.nlm.nih.gov/pubmed/21213454

Mancini, M., Zampieri, C., Carlson-Kuhta, P., Chiari, L., & Horak, F. B. (2009). Anticipatory postural adjustments prior to step initiation are hypometric in

untreated Parkinson's disease: an accelerometer-based approach. *European Journal of Neurology*, *16*(9), 1028–1034. https://doi.org/10.1111/j.1468-1331.2009.02641.x

Merad, M., Roby-Brami, A., & Jarrasse, N. (2016). Towards the implementation of natural prosthetic elbow motion using upper limb joint coordination. *Proceedings of the IEEE RAS and EMBS International Conference on Biomedical Robotics and Biomechatronics*, *2016-July*, 821–826. https://doi.org/10.1109/BIOROB.2016.7523729

Miller, L. M., Kim, H., & Rosen, J. (2011). Redundancy and joint limits of a seven degree of freedom upper limb exoskeleton. In *2011 Annual International Conference of the IEEE Engineering in Medicine and Biology Society* (Vol. 1, pp. 8154–8157). IEEE. https://doi.org/10.1109/IEMBS.2011.6092011

Monkhouse, S. (2005). *Cranial Nerves Functional Anatomy*. *Functional Anatomy*. Cambridge University Press. Retrieved from http://www.amazon.com/Cranial-Nerves-Functional-Stanley-Monkhouse/dp/0521615372?SubscriptionId=1V7VTJ4HA4MFT9XBJ1R2&tag=mekentosjcom-20&linkCode=xm2&camp=2025&creative=165953&creativeASIN=0521615372%5Cnpapers3://publication/uuid/7849785C-BB3E-41B3-84A3-E9FE

Murgia, A., Kerkhofs, V., Savelberg, H., & Meijer, K. (2010). A portable device for the clinical assessment of upper limb motion and muscle synergies. In *2010 Annual International Conference of the IEEE Engineering in Medicine and Biology* (pp. 931–934). IEEE. https://doi.org/10.1109/IEMBS.2010.5627522

Newman, C. J., Bruchez, R., Roches, S., Jequier Gygax, M., Duc, C., Dadashi, F., … Aminian, K. (2017). Measuring upper limb function in children with hemiparesis with 3D inertial sensors. *Child's Nervous System*, *33*(12), 2159–2168. https://doi.org/10.1007/s00381-017-3580-1

Nudo, R. J., Plautz, E. J., & Milliken, G. W. (1997). Adaptive Plasticity in Primate Motor Cortex as a Consequence of Behavioral Experience and Neuronal Injury. *Seminars in Neuroscience*, *9*(1–2), 13–23.

https://doi.org/10.1006/smns.1997.0102

O'Donovan, K. J., Kamnik, R., O'Keeffe, D. T., & Lyons, G. M. (2007). An inertial and magnetic sensor based technique for joint angle measurement. *Journal of Biomechanics*, *40*(12), 2604–2611. https://doi.org/10.1016/j.jbiomech.2006.12.010

Parel, I., Cutti, A. G., Fiumana, G., Porcellini, G., Verni, G., & Accardo, A. P. (2012). Ambulatory measurement of the scapulohumeral rhythm: intra- and inter-operator agreement of a protocol based on inertial and magnetic sensors. *Gait & Posture*, *35*(4), 636–640. https://doi.org/10.1016/j.gaitpost.2011.12.015

Parker, V. M., Wade, D. T., & Langton Hewer, R. (1986). Loss of arm function after stroke: measurement, frequency, and recovery. *International Rehabilitation Medicine*, *8*(2), 69–73. Retrieved from http://www.ncbi.nlm.nih.gov/pubmed/3804600

Pérez, R., Costa, Ú., Torrent, M., Solana, J., Opisso, E., Cáceres, C., … Gómez, E. J. (2010). Upper Limb Portable Motion Analysis System Based on Inertial Technology for Neurorehabilitation Purposes. *Sensors*, *10*(12), 10733–10751. https://doi.org/10.3390/s101210733

Picerno, P., Cereatti, A., & Cappozzo, A. (2008). Joint kinematics estimate using wearable inertial and magnetic sensing modules. *Gait & Posture*, *28*(4), 588–595. https://doi.org/10.1016/j.gaitpost.2008.04.003

Pierrot-Deseilligny, E., & Burque, D. (2005). *The circuitry of the human spinal cord: its role in motor control and movement disorders. Brain* (Vol. 129). https://doi.org/10.1017/CBO9781139026727

Plamondon, A., Delisle, A., Larue, C., Brouillette, D., McFadden, D., Desjardins, P., & Larivière, C. (2007). Evaluation of a hybrid system for three-dimensional measurement of trunk posture in motion. *Applied Ergonomics*, *38*(6), 697–712. https://doi.org/10.1016/j.apergo.2006.12.006

Poitras, I., Dupuis, F., Bielmann, M., Campeau-Lecours, A., Mercier, C., Bouyer,

L. J., & Roy, J. S. (2019). Validity and reliability ofwearable sensors for joint angle estimation: A systematic review. *Sensors (Switzerland)*, *19*(7), 1–17. https://doi.org/10.3390/s19071555

Popović, D. B. (2014). Advances in functional electrical stimulation (FES). *Journal of Electromyography and Kinesiology, 24*(6), 795–802. https://doi.org/10.1016/j.jelekin.2014.09.008

Prayudi, I., & Kim, D. (2012). Design and implementation of IMU-based human arm motion capture system. In *2012 IEEE International Conference on Mechatronics and Automation* (pp. 670–675). IEEE. https://doi.org/10.1109/ICMA.2012.6283221

Prilutsky, B. I., Ashley, D., Vanhiel, L., Harley, L., Tidwell, J. S., & Backus, D. (2011). Motor Control and Motor Redundancy Implications for Neurorehabilitation, *17*(1), 7–15. https://doi.org/10.1310/sci1701-7

Ricci, L., Formica, D., Tamilia, E., Taffoni, F., Sparaci, L., Capirci, O., & Guglielmelli, E. (2013). An experimental protocol for the definition of upper limb anatomical frames on children using magneto-inertial sensors. In *2013 35th Annual International Conference of the IEEE Engineering in Medicine and Biology Society (EMBC)* (Vol. 2013, pp. 4903–4906). IEEE. https://doi.org/10.1109/EMBC.2013.6610647

Ricci, Luca, Formica, D., Sparaci, L., Lasorsa, F., Taffoni, F., Tamilia, E., & Guglielmelli, E. (2014). A New Calibration Methodology for Thorax and Upper Limbs Motion Capture in Children Using Magneto and Inertial Sensors. *Sensors, 14*(1), 1057–1072. https://doi.org/10.3390/s140101057

Roetenberg, D., Luinge, H. J., Baten, C. T. M., & Veltink, P. H. (2005). Compensation of magnetic disturbances improves inertial and magnetic sensing of human body segment orientation. *IEEE Transactions on Neural Systems and Rehabilitation Engineering*, *13*(3), 395–405. https://doi.org/10.1109/TNSRE.2005.847353

Roetenberg, D., Luinge, H., & Slycke, P. (2013). *Xsens MVN : Full 6DOF Human*

Motion Tracking Using Miniature Inertial Sensors. XSENS TECHNOLOGIES white paper, www.xsens.com/images/stories/PDF/ MVN_white_paper.pdf. Retrieved from http://en.souvr.com/product/pdf/MVN_white_paper.pdf

Rothwell, J. (1994). *Control of Human Voluntary Movement* (2nd Editio). Dordrecht: Springer Netherlands. https://doi.org/10.1007/978-94-011-6960-8

Rushton, D. N. (2003). Functional Electrical Stimulation and rehabilitation—an hypothesis. *Medical Engineering & Physics*, *25*(1), 75–78. https://doi.org/10.1016/S1350-4533(02)00040-1

Saladin, K. S. (2001). *Anatomy & Physiology: the Unity of Form and Function* (2nd Editio). New York, NY: McGraw-Hill.

Santisteban, L., Térémetz, M., Bleton, J. P., Baron, J. C., Maier, M. A., & Lindberg, P. G. (2016). Upper limb outcome measures used in stroke rehabilitation studies: A systematic literature review. *PLoS ONE*, *11*(5), 1–16. https://doi.org/10.1371/journal.pone.0154792

Schiefer, C., Ellegast, R. P., Hermanns, I., Kraus, T., Ochsmann, E., Larue, C., & Plamondon, A. (2014). Optimization of Inertial Sensor-Based Motion Capturing for Magnetically Distorted Field Applications. *Journal of Biomechanical Engineering*, *136*(12), 121008. https://doi.org/10.1115/1.4028822

Sharf, I., Wolf, A., & Rubin, M. B. (2010). Arithmetic and geometric solutions for average rigid-body rotation. *Mechanism and Machine Theory*, *45*(9), 1239–1251. https://doi.org/10.1016/j.mechmachtheory.2010.05.002

Sheffler, L. R., & Chae, J. (2007). Neuromuscular electrical stimulation in neurorehabilitation. *Muscle & Nerve*, *35*(5), 562–590. https://doi.org/10.1002/mus.20758

Sidenbladh, H., Black, M. J., & Fleet, D. J. (2000). Stochastic Tracking of 3D Human Figures Using 2D Image Motion. In D. Vernon (Ed.), *Computer Vision --- ECCV 2000: 6th European Conference on Computer Vision Dublin,*

Ireland, June 26--July 1, 2000 Proceedings, Part II (pp. 702–718). Berlin, Heidelberg: Springer Berlin Heidelberg. https://doi.org/10.1007/3-540-45053-X_45

Smith, C., Kenney, L., Howard, D., Sun, M., Luckie, H., Waring, K., … Health, F. (2017). The feasibility of using a novel functional electrical stimulation system (FES-UPP) in clinical environments , to support upper limb functional task practice following stroke. In *IFESS Conference.*

Smith, C., Sun, M., Kenney, L., Howard, D., Luckie, H., Waring, K., … Cotterill, S. (2019). A Three-Site Clinical Feasibility Study of a Flexible Functional Electrical Stimulation System to Support Functional Task Practice for Upper Limb Recovery in People With Stroke. *Frontiers in Neurology*, *10*(March), 1–14. https://doi.org/10.3389/fneur.2019.00227

Speich, J. E., & Rosen, J. (2004). Medical Robotics. *Encyclopedia of Biomaterials and Biomedical Engineering*, 983–993. Retrieved from http://www.ncbi.nlm.nih.gov/pubmed/7648297

Stockley, R., Peel, R., Jarvis, K., & Connell, L. (2019). Current therapy for the upper limb after stroke: a cross-sectional survey of UK therapists. *BMJ Open*, *9*(9), e030262. https://doi.org/10.1136/bmjopen-2019-030262

Sun, M. (2014). *A functional electrical stimulation (fes) control system for upper limb rehabilitation.* University of Salford. Retrieved from http://usir.salford.ac.uk/32854/1/Final_thesis_Mingxu_240914.pdf

Sun, M., Kenney, L., Smith, C., Waring, K., Luckie, H., Liu, A., & Howard, D. (2016). A novel method of using accelerometry for upper limb FES control. *Medical Engineering & Physics*, *38*(11), 1244–1250. https://doi.org/10.1016/j.medengphy.2016.06.005

Sun, M., Smith, C., Howard, D., Kenney, L., Luckie, H., Waring, K., … Finn, S. (2018). FES-UPP: A flexible functional electrical stimulation system to support upper limb functional activity practice. *Frontiers in Neuroscience*, *12*(JUL), 1–13. https://doi.org/10.3389/fnins.2018.00449

Sveistrup, H. (2004). Motor rehabilitation using virtual reality. *Journal of Neuroengineering and Rehabilitation*, *1*(1), 10. https://doi.org/10.1186/1743-0003-1-10

Tao, Y., Hu, H., Park, W., & Kingdom, U. (2003). Building A Visual Tracking System for Home-Based. *Proceedings of the 9th Chinese Automation & Computing Society Conference in the UK, Luton, England*, *9*(September), 443–448.

The MathWorks, I. U. S. (2019). MATLAB R2019a (9.6.0.1214997).

Timmermans, A. A. A., Seelen, H. A. M., Willmann, R. D., Bakx, W., de Ruyter, B., Lanfermann, G., & Kingma, H. (2009). Arm and hand skills: training preferences after stroke. *Disability and Rehabilitation*, *31*(16), 1344–1352. https://doi.org/10.1080/09638280902823664

Tresadern, P. A., Thies, S. B., Kenney, L. P. J., Howard, D., & Goulermas, J. Y. (2008). Rapid Prototyping for Functional Electrical Stimulation Control. *IEEE Pervasive Computing*, *7*(2), 62–69. https://doi.org/10.1109/MPRV.2008.35

Vignais, N., Miezal, M., Bleser, G., Mura, K., Gorecky, D., & Marin, F. (2013). Innovative system for real-time ergonomic feedback in industrial manufacturing. *Applied Ergonomics*, *44*(4), 566–574. https://doi.org/10.1016/j.apergo.2012.11.008

Walmsley, C. P., Williams, S. A., Grisbrook, T., Elliott, C., Imms, C., & Campbell, A. (2018). Measurement of Upper Limb Range of Motion Using Wearable Sensors: A Systematic Review. *Sports Medicine - Open*, *4*(1). https://doi.org/10.1186/s40798-018-0167-7

Ward, N. S., Brander, F., & Kelly, K. (2019). Intensive upper limb neurorehabilitation in chronic stroke: outcomes from the Queen Square programme. *Journal of Neurology, Neurosurgery & Psychiatry*, *90*(5), 498–506. https://doi.org/10.1136/jnnp-2018-319954

WHF. (2016). World Heart Federation. Retrieved from http://www.world-heart-federation.org/cardiovascular-health/stroke/

WHO. (2003). *World health report*. World Health Organization.

Wu, G., & Cavanagh, P. R. (1995). ISB recommendations in the reporting for standardization of kinematic data. *J Biomechanics*, *28*(10), 1257–1261. https://doi.org/10.1016/0021-9290(95)00017-C

Wu, G., Siegler, S., Allard, P., Kirtley, C., Leardini, A., Rosenbaum, D., … Stokes, I. (2002). ISB recommendation on definitions of joint coordinate system of various joints for the reporting of human joint motion—part I: ankle, hip, and spine. *Journal of Biomechanics*, *35*(4), 543–548. https://doi.org/10.1016/S0021-9290(01)00222-6

Wu, G., van der Helm, F. C. T., (DirkJan) Veeger, H. E. J., Makhsous, M., Van Roy, P., Anglin, C., … Buchholz, B. (2005). ISB recommendation on definitions of joint coordinate systems of various joints for the reporting of human joint motion—Part II: shoulder, elbow, wrist and hand. *Journal of Biomechanics*, *38*(5), 981–992. https://doi.org/10.1016/j.jbiomech.2004.05.042

Yang, H., & Ye, J. (2011). A calibration process for tracking upper limb motion with inertial sensors. In *2011 IEEE International Conference on Mechatronics and Automation* (Vol. 1, pp. 618–623). IEEE. https://doi.org/10.1109/ICMA.2011.5985732

Yi Zhang, Huosheng Hu, & Huiyu Zhou. (2005). Study on adaptive kalman filtering algorithms in human movement tracking. In *2005 IEEE International Conference on Information Acquisition* (pp. 11–15). IEEE. https://doi.org/10.1109/ICIA.2005.1635045

Zabat, M., Ababou, A., Ababou, N., & Dumas, R. (2019). IMU-based sensor-to-segment multiple calibration for upper limb joint angle measurement—a proof of concept. *Medical and Biological Engineering and Computing*, *57*(11), 2449–2460. https://doi.org/10.1007/s11517-019-02033-7

Zhang, J., Novak, A. C., Brouwer, B., & Li, Q. (2013). Concurrent validation of Xsens MVN measurement of lower limb joint angular kinematics.

Physiological Measurement, *34*(8), N63-9. https://doi.org/10.1088/0967-3334/34/8/N63

Zhou, H., & Hu, H. (2004). *A survey—human movement tracking and stroke rehabilitation.*

Zhou, H., & Hu, H. (2007a). Inertial sensors for motion detection of human upper limbs. *Sensor Review*, *27*(2), 151–158. https://doi.org/10.1108/02602280710731713

Zhou, H., & Hu, H. (2007b). Upper limb motion estimation from inertial measurements. *International Journal of Information Technology*, *13*(1), 1–14.

Zhou, H., & Hu, H. (2008). Human motion tracking for rehabilitation-A survey. *Biomedical Signal Processing and Control*, *3*(1), 1–18. https://doi.org/10.1016/j.bspc.2007.09.001

Zhou, H., Hu, H., & Tao, Y. (2006). Inertial measurements of upper limb motion. *Medical and Biological Engineering and Computing*, *44*(6), 479–487. https://doi.org/10.1007/s11517-006-0063-z

Zhou, H., Stone, T., Hu, H., & Harris, N. (2008). Use of multiple wearable inertial sensors in upper limb motion tracking. *Medical Engineering and Physics*, *30*(1), 123–133. https://doi.org/10.1016/j.medengphy.2006.11.010